

THE ATACAMA COSMOLOGY TELESCOPE: SUNYAEV-ZEL'DOVICH SELECTED GALAXY CLUSTERS AT 148 GHz FROM THREE SEASONS OF DATA

MATTHEW HASSELFIELD^{1,2}, MATT HILTON^{3,4}, TOBIAS A. MARRIAGE⁵, GRAEME E. ADDISON^{2,6}, L. FELIPE BARRIENTOS⁷,
 NICHOLAS BATTAGLIA^{8,9}, ELIA S. BATTISTELLI^{10,2}, J. RICHARD BOND⁹, DEVIN CRICHTON⁵, SUDEEP DAS^{11,12},
 MARK J. DEVLIN¹³, SIMON R. DICKER¹³, JOANNA DUNKLEY⁶, ROLANDO DÜNNER⁷, JOSEPH W. FOWLER^{14,15},
 MEGAN B. GRALLA⁵, AMIR HAJIAN⁹, MARK HALPERN², ADAM D. HINCKS⁹, RENÉE HLOZEK¹, JOHN P. HUGHES¹⁶,
 LEOPOLDO INFANTE⁷, KENT D. IRWIN¹⁴, ARTHUR KOSOWSKY¹⁷, DANICA MARSDEN^{18,13}, FELIPE MENANTEAU¹⁶,
 KAVILAN MOODLEY³, MICHAEL D. NIEMACK^{14,15,19}, MICHAEL R. NOLTA⁹, LYMAN A. PAGE¹⁵, BRUCE PARTRIDGE²⁰,
 ERIK D. REESE¹³, BENJAMIN L. SCHMITT¹³, NEELIMA SEHGAL²¹, BLAKE D. SHERWIN¹⁵, JON SIEVERS^{1,9},
 CRISTÓBAL SIFÓN²², DAVID N. SPERGER¹, SUZANNE T. STAGGS¹⁵, DANIEL S. SWETZ^{14,13}, ERIC R. SWITZER⁹,
 ROBERT THORNTON^{13,23}, HY TRAC⁸, EDWARD J. WOLLACK²⁴

Draft version December 12, 2013

ABSTRACT

We present a catalog of 68 galaxy clusters, of which 19 are new discoveries, detected via the Sunyaev-Zel'dovich effect (SZ) at 148 GHz in the Atacama Cosmology Telescope (ACT) survey on the celestial equator. With this addition, the ACT collaboration has reported a total of 91 optically confirmed, SZ detected clusters. The 504 square degree survey region includes 270 square degrees of overlap with SDSS Stripe 82, permitting the confirmation of SZ cluster candidates in deep archival optical data. The subsample of 48 clusters within Stripe 82 is estimated to be 90% complete for $M_{500c} > 4.5 \times 10^{14} M_{\odot}$ and redshifts $0.15 < z < 0.8$. While a full suite of matched filters is used to detect the clusters, the sample is studied further through a “Profile Based Amplitude Analysis” using a statistic derived from a single filter at a fixed $\theta_{500} = 5'.9$ angular scale. This new approach incorporates the cluster redshift along with prior information on the cluster pressure profile to fix the relationship between the cluster characteristic size (R_{500}) and the integrated Compton parameter (Y_{500}). We adopt a one-parameter family of “Universal Pressure Profiles” (UPP) with associated scaling laws, derived from X-ray measurements of nearby clusters, as a baseline model. Three additional models of cluster physics are used to investigate a range of scaling relations beyond the UPP prescription. Assuming a concordance cosmology, the UPP scalings are found to be nearly identical to an adiabatic model, while a model incorporating non-thermal pressure better matches dynamical mass measurements and masses from the South Pole Telescope. A high signal to noise ratio subsample of 15 ACT clusters with complete optical follow-up is used to obtain cosmological constraints. We demonstrate, using fixed scaling relations, how the constraints depend on the assumed gas model if only SZ measurements are used, and show that constraints from SZ data are limited by uncertainty in the scaling relation parameters rather than sample size or measurement uncertainty. We next add in seven clusters from the ACT Southern survey, including their dynamical mass measurements, which are based on galaxy velocity dispersions and thus are independent of the gas physics. In combination with WMAP7 these data simultaneously constrain the scaling relation and cosmological parameters, yielding 68% confidence ranges described by $\sigma_8 = 0.829 \pm 0.024$ and $\Omega_m = 0.292 \pm 0.025$. We consider these results in the context of constraints from CMB and other cluster studies. The constraints arise mainly due to the inclusion of the dynamical mass information and do not require strong priors on the SZ scaling relation parameters. The results include marginalization over a 15% bias in dynamical masses relative to the true halo mass. In an extension to Λ CDM that incorporates non-zero neutrino mass density, we combine our data with WMAP7, Baryon Acoustic Oscillation data, and Hubble constant measurements to constrain the sum of the neutrino mass species to be $\sum_{\nu} m_{\nu} < 0.29$ eV (95% confidence limit).

Subject headings: cosmology:cosmic microwave background – cosmology:observations – galaxies:clusters – Sunyaev-Zel'dovich Effect

¹ Department of Astrophysical Sciences, Peyton Hall, Princeton University, Princeton, NJ 08544, USA

² Department of Physics and Astronomy, University of British Columbia, Vancouver, BC, V6T 1Z4, Canada

³ Astrophysics and Cosmology Research Unit, School of Mathematics, Statistics & Computer Science, University of KwaZulu-Natal, Durban, 4041, South Africa

⁴ Centre for Astronomy & Particle Theory, School of Physics & Astronomy, University of Nottingham, Nottingham, NG7 2RD, UK

⁵ Dept. of Physics and Astronomy, The Johns Hopkins Uni-

versity, 3400 N. Charles St., Baltimore, MD 21218-2686, USA

⁶ Department of Astrophysics, Oxford University, Oxford, OX1 3RH, UK

⁷ Departamento de Astronomía y Astrofísica, Facultad de Física, Pontificia Universidad Católica, Casilla 306, Santiago 22, Chile

⁸ Department of Physics, Carnegie Mellon University, Pittsburgh, PA 15213, USA

⁹ Canadian Institute for Theoretical Astrophysics, University of Toronto, Toronto, ON, M5S 3H8, Canada

¹⁰ Department of Physics, University of Rome “La Sapienza”,

1. INTRODUCTION

Galaxy clusters are sensitive tracers of the growth of structure in the Universe. The measurement of their evolving abundance with redshift has the potential to provide constraints on cosmological parameters that are complementary to other measurements, such as the angular power spectrum of the cosmic microwave background (CMB; e.g., [Hinshaw et al. 2012](#); [Dunkley et al. 2011](#); [Keisler et al. 2011](#); [Story et al. 2012](#)), Type Ia supernovae (e.g., [Hicken et al. 2009](#); [Lampeitl et al. 2010](#); [Suzuki et al. 2012](#)), or baryon acoustic oscillations measured in galaxy correlation functions (e.g., [Percival et al. 2010](#)).

There is a long history of using optical (e.g., [Abell 1958](#); [Lumsden et al. 1992](#); [Goto et al. 2002](#); [Lopes et al. 2004](#); [Miller et al. 2005](#); [Koester et al. 2007](#); [Hao et al. 2010](#); [Szabo et al. 2011](#); [Wen et al. 2009, 2012](#)) and X-ray (e.g., [Henry et al. 1992](#); [Böhringer et al. 2004](#); [Burenin et al. 2007](#); [Mehrtens et al. 2012](#)) surveys to search for galaxy clusters. Data from such surveys offered an early indication of an $\Omega_m < 1$ universe (e.g., [Bahcall & Cen 1992](#)). Recent results have demonstrated the power of modern optical and X-ray surveys for constraining cosmology (e.g., [Vikhlinin et al. 2009b](#); [Mantz et al. 2010b](#); [Rozo et al. 2010](#)). A promising method for both detecting clusters in optical surveys and simultaneously providing mass estimates is to use weak gravitational lensing shear selection, and the first such samples using this technique have recently appeared (e.g., [Wittman et al. 2006](#); [Miyazaki et al. 2007](#)). Within the last few years, cluster surveys exploiting the Sunyaev-Zel'dovich effect (SZ; [Sunyaev & Zel'dovich 1970](#)) have also begun to deliver cluster samples (e.g., [Staniszewski et al. 2009](#); [Marriage et al. 2011](#); [Williamson et al. 2011](#); [Planck Collaboration 2011a](#); [Reichardt et al. 2013](#)) and constraints on cosmological parameters ([Vanderlinde et al. 2010](#); [Sehgal et al. 2011](#); [Benson et al. 2013](#); [Reichardt et al. 2013](#)).

The thermal SZ effect is the inverse Compton scattering of CMB photons by electrons within the hot ($\sim 10^7\text{--}8\text{ K}$) intracluster medium of galaxy clusters. This leads to a spectral distortion in the direction of clusters, with the size of the effect being proportional to the volume-integrated thermal pressure and thus, in the adiabatic scenario, the total thermal energy of the cluster gas. Accordingly, this is correlated with cluster mass (e.g., [Bonamente et al. 2008](#); [Marrone et al. 2012](#); [Sifón et al. 2012](#); [Planck Collaboration et al. 2013](#)). Since the SZ signal is not diminished due to luminosity distance, it is nearly redshift independent; in principle SZ surveys can detect all clusters in the Universe above a mass limit set by the survey noise level (e.g., [Birkinshaw 1999](#); [Carlstrom et al. 2002](#)).

Although current SZ cluster samples are small in comparison to existing X-ray and optical cluster catalogs, they provide very powerful complementary probes because they are sensitive to the high mass, high redshift cluster population (e.g., [Brodwin et al. 2010](#); [Foley et al. 2011](#); [Planck Collaboration 2011b](#); [Menanteau et al. 2012](#); [Stalder et al. 2012](#)). Many studies (e.g., [Hoyle et al. 2011](#); [Mortonson et al. 2011](#); [Hotchkiss 2011](#); [Harrison & Coles 2012](#)) have noted that the discovery of a sufficiently massive cluster at high redshift would be a challenge to Λ CDM cosmology, and the approximately redshift independent, mass-limited nature of SZ surveys means that they are well suited to reveal such objects if they exist.

In this paper we describe the results of a search for galaxy clusters using the SZ effect in maps of the celestial equator obtained by the Atacama Cosmology Telescope (ACT; [Swetz et al. 2011](#)). ACT is a 6 m telescope located in northern Chile that observes the sky in three frequency bands (centered at 148, 218, and 277 GHz) simultaneously with arcminute resolution. During 2008, ACT surveyed a 455 deg^2 patch of the Southern sky, centered on $\delta = -55\text{ deg}$, detecting a number of SZ cluster candidates of which 23 were optically confirmed as massive clusters ([Menanteau et al. 2010](#); [Marriage et al. 2011](#)). The Equatorial survey area, on which we report in this work, was chosen to overlap the deep ($r \approx 23.5\text{ mag}$) optical data from the Sloan Digital Sky Survey (SDSS; [Abazajian et al. 2009](#)) Stripe 82 region (S82 hereafter; [Annis et al. 2011](#)). Optical confirmation of our SZ cluster candidates is reported in [Menanteau et al. \(2013\)](#), using data from SDSS and additional targeted optical and IR observations obtained at Apache Point Observatory. All clusters have photometric redshifts, and most have spectroscopic redshifts from a combination of SDSS and new observations at Gemini South. X-ray fluxes from the ROSAT All Sky Survey confirm that this is a massive cluster sample. The overlap of the ACT survey with SDSS has also enabled stacking analyses which characterize the SZ-signal as a function of halo mass from optically selected samples ([Hand et al. 2011](#); [Sehgal et al. 2013](#)), as well as a first detection of the kinetic SZ effect from the correlation of positions and redshifts of luminous red galaxies with temperature in the ACT maps ([Hand et al. 2012](#)).

The structure of this paper is as follows. In Section 2 we describe the processing of the ACT data used in this work and the cluster detection algorithm. In Section 3

Piazzale Aldo Moro 5, I-00185 Rome, Italy

¹¹ High Energy Physics Division, Argonne National Laboratory, 9700 S Cass Avenue, Lemont, IL 60439, USA

¹² Berkeley Center for Cosmological Physics, LBL and Department of Physics, University of California, Berkeley, CA 94720, USA

¹³ Department of Physics and Astronomy, University of Pennsylvania, 209 South 33rd Street, Philadelphia, PA 19104, USA

¹⁴ NIST Quantum Devices Group, 325 Broadway Mailcode 817.03, Boulder, CO 80305, USA

¹⁵ Joseph Henry Laboratories of Physics, Jadwin Hall, Princeton University, Princeton, NJ 08544, USA

¹⁶ Department of Physics and Astronomy, Rutgers, The State University of New Jersey, Piscataway, NJ 08854-8019, USA

¹⁷ Department of Physics and Astronomy, University of Pittsburgh, Pittsburgh, PA 15260, USA

¹⁸ Department of Physics, University of California Santa Barbara, CA 93106, USA

¹⁹ Department of Physics, Cornell University, Ithaca, NY 14853, USA

²⁰ Department of Physics and Astronomy, Haverford College, Haverford, PA 19041, USA

²¹ Department of Physics and Astronomy, Stony Brook, NY 11794-3800, USA

²² Leiden Observatory, Leiden University, PO Box 9513, NL-2300 RA Leiden, Netherlands

²³ Department of Physics, West Chester University of Pennsylvania, West Chester, PA 19383, USA

²⁴ NASA/Goddard Space Flight Center, Greenbelt, MD 20771, USA

we describe our approach to relating the cluster signal in filtered SZ maps to cluster mass, and obtain mass estimates for our cluster sample. In Section 4 we compare our catalog to other SZ, optical, and X-ray selected cluster catalogs. In Section 5 we obtain constraints on cosmological parameters using the ACT cluster sample. In an Appendix, we present analogous SZ signal measurements and mass estimates for ACT’s Southern field clusters, using deeper data obtained over the course of the 2009–2010 observing seasons.

Where it is necessary to adopt a fiducial cosmology, we assume $\Omega_m = 0.3$, $\Omega_\Lambda = 0.7$, and $H_0 = 70 h_{70} \text{ km s}^{-1} \text{ Mpc}^{-1}$ ($h_{70} = 1$), unless stated otherwise. Throughout this paper, cluster mass is measured within a characteristic radius with respect to the critical density such that, e.g., M_{500c} is defined as the mass measured within the radius (R_{500}) at which the enclosed mean density is 500 times the critical density at the cluster redshift. The function $E(z)$ denotes the evolution of the Hubble parameter with redshift (i.e., $E(z) = [\Omega_m(1+z)^3 + \Omega_\Lambda]^{1/2}$ for a universe with $\Omega_k = 0$ and negligible radiation density). Uncertainties and error bars are specified at the $1\text{-}\sigma$ level, and posterior distributions are summarized in terms of their mean and standard deviation unless otherwise indicated.

2. MAPS AND CLUSTER DETECTION

In this section we discuss the detection of galaxy clusters in the ACT Equatorial maps at 148 GHz. The maps are filtered to enhance structures whose shape matches the Universal Pressure Profile of Arnaud et al. (2010). The final cluster catalog consists of SZ candidates that have been confirmed in optical or IR imaging.

2.1. Equatorial Maps

ACT’s observations during the 2009 and 2010 seasons were concentrated on the celestial equator. For this study we make use of the 504 square degree deep, contiguous region spanning from $20^{\text{h}}16^{\text{m}}00^{\text{s}}$ to $3^{\text{h}}52^{\text{m}}24^{\text{s}}$ in right ascension and from $-2^{\circ}07'$ to $2^{\circ}18'$ in declination. This region includes 270 square degrees of overlap with S82, which extends to $20^{\text{h}}39^{\text{m}}$ in R.A. and $\pm 1^{\circ}15'$ in declination. As shown in Figure 1, the S82 region corresponds to the lowest-noise region of the ACT Equatorial maps.

The bolometer time-stream data are acquired while scanning the telescope in azimuth at fixed elevation. Cross-linked data are obtained by observing the same celestial region at two telescope pointings that produce approximately orthogonal scan directions. Because the scan strategy was optimized for simultaneous observation with the 148 GHz and 218 GHz arrays (the centers of which are separated by approximately $33'$ when projected onto the sky), the regions beyond declinations of $\pm 1^{\circ}40'$ are not well cross-linked.

The ACT data reduction pipeline and map-making procedure are described in Dünner et al. (2013), in the context of ACT’s 2008 data. The time-stream bolometer data are screened for pathologies and then combined to obtain a maximum likelihood estimate of the microwave sky map (with $0.5'$ pixels) for each observing season. As a result of the cross-linked scan strategy, and the careful treatment of noise during map making, the ACT maps are unbiased at angular scales $\ell > 300$.

Due to realignments of the primary and secondary mirrors, the telescope beams vary slightly between seasons but are stable over the course of each season. The telescope beams are determined from observations of Saturn, using the method described in Hincks et al. (2010), but with additional corrections to account for $\approx 6''$ RMS pointing variation between observations made on different nights (Hasselfield et al., in prep.). The effective beam for the 148 GHz array differs negligibly between the 2009 and 2010 seasons, with a FWHM of $1.4'$ and solid angle (including the effects of pointing variation) of $224 \pm 2 \text{ nsr}$.

Calibrations of ACT observations are based on frequent detector load curves, and atmospheric opacity water vapor measurements (Dünner et al. 2013). Absolute calibration of the ACT maps is achieved by comparing the large angular scale ($300 < \ell < 1100$) signal from the 2010 season maps to the WMAP 95 GHz 7-year maps (Jarosik et al. 2011). Using a cross-correlation technique as described in Hajian et al. (2011), an absolute calibration uncertainty of $\approx 2\%$ in temperature is achieved (Das et al. 2013). The inter-calibration of 2009 and 2010 is measured through a similar cross-correlation technique, with less than 2% error.

2.2. Gas Pressure Model

At several stages in the detection and analysis we will require a template for the intracluster gas pressure profile. To this end we adopt the “Universal Pressure Profile” (UPP) of Arnaud et al. (2010, hereafter A10), which includes mass dependence in the profile shape and has been calibrated to X-ray observations of nearby clusters. In this section we review the form of the UPP, and obtain several approximations that will be used in cluster detection (Section 2.3) and cluster property recovery (Section 3).

In A10, the cluster electron pressure as a function of physical radius r is modeled with a generalized Navarro-Frenk-White (GNFW) profile (Nagai, Kravtsov, & Vikhlinin 2007),

$$p(x) = P_0 (c_{500}x)^{-\gamma} (1 + (c_{500}x)^\alpha)^{(\gamma-\beta)/\alpha}, \quad (1)$$

where $x = r/R_{500}$ and $P_0, c_{500}, \gamma, \alpha, \beta$ are fit parameters. The overall pressure normalization, under assumptions of self-similarity (i.e., the case when gravity is the sole process responsible for setting cluster properties), varies with mass and redshift according to

$$P_{500} = [1.65 \times 10^{-3} h_{70}^2 \text{ keV cm}^{-3}] m^{2/3} E^{8/3}(z), \quad (2)$$

where $E(z)$ is the ratio of the Hubble constant at redshift z to its present value, and

$$m \equiv M_{500c} / (3 \times 10^{14} h_{70}^{-1} \text{ M}_\odot) \quad (3)$$

is a convenient mass parameter. Some deviation from strict self-similarity may be encoded via an additional mass dependence in the shape of the profile, yielding a form

$$P(r) = P_{500} m^{\alpha_p(x)} p(x). \quad (4)$$

In this framework, A10 use X-ray observations of local ($z < 0.2$) clusters to obtain best-fit GNFW parameters $[P_0, c_{500}, \gamma, \alpha, \beta] = [8.403 h_{70}^{3/2}, 1.177, 0.3081, 1.0510,$

5.4905], and an additional radial dependence described reasonably well by $\alpha_p(x) = 0.22/(1 + 8x^3)$.

Because hydrostatic mass estimates are used by A10 to assess the relationship between cluster mass and the pressure profile, there may be systematic differences when one makes use of an alternative mass proxy, such as weak lensing or galaxy velocity dispersion. Simulations suggest that hydrostatic masses are underestimates of the true cluster mass (e.g., Nagai et al. 2007). However, there is little consensus among recent studies which compare X-ray hydrostatic and weak lensing mass measurements. For example, Mahdavi et al. (2013) find that hydrostatic masses are lower than weak lensing masses by about 10% at R_{500} ; Zhang et al. (2010) and Vikhlinin et al. (2009a) find reasonable agreement; while Planck Collaboration et al. (2013) find hydrostatic masses to be about 20% larger than weak lensing masses. Therefore in our initial treatment of the UPP we neglect this bias; later we will address this issue by adding degrees of freedom to allow for changes in the normalization of the pressure profile.

The thermal SZ signal is related to the optical depth for Compton scattering along a given line of sight. For our pressure profile, and in the absence of relativistic effects, this Compton parameter at projected angle θ from the cluster center is

$$y(\theta) = \frac{\sigma_T}{m_e c^2} \int ds P \left(\sqrt{s^2 + (R_{500}\theta/\theta_{500})^2} \right), \quad (5)$$

where $\theta_{500} = R_{500}/D_A(z)$ with $D_A(z)$ the angular diameter distance to redshift z , σ_T is the Thomson cross section, m_e is the electron mass, and the integral in s is along the line of sight. Relativistic effects change this picture somewhat, but for convenience we will use the above definition of $y(\theta)$ and apply the relativistic correction only when calculating the SZ signal associated with a particular y .

To simplify the expression for the cluster pressure profile, we first consider the mass parameter $m = 1$ and factor the expression in equation (5) to get

$$y(\theta, m = 1) = 10^{A_0} E(z)^2 \tau(\theta/\theta_{500}) \quad (6)$$

where $\tau(x)$ is a dimensionless profile normalized to $\tau(0) = 1$, and $10^{A_0} = 4.950 \times 10^{-5} h_{70}^{1/2}$ gives the normalization. The deviations from self-similarity are weak enough that we may model the changes in the profile shape with mass as simple adjustments to the normalization and angular scale of the profile. For the masses of interest here ($1 < m < 10$) we obtain

$$y(\theta, m) \approx 10^{A_0} E(z)^2 m^{1+B_0} \tau(m^{C_0} \theta/\theta_{500}) \quad (7)$$

with $B_0 = 0.08$ and $C_0 = -0.025$. This approximation reproduces the inner signal shape extremely well, with deviations increasing to the 0.5% level by θ_{500} . For $0.1\theta_{500} < \theta < 3\theta_{500}$, the enclosed signal ($\int_0^\theta d\theta' 2\pi\theta' y(\theta', m)$) differs by less than 1% from the results of the full computation. This parametrization of the cluster signal in terms of a normalization and dimensionless profile is not used for cluster detection (Section 2.3), but will motivate the formulation of scaling relations and permit the estimation of cluster masses (Section 3.1).

The observed signal due to the SZ effect is a change in radiation intensity, expressed in units of CMB temperature:

$$\frac{\Delta T(\theta)}{T_{\text{CMB}}} = f_{\text{SZ}} y(\theta). \quad (8)$$

In the non-relativistic limit, the factor f_{SZ} depends only on the observed radiation frequency. Integrating this non-relativistic SZ spectral response over the nominal 148 GHz array band-pass, we obtain an effective frequency of 146.9 GHz (Swetz et al. 2011). At this frequency, the formulae of Itoh et al. (1998) provide a spectral factor, including relativistic effects for gas temperature T_e , of $f_{\text{SZ}}(t) = -0.992 f_{\text{rel}}(t)$ where $t = k_B T_e / m_e c^2$ and $f_{\text{rel}}(t) = 1 + 3.79t - 28.2t^2$. This results in a 6% correction for a cluster with $T = 10$ keV. We use the scaling relation of Arnaud et al. (2005), $t = -0.00848 \times (mE(z))^{-0.585}$, to express the mean temperature dependence in terms of the cluster mass and redshift. This yields a final form, $f_{\text{SZ}}(m, z) = -0.992 f_{\text{rel}}(m, z)$, which we use in all subsequent modeling of the SZ signal. The corrections for the ACT cluster sample range from roughly 3% to 10%.

2.3. Galaxy Cluster Detection

In addition to the temperature decrements due to galaxy clusters, the ACT maps at 148 GHz contain contributions from the CMB, radio point sources, dusty galaxies, and noise from atmospheric fluctuations and the detectors. To detect galaxy clusters in the ACT maps we make use of a set of matched filters, with signal templates based on the UPP through the integrated profile template $\tau(\theta/\theta_{500})$.

We consider signal templates $S_{\theta_{500}}(\theta) \equiv \tau(\theta/\theta_{500})$ for $\theta_{500} = 1.18$ to $27'$ in increments of $1.18'$. Each fixed angular scale corresponds to a physical scale that varies with redshift, but can be computed for a given cosmology. For each signal template we form an associated matched filter in Fourier space

$$\Psi_{\theta_{500}}(\mathbf{k}) = \frac{1}{\Sigma_{\theta_{500}}} \frac{B(\mathbf{k}) S_{\theta_{500}}(k)}{N(\mathbf{k})} \quad (9)$$

where $B(\mathbf{k})$ is the product of the telescope beam response with the map pixel window function, $N(\mathbf{k})$ is the (anisotropic) noise power spectrum of the map, and $\Sigma_{\theta_{500}}$ is a normalization factor chosen so that, when applied to a map containing a beam-convolved cluster signal $-\Delta T[S_{\theta_{500}} * B](\theta)$ (in temperature units), the matched filter returns the central decrement $-\Delta T$.

Since the total power from the galaxy cluster SZ signal is low compared to the CMB, atmospheric noise, and white noise that contaminate the cluster signal, we estimate the noise spectrum $N(\mathbf{k})$ from the map directly. Bright (signal to noise ratio greater than five) point sources are masked from the map, with the masking radius ranging from $2'$ for the dimmest sources to 1° for the brightest source. A plane is fit to the map signal (weighting by the inverse number of samples in each pixel) and removed, and the map is apodized within 0.2° of the map edges.

For ACT, the effect of the noise term in the matched filter is to strongly suppress signal below $\ell \approx 3000$ (corresponding to scales larger than $7'$). When combined with

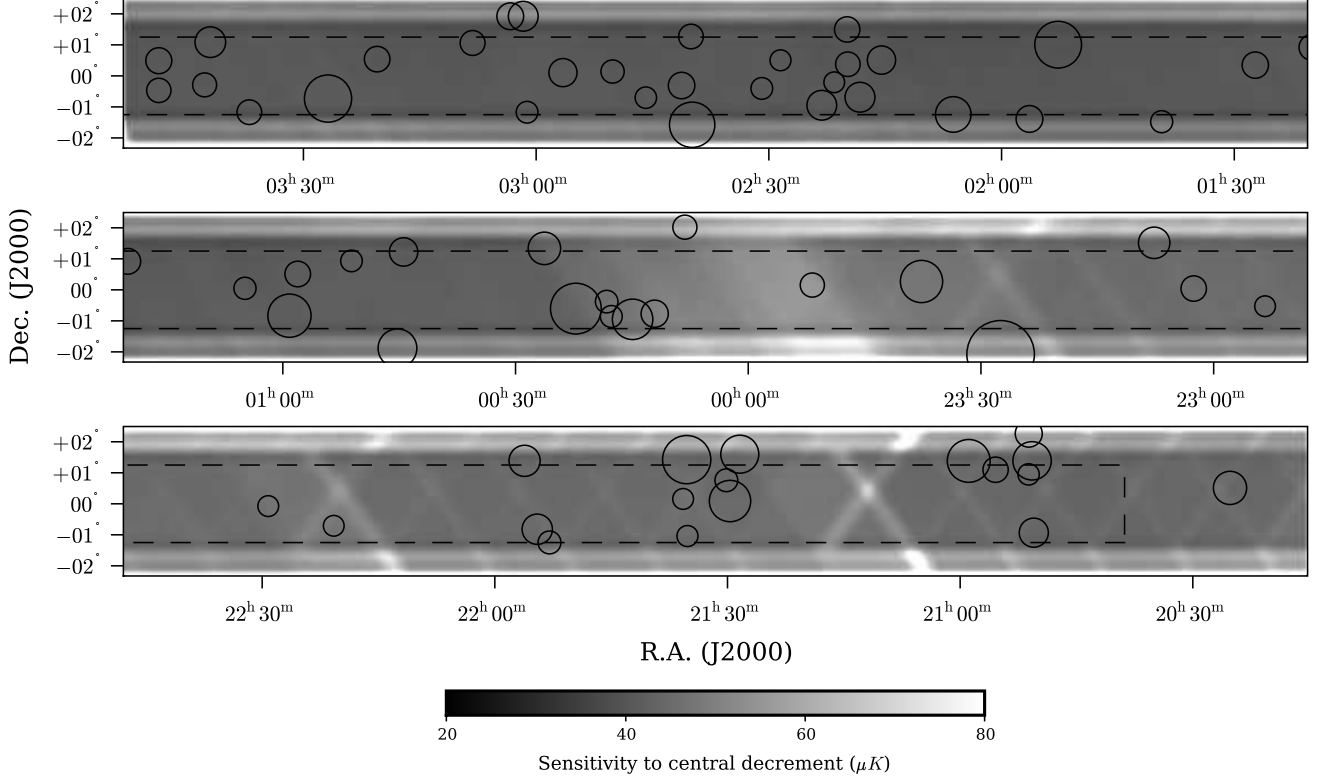


Figure 1. The portion of the ACT Equatorial survey region considered in this work. It spans from $20^{\text{h}}16^{\text{m}}00^{\text{s}}$ to $3^{\text{h}}52^{\text{m}}24^{\text{s}}$ in R.A. and from $-2^{\circ}07'$ to $2^{\circ}18'$ in declination for a total of 504 square degrees. The overlap with Stripe 82 (dashed line) extends only to $20^{\text{h}}39^{\text{m}}$ in R.A. and covers $\pm 1^{\circ}15'$ in declination, for a total of 270 square degrees. Circles identify the optically confirmed SZ-selected galaxy clusters, with radius proportional to the signal to noise ratio of the detection (which ranges from 4 to 13). The gray-scale gives the sensitivity (in CMB μK) to detection of galaxy clusters, *after filtering*, for the matched filter with $\theta_{500} = 5'.9$ (see Section 2.3). Inside the Stripe 82 region the median noise level is 44 μK , with one quarter of pixels having noise less (respectively, more) than 41 μK (46 μK). Outside Stripe 82, the median level is 54 μK , with one quarter of pixels having less (more) than 47 (64) μK noise. The higher noise, X-shaped regions are due to breaks in the scan for calibration operations.

the signal template (and beam), the filters form band-passes centered at ℓ ranging from roughly 2500 to 5000. The angular scales probed by the filters are thus sufficiently small that filtering artifacts near the map boundaries are mitigated by the map apodization. While the suppression of large angular scales disfavors the detection of clusters with large angular sizes, we apply the full suite of filters in order to maximize detection probability and to study the features of inferred cluster properties as the assumed cluster scale is varied.

The azimuthally averaged real space filter kernel corresponding to $\theta_{500} = 5'.9$ is shown in Figure 2, and compared to both the ACT 148 GHz beam and the signal template $S_{\theta_{500}}$.

The true noise spectrum may vary somewhat over the map due to variations in atmospheric and detector noise levels, and thus the matched filter $\Psi_{\theta_{500}}(\mathbf{k})$ might be said to be sub-optimal at any point. The filter remains *unbiased*, however, and a reasonable estimate of the signal to noise ratio (S/N) may still be obtained by recognizing that the local noise level will be highly correlated with the number of observations contributing to a given map pixel.

Prior to matched filtering, the ACT maps are conditioned in the same way as for noise estimation, except that the point sources are subtracted from the maps in-

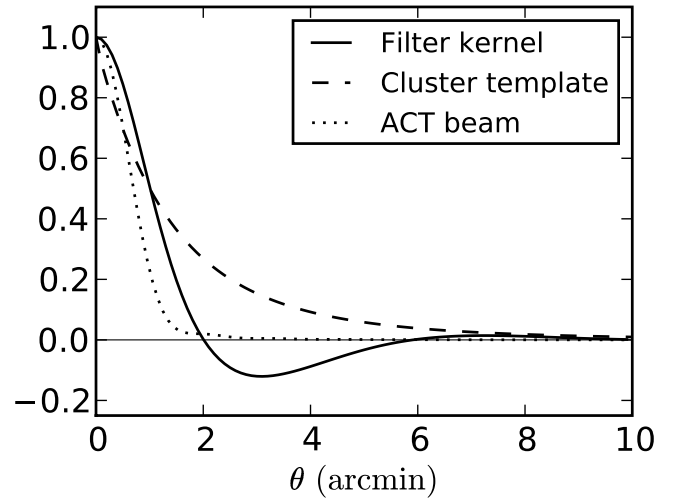


Figure 2. The azimuthally averaged real space matched filter kernel, proportional to $\Psi_{5'.9}(\theta)$, for signal template with $\theta_{500} = 5'.9$. Shown for reference are the ACT 148 GHz beam, and the cluster signal template $S_{5'.9}(\theta)$. While filters tuned to many different angular scales are used for cluster detection (Section 2.3), the 5/9 filter is used for cluster characterization and cosmology (Section 3.1).

stead of being masked. (Subsequent analysis disregards regions near those point sources, amounting to 1% of the map area.) With the application of each filter we obtain a map of ΔT values. A section of a filtered map (for $\theta_{500} = 5.9$) is shown in Figure 3.

We characterize the noise in each filtered map by modeling the variance at position \mathbf{x} as $\sigma^2(\mathbf{x}) = \sigma_0^2 + \sigma_{\text{hits}}^2/n_{\text{hits}}(\mathbf{x})$, where $n_{\text{hits}}(\mathbf{x})$ is the number of detector samples falling in the pixel at \mathbf{x} . We fit constants σ_0 and σ_{hits} by binning in small ranges of $1/n_{\text{hits}}$. The fit is iterated after excluding regions near pixels that are strong outliers to the noise model. Typically such pixels are near eventual galaxy cluster candidates. Figure 1 shows the noise map for the $\theta_{500} = 5.9$ filter.

After forming the signal to noise ratio map $-\Delta T(\mathbf{x})/\sigma(\mathbf{x})$, cluster candidates are identified as all pixels with values exceeding four. The catalog of cluster candidates contains positions, central decrements (ΔT), and the local map noise level. Candidates seen at multiple filter scales are cross-identified if the detection positions are within $1'$; the cluster candidate positions that we list come from the map where the cluster was most significantly detected. We adopt the largest S/N value obtained over the range of filter scales as the detection significance for each candidate.

For a given candidate, the S/N tends to vary only weakly with the filter scale. The reconstructed central decrement ΔT varies weakly above filter scales of $\theta_{500} \approx 3'$, as may be seen for the most significantly detected clusters in Figure 4. This stabilization occurs when the assumed cluster size is larger than the true cluster size, because the filter is optimized to return the difference in the level of the signal at the cluster position and the level of the signal away from the cluster center. The filter interprets the signal at the cluster position as being due to the convolution of the telescope beam with the cluster signal. The inferred central decrement thus rises rapidly as the assumed θ_{500} decreases, since total SZ flux scales as $\Delta T \theta_{500}^2$. As is discussed in Section 3.1, only the results from the $\theta_{500} = 5.9$ matched filter are used for inferring masses, scaling relations, and cosmological results. The corresponding physical scale may be determined, as a function of redshift, based on cluster distance.

2.4. Galaxy Cluster Confirmation

The cluster candidates obtained from the 148 GHz map analysis are confirmed using optical and infrared imaging. A complete discussion of this process may be found in Menanteau et al. (2013). For the purposes of this work, we briefly summarize the confirmation process and the redshift limits of the sample (which must be understood in order to derive cosmological constraints). These limits differ according to the depth of the optical imaging available over a given part of the map.

Most cluster candidates are confirmed through the analysis of SDSS imaging. The ACT Equatorial survey is almost entirely covered by SDSS archival data (Abazajian et al. 2009), with a central strip designed to overlap with the deep optical data ($r \approx 23.5$) in the S82 region (Annis et al. 2011), as shown in Figure 1. For each ACT cluster candidate with peak S/N > 4 , SDSS images are studied using an iterative photometric anal-

ysis to identify a brightest cluster galaxy (BCG) and an associated red sequence of member galaxies. A minimum richness of $N_{\text{gal}} = 15$, evaluated within a projected $1 h^{-1}$ Mpc of the nominal cluster center and within $0.045(1+z_c)$ of the nominal cluster redshift z_c , is required for the candidate to be confirmed as a cluster. The redshifts of confirmed clusters are obtained from either a photometric analysis of the images, from SDSS spectroscopy of bright cluster members, or from targeted multi-object spectroscopic follow-up. The redshift limit of cluster confirmation using SDSS data alone is estimated to be $z \approx 0.8$ within S82 and $z \approx 0.5$ outside of S82. Cluster candidates that are not confirmed in SDSS imaging are targeted, in an on-going follow-up campaign, under the assumption that they may be high redshift clusters.

Within the S82 region, 49 of 155 candidates are confirmed, with 44 of these confirmations resulting from analysis of SDSS data only. Targeted follow-up of the high S/N candidates was pursued at the Apache Point Observatory, yielding five more confirmations, all at $z > 0.9$. All cluster candidates with S/N > 5.1 were confirmed as clusters. This is consistent with our estimate of 1.8 false detections in this region, based on filtering of simulated noise. The follow-up in the S82 region is deemed complete to a S/N of 5.1, in the sense that all SZ candidates with ACT S/N > 5.1 have been targeted. It is thus this sample, and this region, that are considered for the cosmological analysis (in addition to a subset of the Marriage et al. (2011) sample; see Section 5). The completeness within S82, as a function of mass and redshift, is estimated in Section 3.6.

Outside of S82, 19 clusters are confirmed using SDSS DR8 data. High significance SZ detections in this region that are not confirmed in the DR8 data constitute good candidates for high redshift galaxy clusters and are being investigated in a targeted follow-up campaign.

The confirmed cluster sample may contain a small number of false positives, due to chance superposition of a low mass cluster at the location of an otherwise spurious SZ candidate. Most of our confirmed clusters are associated with rich optical counterparts, and thus are truly massive clusters. However, our search was carried out over considerable sky area in the ≈ 150 regions around SZ candidates. Assigning an effective area of 13 square arcminutes to each of these fields yields a total area of approximately 0.5 square degrees. From the maxBCG catalog (Koester et al. 2007), which includes optical richness measurements for clusters with $0.1 < z < 0.3$, we expect that the density of clusters satisfying our richness criteria in the range $0.1 < z < 0.8$ is approximately 6 per square degree. We conclude that roughly three of our low richness confirmed clusters could potentially be spurious associations. Such contamination is not likely to affect the high significance (S/N > 5.1) sample, where the lowest richness is ≈ 30 .

In Table 7 we present the catalog of 68 confirmed clusters. For each object we list its coordinates, redshift (see Menanteau et al. 2013, for details), S/N of the detection (we adopt the maximum S/N across the range of filters used), and SZ properties. Figure 5 shows postage stamp images of some high-significance clusters, taken from the filtered ACT 148 GHz maps.

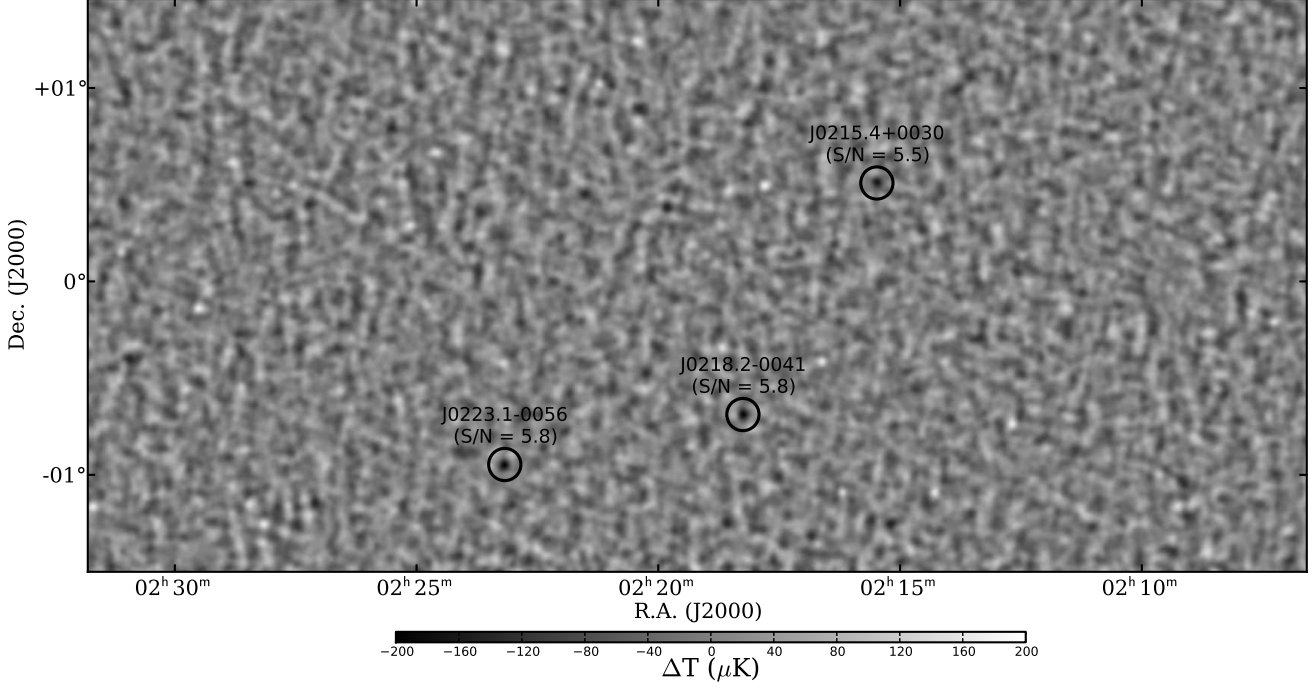


Figure 3. Section of the 148 GHz map (covering 18.7 deg^2) match-filtered with a GNFW profile of scale $\theta_{500} = 5''.9$. Point sources are removed prior to filtering. Three optically confirmed clusters with $S/N > 4.9$ are highlighted (see Table 7). Within this area, there are an additional 11 candidates ($4 < S/N < 4.9$) which are not confirmed as clusters in the SDSS data (and thus may be spurious detections or high-redshift clusters).

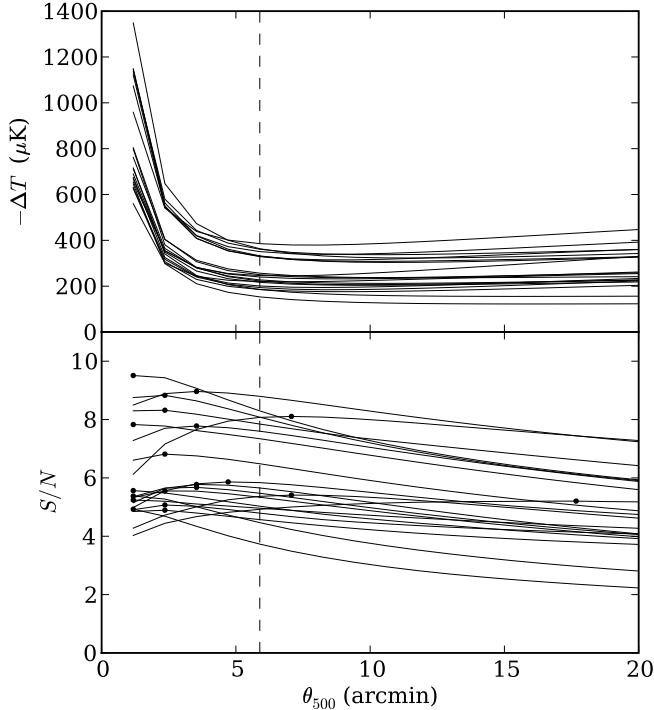


Figure 4. Central decrement and signal to noise ratio as a function of filter scale for the 20 clusters in S82 detected with peak $S/N > 5$. *Top panel:* Although the central decrement is a model-dependent quantity, the value tends to be stable for filter scales of $\theta_{500} > 3'$. *Bottom panel:* On each curve, the circular point identifies the filter scale at which the peak S/N was observed. The vertical dashed line shows the angular scale chosen for cluster property and cosmology analysis, $\theta_{500} = 5''.9$. Despite the apparent gap near $S/N \approx 6$, the clusters shown represent a single population.

3. RECOVERED CLUSTER PROPERTIES

In this section we develop a relationship between cluster mass and the expected signal in the ACT filtered maps. The form of the scaling relationship between the SZ observable and the cluster mass is based on the UPP, and parameters of that relationship are studied using models of cluster physics and dynamical mass measurements. We obtain masses for the ACT Equatorial clusters assuming a representative set of parameters.

3.1. Profile Based Amplitude Analysis

Scaling relations between cluster mass and cluster SZ signal strength are often expressed in terms of bulk integrated Compton quantities, such as Y_{500} , which are expected to be correlated to mass with low intrinsic scatter (e.g., Motl et al. 2005; Reid & Spergel 2006). Due to projection effects, and the current levels of telescope resolution and survey depth, measurements of Y_{500} for individual clusters can be obtained only by comparing the microwave data to a simple, parametrized model for the cluster pressure profile. Such fits may be done directly, or indirectly as part of the cluster detection process through the application of one or more matched filters (where the filters are “matched” in the sense of being tuned to a particular angular scale). In such comparisons, the inferred values of Y_{500} are very sensitive to the assumed cluster scale (i.e., θ_{500}^1), and this scale is poorly constrained by microwave data alone.

Recent microwave survey instruments make use of spatial filters to both detect and characterize their cluster samples, coping with θ_{500} uncertainty in different

¹ $M_{500c} = (4\pi/3) \times 500\rho_c(z)R_{500}^3$; $\theta_{500} = R_{500}/D_A(z)$.

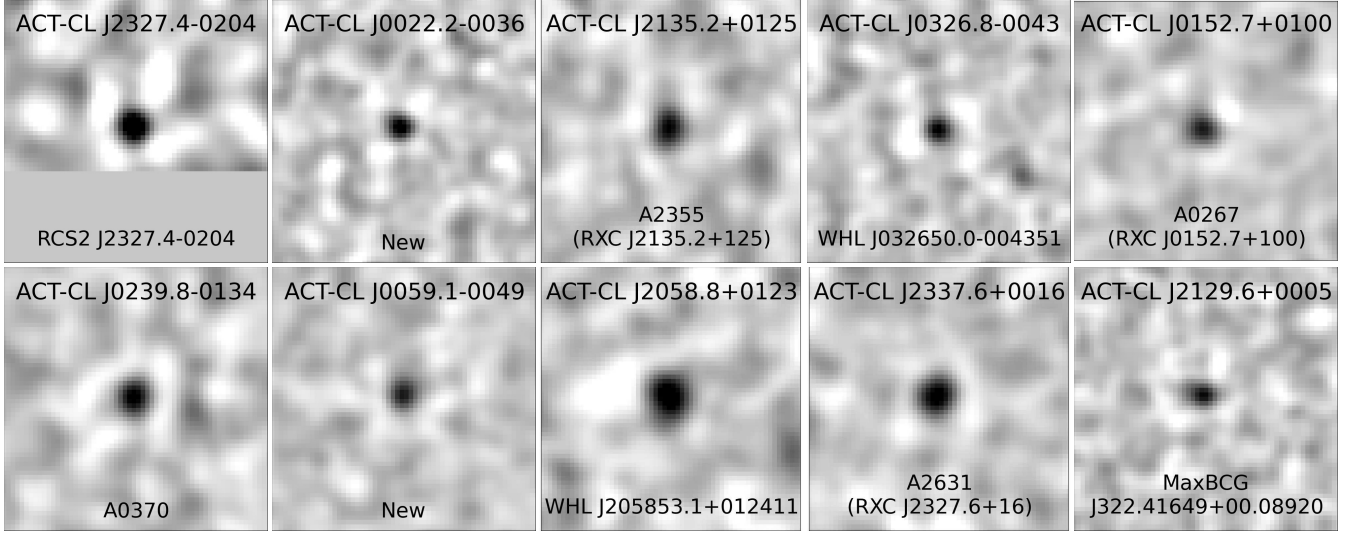


Figure 5. Postage stamp images (30' on a side) for the 10 highest S/N detections in the catalog (see Table 7), taken from the filtered ACT maps. The clusters are ordered by detection S/N, from top left to bottom right, and each postage stamp shown is filtered at the scale which optimizes the detection S/N. Note that J2327.4–0204 is at the edge of the map. The greyscale is linear and runs from $-350 \mu\text{K}$ (black) to $+100 \mu\text{K}$ (white).

ways. For example, the *Planck* team uses X-ray luminosity based masses (Planck Collaboration 2011a) as well as more detailed X-ray and weak lensing studies (Planck Collaboration et al. 2013) to constrain R_{500} , and obtain Y_{500} measurements assuming profile shapes described by the UPP.

In cases where suitable X-ray or optical constraints on the cluster scale are not available, authors have constructed empirical scaling relations based on alternative SZ statistics, such as the amplitude returned by some particular filter (Sehgal et al. 2011), or the maximum S/N over some ensemble of filters (Vanderlinde et al. 2010). Recognizing that the cluster angular scale is poorly constrained by the filter ensemble, recent work from the South Pole Telescope has included a marginalization over the results returned by the ensemble of filters (e.g., Story et al. 2011; Reichardt et al. 2013). Such approaches rely on simulated maps to guide the interpretation of their results.

For the purposes of using the SZ signal to understand scaling relations and to obtain cosmological constraints, we develop an approach in which the cluster SZ signal is parametrized by a single statistic, obtained from the ACT map that has been filtered using $\Psi_{5',9}(\mathbf{k})$. Instead of using simulations to inform our interpretation of the data, we develop a framework where the SZ observable is expressed in terms of the parameters of some underlying model for the cluster pressure profile. In particular, we model the clusters as being well described, up to some overall adjustments to the normalization and mass dependence, by the UPP (see Section 2.2).

An estimate of the cluster central Compton parameter, based only on the non-relativistic SZ treatment, is given by

$$\tilde{y}_0 \equiv \frac{\Delta T}{T_{\text{CMB}}} f_{\text{SZ}}^{-1}(m=0, z=0), \quad (10)$$

where $f_{\text{SZ}}(m=0, z=0) = -0.992$ as explained in Sec-

tion 2.2. This “uncorrected” central Compton parameter is used in place of ΔT to develop an interpretation of the SZ signal. This quantity is uncorrected in the sense that it is associated with the fixed angular scale filter and does not include a relativistic correction.

For a cluster with SZ signal described by equation (7), the value of \tilde{y}_0 that we would expect to observe by applying the filter $\Psi_{5',9}$ to the beam-convolved map is

$$\tilde{y}_0 = 10^{A_0} E(z)^2 m^{1+B_0} Q(\theta_{500}/m^{C_0}) f_{\text{rel}}(m, z) \quad (11)$$

where

$$Q(\theta) = \int \frac{d^2 k}{(2\pi)^2} \Psi_{5',9}(\mathbf{k}) B(\mathbf{k}) \int d^2 \theta' e^{i\boldsymbol{\theta}' \cdot \mathbf{k}} \tau(\theta'/\theta). \quad (12)$$

is the spatial convolution of the filter, the beam, and the cluster’s unit-normalized integrated pressure profile. We note that in this formalism, $\theta_{500} = R_{500}/D_A(z)$ is determined by the cluster mass and the cosmology (rather than being some independent parameter describing the angular scale of the pressure profile).

The response function $Q(\theta)$ for the Equatorial clusters is shown in Figure 6. It encapsulates the bias incurred in the central decrement estimate due to a mismatch between the true cluster size and the size encoded in the filter, for the family of clusters described by the UPP. While this bias is in some cases substantial ($Q \approx 0.3$ for clusters with $\theta_{500} \approx 1.5'$), the function $Q(\theta)$ is not strongly sensitive to the details of the assumed pressure profile (as demonstrated in Section 3.3), and the assumptions underlying this approach are not a significant departure from other analyses that rely on a family of cluster templates to extract a cluster observable.

Equation (11) thus relates \tilde{y}_0 to cluster mass and redshift while accounting for the impact of the filter on clusters whose angular size is determined by their mass and redshift. This relationship can be seen in Figure 7.

The essence of our approach, then, is to filter the maps

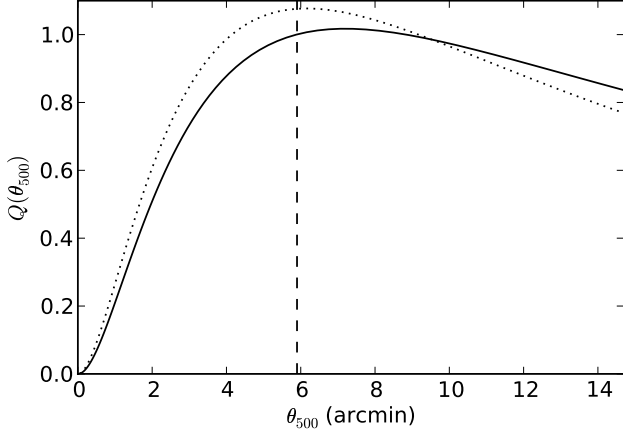


Figure 6. The response function used to reconstruct the cluster central decrement as a function of cluster angular size (solid line). At $\theta_{500} = 5.9$, the filter is perfectly matched and $Q = 1$. At scales slightly above 5.9 , $Q > 1$ because such profiles have high in-band signal despite being an imperfect match, overall, to the template profile. For the definition of Q , see Section 3.1. Dotted line shows analogous function computed under the assumption that the cluster signal is described by the *Planck* Pressure Profile (see Section 3.3).

with $\Psi_{5.9}(k)$ and for each confirmed cluster obtain ΔT and its error. This is equivalent to measuring \tilde{y}_0 , which can then be compared to the right hand side of equation (11). If the cluster redshift is also known, then for a given cosmology the only free parameter in the expression for \tilde{y}_0 is the mass parameter, m .²

We refer to this alternative approach, where a family of pressure profiles is used to model the amplitude of a source in a filtered map, as “Profile Based Amplitude Analysis” (PBAA). While we have applied a filter tuned to a particular angular scale, the effects of angular diameter distance, telescope beam, and the spatial filtering are modeled in a way that accounts for the (mass and redshift dependent) cluster angular scale. For a given cosmology, and having computed $Q(\theta)$ based on the UPP, the parameters (A_0 , B_0 , and C_0) of the scaling relation between \tilde{y}_0 and mass have a physical significance and can be verified through measurements of \tilde{y}_0 , redshift, and mass for a suitable set of clusters.

While the usage of a single filter clearly simplifies data processing, the most compelling advantage is that one does not suffer from inter-filter noise bias. For example, when optimizing filter scale, a CMB cold spot near a cluster candidate will draw the preferred filter to larger angular scales than would the isolated cluster signal. The preferred filter scale is thus driven by the amplitude of local noise excursions as much as it is driven by the cluster signal. In a single filter context, a CMB cold spot affects the amplitude measurement by contributing spurious signal to the apparent cluster decrement; but if CMB hot and cold spots are equally likely, and uncorrelated with cluster positions, then the CMB as a whole acts as a Gaussian noise contribution to cluster signal. The effects of coherent noise on large scales are thus somewhat

² With \tilde{y}_0 and z measurements in hand, one could certainly proceed to solve equation (11) to obtain a mass for each cluster. Because we are treating mass as one of the independent variables, however, such an approach would produce biased mass estimates; see Section 3.2.

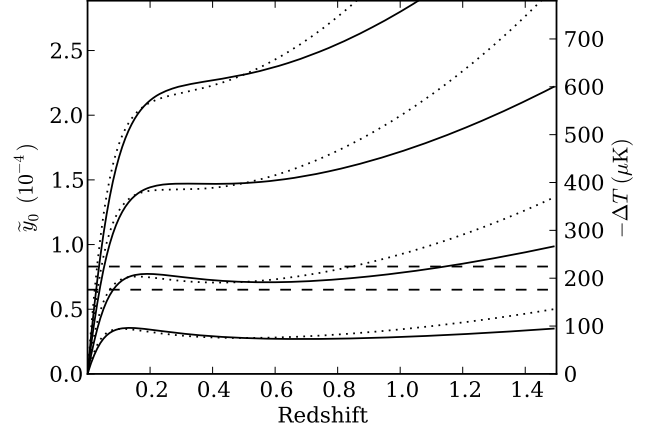


Figure 7. Prediction, based on the UPP, for cluster signal in a map match-filtered with $\theta_{500} = 5.9$, in units of uncorrected central Compton parameter \tilde{y}_0 and apparent temperature decrement $-\Delta T$ at 148 GHz (Section 3.1). Solid lines trace constant masses of, from top to bottom, $M_{500c} = 10^{15}, 7 \times 10^{14}, 4 \times 10^{14}$, and $2 \times 10^{14} h_{70}^{-1} M_{\odot}$. Dotted lines are for the same masses, but with the scaling relation parameter $C = 0.5$ to show the redshift sensitivity to this parameter. Above $z \approx 0.5$, the scaling behavior of the observable \tilde{y}_0 with redshift is stronger for higher masses because their angular size is a better match to the cluster template and the redshift dependence in Q does not attenuate the scaling of the central decrement, $y_0 \propto E(z)^2$, as much as it does for lower masses. The dashed lines correspond to $S/N > 4$ and $S/N > 5.1$, based on the median noise level in the S82 region.

better behaved if we do not permit the re-weighting of angular scales to maximize the apparent signal.

To achieve the goal of detecting as many clusters as possible, one should certainly explore a variety of candidate cluster profiles and apply an ensemble of matched filters. However, for cosmological studies, or when trying to understand the relationship between observables in samples that are selected based on one of the observables under study, it is critical to understand the selection function that describes how the population of objects in the sample relates to the broader population of objects in the universe. While we sacrifice a certain amount of signal when choosing a single filter scale to use for cosmological and scaling relation analysis, we benefit from having a simpler selection function.

Much of our approach can be simply generalized so that a suite of filters are used, but with each filter intended to correspond to a particular redshift interval. The redshift-dependent angular scales might be selected to match clusters of a particular mass, for example. Such an approach benefits from the lack of inter-scale noise bias, because there is no data-based optimization over angular scale. However, interpretation of the signal is then complicated by the need to consider the impact of the full suite of filters on the cluster signal and noise models. Such an approach is tractable, but is not considered in this work.

We also note that $\theta_{500} = 5.9$ is chosen because it lies in a regime of θ_{500} where the measured \tilde{y}_0 statistic for our high significance clusters is approximately constant. Our approach does not require this, however, and could instead have used a filter corresponding to some smaller θ_{500} , where signal to noise ratios are, on average, slightly higher.

In order to compare the predictions of the UPP based

formalism to models and other data sets, we introduce a more general relationship relating cluster mass to the uncorrected central Compton parameter. We allow for variations in the normalization, mass dependence, and scale evolution through parameters A , B , and C and model \tilde{y}_0 as

$$\tilde{y}_0 = 10^{A_0+A} E(z)^2 (M/M_{\text{pivot}})^{1+B_0+B} \times Q \left[\left(\frac{1+z}{1.5} \right)^C \theta_{500}/m^{C_0} \right] f_{\text{rel}}(m, z). \quad (13)$$

To abbreviate the argument to $Q(\theta)$, we will often simply write $Q(m, z)$. The exponents (A_0, B_0, C_0) remain fixed to the UPP model values of equations (6) and (7), except where otherwise noted. For a given data set or model, M_{pivot} will be chosen to reduce covariance in the fit values of A and B . In Table 1 we present the fit parameters for various models and data sets discussed in subsequent sections. In order to compare fits from data sets with different M_{pivot} , we also compute the normalization exponent A_m associated with $M_{\text{pivot}} = 3 \times 10^{14} h_{70}^{-1} \text{M}_{\odot}$ for each data set. In these terms, the UPP model described by equation (11) corresponds to $(A_m, B, C) = (0, 0, 0)$.

In cases where independent surveys each measure \tilde{y}_0 values for a cluster based on following the algorithm described here, the \tilde{y}_0 measurements should not, in general, be compared directly. This is because the filter $\Psi_{\theta_{500}}$ and the resulting bias factor Q depend on the telescope beam and the noise spectra of the resulting maps. However, it is possible to filter one set of maps in a way that matches the beam and filtering of a preceding analysis. In such cases an independent measurement of \tilde{y}_0 is obtained, which may be compared between experiments. Such comparisons are likely to be most interesting in cases where two telescopes have similar resolution.

Alternatively, \tilde{y}_0 measurements and redshifts may be converted, for some particular values of the scaling relation parameters, into physical parameters such as M_{500c} , Y_{500} , or the corrected y_0 . Such derived quantities may be compared between experiments that probe different angular scales. The physical parameters can be updated as one’s understanding of the scaling relation parameters is improved. The use of \tilde{y}_0 thus facilitates the re-use of the data in analyses that explore different models for the cluster signal.

The uncorrected central Compton parameter measurements (\tilde{y}_0) for the ACT Equatorial clusters are presented in Table 7. They are used in subsequent sections to estimate cluster properties (such as corrected SZ quantities and mass) and to constrain cosmological parameters. For the Southern cluster sample, analogous measurements are presented in the Appendix. Between the Equatorial and Southern cluster samples, the ACT collaboration has reported a total of 91 optically confirmed, SZ detected clusters.

3.2. Cluster Mass and SZ Quantity Estimates

Given measurements of cluster \tilde{y}_0 and redshift, one cannot naively invert Equations (11) or (13) to obtain a mass estimate. Because of intrinsic scatter, measurement noise, and the non-trivial (very steep) cluster mass function, the mean mass at fixed SZ signal \tilde{y}_0 will be lower than the mass whose mean predicted SZ signal is

\tilde{y}_0 . The bias due to noise is often referred to as “flux boosting” and can be corrected in a Bayesian analysis that accounts for the underlying distribution of flux densities (Coppin et al. 2005). The bias due to intrinsic scatter, however, is not restricted to the low significance measurements. Considering the population of clusters (at fixed redshift) in the $(\log m, \log \tilde{y}_0)$ plane, the locus $\langle \log m | \log \tilde{y}_0 \rangle$ (i.e., the expectation value of the log of the mass for a given central Compton parameter) lies at lower mass than $\langle \log \tilde{y}_0 | \log m \rangle$. This phenomenon has been discussed in the context of galaxy cluster surveys by, e.g., Mantz et al. (2010a, see also the review by Allen, Evrard, & Mantz 2011).

The mass of a cluster, however, can be estimated if one has an expression for the cluster mass function. We adapt the Bayesian framework of Mantz et al. (2010a) to this purpose. The posterior probability of the mass parameter m given the observation \tilde{y}_0^{ob} is

$$P(m | \tilde{y}_0^{\text{ob}}) \propto P(\tilde{y}_0^{\text{ob}} | m) P(m) = \left(\int d\tilde{y}_0^{\text{tr}} P(\tilde{y}_0^{\text{ob}} | \tilde{y}_0^{\text{tr}}) P(\tilde{y}_0^{\text{tr}} | m) \right) P(m) \quad (14)$$

where \tilde{y}_0^{tr} represents the “true” SZ signal in the absence of noise, $P(\tilde{y}_0^{\text{ob}} | \tilde{y}_0^{\text{tr}})$ is the distribution of \tilde{y}_0^{ob} given \tilde{y}_0^{tr} and the observed noise $\delta\tilde{y}_0^{\text{ob}}$, and $P(m)$ is proportional to the distribution of cluster masses at the cluster redshift. The distribution $P(\tilde{y}_0^{\text{tr}} | m)$ of the noise-free cluster signal \tilde{y}_0^{tr} is assumed to be log-normal about the mean relation given by Equation (13), i.e.,

$$\log \tilde{y}_0^{\text{tr}} \sim N(\log \tilde{y}_0(m, z); \sigma_{\text{int}}^2) \quad (15)$$

with σ_{int} denoting the intrinsic scatter.

We use the results of Tinker et al. (2008) to compute the cluster mass function, assuming the fiducial Λ CDM cosmology, with $\sigma_8 = 0.8$. Scaling the mass function by the comoving volume element at fixed solid angle, we obtain $dN(< m, z)/dz$, the number of clusters, per unit solid angle and per unit redshift, that have mass less than m . The probability of a cluster in this light cone having mass m and redshift z may then be taken as $P(m, z) \propto d^2 N(< m, z)/dz dm$. We account for redshift uncertainty by marginalizing the cluster mass function $P(m, z)$ over the cluster’s redshift error to obtain an effective $P(m)$ at the observed cluster redshift.

The marginalized masses obtained using Equation (14) are presented in Table 8. For the ACT Southern cluster sample, these masses are presented in the Appendix. In each case, masses are presented for the UPP scaling relation as well as for scaling relation parameters fit to SZ signal models (see Section 3.4) or dynamical mass data (see Section 3.5).

A similar approach may be taken to estimate the true values of SZ quantities, given the observed quantities. In this case we are effectively only undoing the noise bias, while intrinsic scatter affects the underlying population function. We are interested in

$$P(\tilde{y}_0^{\text{tr}} | \tilde{y}_0^{\text{ob}}) \propto P(\tilde{y}_0^{\text{ob}} | \tilde{y}_0^{\text{tr}}) P(\tilde{y}_0^{\text{tr}}) = P(\tilde{y}_0^{\text{ob}} | \tilde{y}_0^{\text{tr}}) \int dm P(\tilde{y}_0^{\text{tr}} | m) P(m). \quad (16)$$

The resulting probability distribution is used to obtain

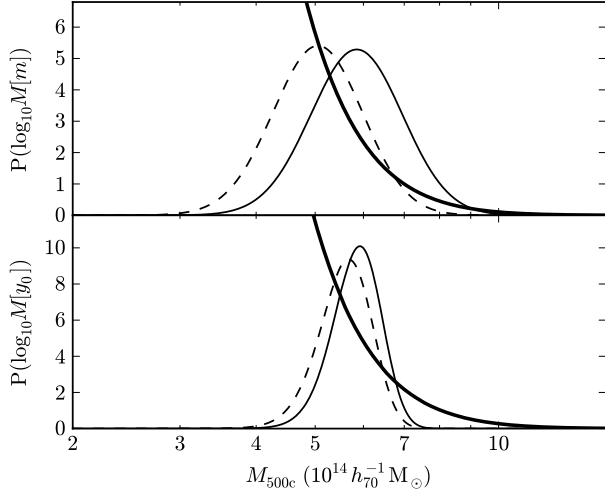


Figure 8. Example probability distributions for cluster mass (upper panel) and SZ signal strength parametrized as a mass according to equation (13) (lower panel). The solid line PDF is the result of a direct inversion of the scaling relation described by equation (13). The corrected PDF (dashed line) is obtained by accounting for the underlying population distribution (bold line; arbitrary normalization). The correction is computed according to equation (14) for the upper panel, and according to equation (16) for the lower panel. Curves shown correspond to ACT-CL J0022.2–0036.

marginalized estimates of y_0 , θ_{500} (which should be interpreted as giving the scale of the pressure profile rather than the scale of the mass density profile), Y_{500} (estimated within the SZ-inferred θ_{500}) and Q . These quantities are presented in Table 8, for the UPP scaling relation parameters.

In Figure 8 we demonstrate the impact of the steep mass function on the inferred mass and SZ quantities. As the measurement noise decreases, the \tilde{y}_0 measurements are less biased; but any intrinsic scatter in the \tilde{y}_0 – M relation will lead to bias in the naively estimated mass.

3.3. The Planck Pressure Profile

In Planck Collaboration (2012a), data for 62 massive clusters from the *Planck* all-sky Early Sunyaev-Zel’dovich cluster sample (Planck Collaboration 2011a) are analyzed to obtain a “*Planck* pressure profile” (PPP) based on measurements of the SZ signal. Integrating the PPP along lines of sight, the central pressure is 20% lower than the UPP but is higher than the UPP outside of $0.5R_{500}$. *Planck* finds overall consistency between results obtained with the UPP and the PPP.

We assess the difference in inferred mass due to this alternative pressure profile by re-analyzing the ACT \tilde{y}_0 using the PPP. A bias function Q is computed as in Equation (12), but with the normalized Compton profile τ associated to the PPP (see Figure 6). We additionally determine scaling parameters, compatible with Equation (7), of $(10^{A_0}, B_0, C_0) = (4.153 \times 10^{-5} h_{70}^{1/2}, 0.12, 0)$. Note that while the bias function shows increased sensitivity, compared to the UPP, for $\theta_{500} < 9'$, this is compensated for by the lower normalization factor 10^{A_0} . For the Equatorial cluster sample, we find the PPP masses to be well described by a simple mean shift of $M_{500c}^{\text{PPP}} = 1.015 M_{500c}^{\text{UPP}}$, with 3% RMS scatter. Note that this is only a statement about the dependence of the ACT results on the assumed pressure profile; experiments that

probe different angular scales may be more or less sensitive to such a change.

While the change in inferred masses is in this case negligible, we reiterate that our fully parametrized relationship between SZ signal and mass (Equation (13)) allows for freedom in the normalization, mass dependence, and evolution of cluster concentration with redshift. Mass or cosmological parameter estimation can be computed after fixing these parameters based on any chosen pressure profile, model, simulation, or data set; all that is required is to compensate for the mismatch of our assumed pressure profile to the true mean pressure profile.

3.4. Scaling Relation Calibration from SZ Models

The previous sections have described a general approach that relates cluster mass and redshift to SZ signal in a filtered map, given values for the scaling relation parameters. In this section we obtain scaling relation parameters based on three models for cluster gas physics. While the ACT data will be interpreted using each of these results, we do not yet consider any ACT data explicitly.

Current models for the SZ signal from clusters include contributions from non-thermal pressure support, star formation, and energy feedback and are calibrated to match detailed hydrodynamical studies and X-ray or optical observations (Shaw et al. 2010; Bode et al. 2012). Such models provide a useful testing ground for the assumptions and methodology of our approach to predicting SZ signal based on cluster mass. While models may suffer from incomplete modeling of relevant physical effects, they are less vulnerable to some measurement biases (e.g., by providing a cluster mass and alleviating the need for secondary mass proxies). In order to explore the current uncertainty in the SZ–mass scaling relation, we consider simulated sky maps based on three models of cluster SZ signal that include different treatments of cluster physics.

Our study will center on maps of SZ signal produced from the SZ models and structure formation simulations of Bode et al. (2012, hereafter B12). The N-body simulations (Bode & Ostriker 2003) are obtained in a Tree-Particle-Mesh framework, in which dark matter halos have been identified by a friends-of-friends algorithm. The intracluster medium (ICM) of massive halos is subsequently added, following a hydrostatic equilibrium prescription, and calibrated to X-ray and optical data (Bode, Ostriker, & Vikhlinin 2009). The density and temperature of the ICM of lower mass halos and the IGM are modeled as a virialized ideal gas with density (assuming cosmic baryon fraction $\Omega_b/\Omega_m = 0.167$) and kinematics that follow the dark matter.

To complement the model of B12, we also consider the Adiabatic and Nonthermal20 models described in Trac et al. (2011), which make use of the same N-body results as B12. In the Adiabatic model the absence of feedback and star formation leads to a higher gas fraction than in the B12 model. In the Nonthermal20 model, 20% of the hydrostatic pressure is assumed to be nonthermal, leading to substantially less SZ signal compared to the B12 model. The SZ-mass relations derived from these two models are thus interpreted as, respectively, upper and lower bounds on the SZ signal.

The model of B12 differs from those in Trac et al.

(2011) through a more detailed handling of non-thermal pressure support, which is tied to the dynamical state of the cluster and is allowed to vary over the cluster extent. Both B12 and the similar treatment of Shaw et al. (2010) make use of hydrodynamic simulations (Nagai et al. 2007; Lau et al. 2009; Battaglia et al. 2012) to understand these non-thermal contributions.

To calibrate our scaling relation approach to these models, we make use of light-cone integrated maps of the thermal and kinetic SZ at 145 GHz (constructed as in Sehgal et al. 2010), and the associated catalog of cluster positions and masses. A set of 192 non-overlapping patches of area 18.2 deg^2 each are extracted from the simulated map, and convolved with the ACT 148 GHz beam to simulate observation with the telescope. The maps are then filtered with the same filter $\Psi_{5.9}(\mathbf{k})$ that was used for the ACT Equatorial clusters. Because the filtering is a linear operation, it is counter-productive to the purpose of calibration and intrinsic scatter estimation to add noise (CMB, detector noise) to the simulated signal map, and so we do not. The uncorrected central decrements are extracted and used to constrain the parameters of Equation (13). To probe the high-mass regime, only the 257 clusters having $M_{500c} > 4.3 \times 10^{14} h_{70}^{-1} M_{\odot}$ and $0.2 < z < 1.4$ are considered; the fit is performed around $M_{\text{pivot}} = 5.5 \times 10^{14} h_{70}^{-1} M_{\odot}$. The intrinsic scatter of the relation is also obtained from the RMS of the residuals. For the B12 model, the residuals of the fit are plotted against mass in Figure 9.

For each of the three models, fit parameters are presented in Table 1. The mass dependence is consistent, in all cases, with the UPP prediction ($B \approx 0$), and additional redshift dependence is only present in the Nonthermal20 model. Only the Adiabatic model is consistent in its normalization with the UPP value. This is despite the explicit calibration, in B12, of the mean pressure profile to the UPP at R_{500} . The origin of this inconsistency is due to the relative shallowness of the mean pressure profile in B12 compared to the UPP. Thus, the profiles in B12 have less total signal within R_{500} , where ACT is sensitive.

The scaling relation parameters obtained for the Adiabatic model are sufficiently close to zero (i.e., to the UPP scaling prediction), that we drop them from further consideration. While the B12 normalization lies somewhat below the UPP prediction, we note that even lower normalizations (such as that found in the Nonthermal20 model) are favored by recent measurements of the SZ contribution to the CMB angular power spectrum (Dunkley et al. 2011; Reichardt et al. 2012).

We thus proceed to consider quantities derived from each of the UPP, B12, and Nonthermal20 scaling relation parameter sets. Mass estimates for the B12 and Nonthermal20 models are computed for the ACT Equatorial cluster sample as described in Section 3.2, and are presented alongside the UPP estimates in Table 8.

3.5. Scaling Relation Calibration from Dynamical Masses

Sifón et al. (2012, hereafter S12) measure galaxy velocity dispersions to obtain mass estimates for clusters in ACT’s Southern field. S12 also present the uncorrected central Compton parameter measurements \tilde{y}_0 and the

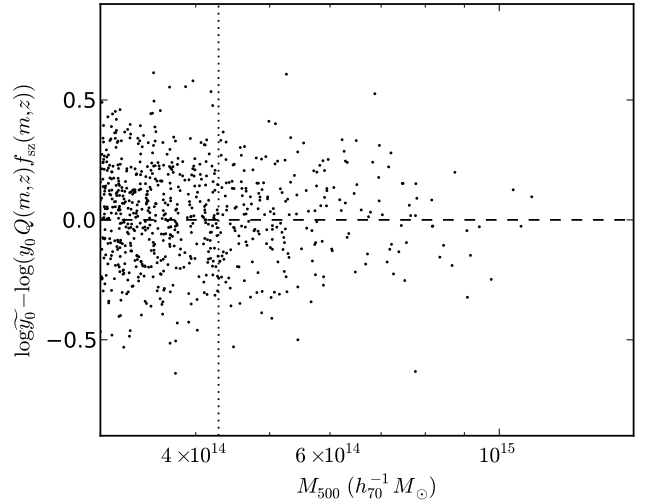


Figure 9. Residuals of the scaling relation fit for the B12 model (Section 3.4). Only clusters with $0.2 < z < 1.4$ and $M_{500c} > 4.3 \times 10^{14} h_{70}^{-1} M_{\odot}$ (indicated by dotted line) are used for the fit. The scatter in the relation is measured from the RMS of the residuals.

corrected versions y_0 obtained as described in Section 3.2 and presented in the Appendix. S12 perform power law fits of both the uncorrected (\tilde{y}_0) and corrected (y_0) central Compton parameters to the dynamical masses to establish scaling relations for those cluster observables.

Here, we fit the full scaling relation of equation (13) to the dynamical mass data for the 16 $z > 0.3$ clusters from the Southern field that were detected by ACT and observed by S12. We do not use the scaling relation as estimated in S12, because the parametrization of the scaling relation in that study is different. Also, the linear regression that is used in S12 (the bisector algorithm of Akritas & Bershady (1996)) is not suited to predicting the SZ signal given only the mass, which is the aim in formulating the cluster abundance likelihood in Section 5.³

Dynamical masses are estimated in S12 for each cluster based on an average of 60 member galaxy spectroscopic redshifts. For each cluster, the galaxy velocity dispersion S_{BI} is interpreted according to the simulation based results of Evrard et al. (2008), who find that the dark matter velocity dispersion σ_{DM} is related to the halo mass M_{200c} by

$$\sigma_{\text{DM}} = \sigma_{15} \left(\frac{0.7 \times E(z) M_{200c}}{10^{15} h_{70}^{-1} M_{\odot}} \right)^{\alpha}, \quad (17)$$

where $\sigma_{15} = 1082.9 \pm 4 \text{ km s}^{-1}$ and $\alpha = 0.3361 \pm 0.0026$. By inverting equation (17) and assuming that $S_{\text{BI}} = \sigma_{\text{DM}}$, S12 obtain dynamical estimates, which we will denote by M_{200c}^{dyn} , of the halo mass. As discussed in S12 and Evrard et al. (2008), the systematic bias between galaxy and dark matter velocity dispersions, $b_v \equiv S_{\text{BI}}/\sigma_{\text{DM}}$, is believed to be within 5% of unity. To account for this, and any other potential systematic biases in the dynamical

³ The cluster abundance likelihood assumes a scaling relation where \tilde{y}_0 is the dependent variable and takes full account of the mass function; in this section we will use the likelihood-based approach of Kelly (2007) which includes iterative estimation of the distribution of the independent variable.

Table 1
Scaling relation parameters

Description	M_{pivot} ($10^{14} h_{70}^{-1} M_{\odot}$)	A	A_m	B	C	σ_{int}
Universal Pressure Profile (UPP) Models (§3.4)	–	–	0	0	0	0.20 ^a
B12	5.5	0.111 ± 0.021	-0.17 ± 0.06	-0.00 ± 0.20	-0.04 ± 0.37	0.20
Nonthermal20	5.5	-0.003 ± 0.020	-0.29 ± 0.06	0.00 ± 0.20	0.67 ± 0.47	0.21
Adiabatic	5.5	0.241 ± 0.020	-0.02 ± 0.06	-0.08 ± 0.20	0.10 ± 0.43	0.21
Dynamical mass data (§3.5)						
All clusters	7.5	0.237 ± 0.060	-0.21 ± 0.21	0.03 ± 0.51	0	0.31 ± 0.13
Excluding J0102	7.5	0.205 ± 0.045	-0.11 ± 0.15	-0.28 ± 0.35	0	0.19 ± 0.10
Full cosmological MCMC (§5.3)						
Λ CDM model	7.0	0.079 ± 0.135	-0.45 ± 0.19	0.36 ± 0.36	0.43 ± 0.62	0.42 ± 0.19
w CDM model	7.0	0.065 ± 0.153	-0.46 ± 0.21	0.36 ± 0.35	0.34 ± 0.65	0.45 ± 0.20

Note. — Scaling relation parameters, fit to: (i) various SZ models (see Section 3.4); (ii) the dynamical mass data of Sifón et al. (2012) (Section 3.5); (iii) a cosmological MCMC including WMAP data along with the ACT Southern and Equatorial cluster samples and dynamical mass data (Section 5.3). Scaling relation parameters A , B , and C are defined as in equation (13), with M_{pivot} chosen to yield uncorrelated A and B . A_m is the normalization parameter corresponding to $M_{\text{pivot}} = 3 \times 10^{14} h_{70}^{-1} M_{\odot}$ and may be compared among rows. Parameters A_m , B and C indicate the level of deviation from the predictions based on the Universal Pressure Profile of Arnaud et al. (2010) (equations (6) and (7); shown for reference). The intrinsic scatter σ_{int} is defined as the square root of the variance of the observed $\log \tilde{y}_0$, in the absence of noise, relative to the mean relation defined by equation 13. The parameter C is fixed to 0 when fitting scaling relations to dynamical masses.

^a This value, based on the B12 model value, is used for results computed for the UPP scaling relation parameters that also require a value for the intrinsic scatter.

ical mass estimates, we introduce the parameter

$$\beta^{\text{dyn}} \equiv \left\langle \frac{M_{200c}^{\text{dyn}}}{M_{200c}} \right\rangle. \quad (18)$$

Based on a velocity dispersion bias of $b_v = 1.00 \pm 0.05$, the equivalent mass bias is $\beta^{\text{dyn}} = 1.00 \pm 0.15$. For the present discussion, we disregard this bias in order to distinguish its effects from other calibration issues. However, in the cosmological parameter analysis of Section 5 we include β^{dyn} as a nuisance parameter and discuss its impact on the cosmological parameter constraints.

The \tilde{y}_0 measurements associated with the Southern sample of clusters are obtained using a filter matched to the noise power spectrum of the Southern field maps used in Sifón et al. (2012). Thus, while the signal template is the same, the full form of the filter Ψ and the associated response function Q differ slightly from the ones used on the Equatorial data. We apply the same correction for selection bias that was used by S12, and denote the corrected values as $\tilde{y}_0^{\text{corr}}$.

To convert the dynamical masses to M_{500c} values, we model the cluster halo with a Navarro-Frenk-White profile (Navarro et al. 1995) with concentration parameters and uncertainties obtained from the fits of Duffy et al. (2008). For the fit we use a pivot mass of $7.5 \times 10^{14} h_{70}^{-1} M_{\odot}$, and fix the parameter C to 0 (otherwise the fit is poorly constrained). We use the likelihood-based approach of Kelly (2007) to fit for the intrinsic scatter along with the parameters A and B , given measurement errors on both independent and dependent variables. The scatter is modeled, as before, as an additional Gaussian random contribution to $\log \tilde{y}_0$ relative to the mean relation $\langle \tilde{y}_0 | m, z \rangle$.

The fit parameters are presented in Table 1. A substantial contribution to the scatter in the dynamical mass fits comes from the exceptional, merging cluster ACT-CL J0102–4915 (“El Gordo,” Menanteau et al. 2012): when this cluster is excluded from the fit, the scatter drops to 0.19 ± 0.10 , which is more consistent with fits based solely

on models.

In Figure 10 we plot the cluster SZ measurements against the dynamical masses, along with the best fit scaling relation. The scaling relations from the UPP and from the parameters fit to the B12 and Nonthermal20 models are also shown. While the fit parameters for the dynamical mass data are consistent with either the B12 or Nonthermal20 models, the dynamical mass data lie well below the mean scaling relation predicted by the UPP. These results reinforce the need to consider a broad range of possible scaling relation parameters, within our framework based on the UPP. We note, however, that the possibility of a systematic difference between dynamical masses and other mass proxies must be considered when comparing the parameters obtained in this section to other results.

3.6. Completeness Estimate

In this section we estimate the mass, as a function of redshift, above which the ACT cluster sample within SDSS Stripe 82 (which we will refer to as the S82 sample) is 90% complete. We consider the S82 sample as a whole ($S/N > 4$), and also consider the subsample that has complete high redshift follow-up ($S/N > 5.1$).

For a cluster of a given mass and redshift, we use the formalism of Section 3.1 to predict its SZ signal and to infer the amplitude $\tilde{y}_{\theta_{500}}$ that we would expect to measure in a map to which filter $\Psi_{\theta_{500}}$ has been applied, in the absence of noise and intrinsic scatter. We then assume that the cluster occupies a map pixel with a particular noise level, and consider all possible realizations of the noise (assumed to be Gaussian) and intrinsic scatter, to get the probability distribution of observed $\tilde{y}_{\theta_{500}}$ values. Applying the sample selection criteria, we thus obtain the probability of detection for this mass, redshift, filter scale, and map noise level.

We obtain the total probability that the cluster will be detected at a given filter scale by averaging over the distribution of noise levels in the corresponding filtered map. The distribution of noise levels in the real filtered

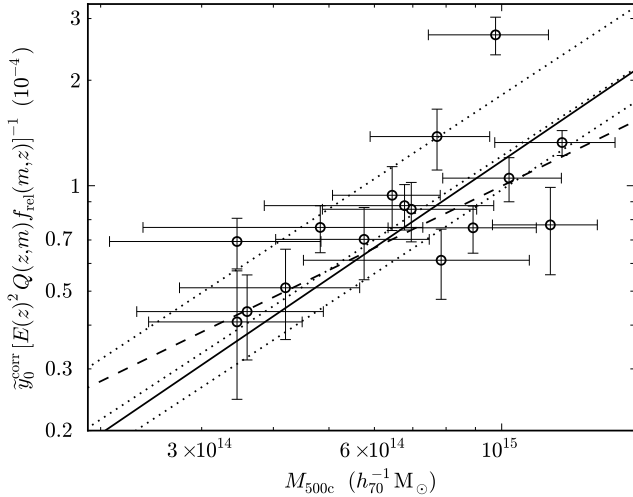


Figure 10. Corrected central Compton parameter vs. dynamical mass for the 16 ACT-detected clusters presented in Sifón et al. (2012) for the Southern sample. Values on y -axis include factor of $E(z)^{-2}$, which arises in the derivation of y_0 in self-similar models. The high signal outlier is “El Gordo” (ACT-CL J0102–4915, Menanteau et al. 2012), an exceptional, merging system. The solid line represents the best fit of equation (13) with $M_{\text{pivot}} = 7.5 \times 10^{14} h_{70}^{-1} M_{\odot}$. The dashed line is for the fit with J0102–4915 excluded. Dotted lines, from top to bottom, are computed for scaling relation parameters corresponding to the UPP, B12 and Nonthermal20 ($z = 0.5$) models.

maps is used to perform this computation. To obtain a total detection probability for the cluster, we take the maximum of the detection probabilities over the ensemble of filters. This assumes that noise and intrinsic scatter are strongly covariant between the filter scales, so that a cluster that is not detected in the optimal filter is very unlikely to be detected in a sub-optimal filter. This assumption may lead to a slight underestimate of the total detection probability. The calculation is repeated to obtain the detection efficiency as a function of mass and redshift.

At redshift z , the completeness at mass level M is the average fraction of all existing clusters with mass greater than M that we would expect to detect. The total number of clusters is obtained by integrating the Tinker et al. (2008) mass function at our fiducial cosmology; the average number of detected clusters is obtained by integrating the mass function scaled by the detection efficiency. Such computations are used to obtain the mass, as a function of redshift, at which the completeness level is 90%.

The completeness mass levels are shown in Figure 11. Note that we also show results obtained for the B12 scaling relation parameters. In this case we also obtained completeness estimates based in part on the filtered simulated maps. The central Compton parameters were measured in the filtered maps, and the S82 noise model was applied to generate a detection probability for each simulated cluster. Because of the small number of sufficiently high mass clusters in the model simulations, we have compensated for sample variance by reweighting the contribution of each cluster to correspond to the Tinker et al. (2008) mass function.

In summary, the S82 sample with $S/N > 4$, for which optical confirmation should be 100% complete for $z <$

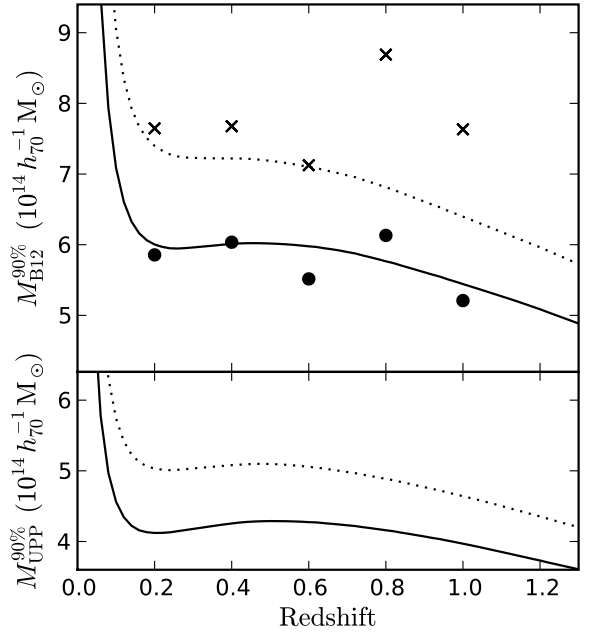


Figure 11. Estimate of the mass (M_{500c}) above which the ACT cluster sample within S82 is 90% complete (see Section 3.6). Lower panel assumes a UPP-based scaling relation with 20% intrinsic scatter; solid line is for $S/N > 4$ (full S82 sample, valid to $z < 0.8$), dotted line is for the $S/N > 5.1$ subsample (valid to $z \approx 1.4$). The upper panel shows analogous limits, but assuming scaling relation parameters obtained for the B12 model (Section 3.4). Circles (crosses) are based on filtering and analysis of B12 model clusters for the $S/N > 4$ (5.1) cut. The completeness threshold decreases steadily above $z \approx 0.6$ because clusters at this mass are easily resolved and the total SZ signal, at constant mass, increases with redshift.

0.8, is estimated to have SZ detection completeness of 90% above masses of $M_{500c} \approx 4.5 \times 10^{14} h_{70}^{-1} M_{\odot}$ for $z > 0.2$. The S82 sample having $S/N > 5.1$, for which optical confirmation is 100% complete for $z < 1.4$, is estimated to have SZ detection completeness of 90% above masses of $M_{500c} \approx 5.1 \times 10^{14} h_{70}^{-1} M_{\odot}$ for $z > 0.2$. (Note in the latter case, however, that the mass threshold falls steadily beyond redshift of 0.5.)

3.7. Redshift distribution

While a full cosmological analysis will be undertaken in Section 5, we briefly confirm the consistency of our cluster redshift distribution with expectations. As in the cosmological analysis, we will select our samples based on the signal to noise ratio of the uncorrected central decrement $\tilde{y}_0 \pm \delta\tilde{y}_0$ obtained for each cluster using the filter corresponding to $\theta_{500} = 5'.9$. We first consider the S82 clusters that have $\tilde{y}_0/\delta\tilde{y}_0 > 4$, over the redshift range $0.2 < z < 0.8$. Secondly we consider the “cosmological” sample of clusters, consisting of 15 clusters with $\tilde{y}_0/\delta\tilde{y}_0 > 5.1$ and $z > 0.2$. The cumulative number density as a function of redshift is shown in Figure 12. For each of the two subsamples, we bin the clusters into redshift bins of width 0.1 and perform a maximum likelihood fit (assuming Poisson statistics in each bin) to estimate σ_8 . To facilitate comparison with cosmological results presented in Section 5, we assume a flat Λ CDM cosmology with $\Omega_m = 0.25$ and $n_s = 0.96$, and fix the scaling relation parameters to the values associated with the UPP. Cluster count predictions are obtained starting

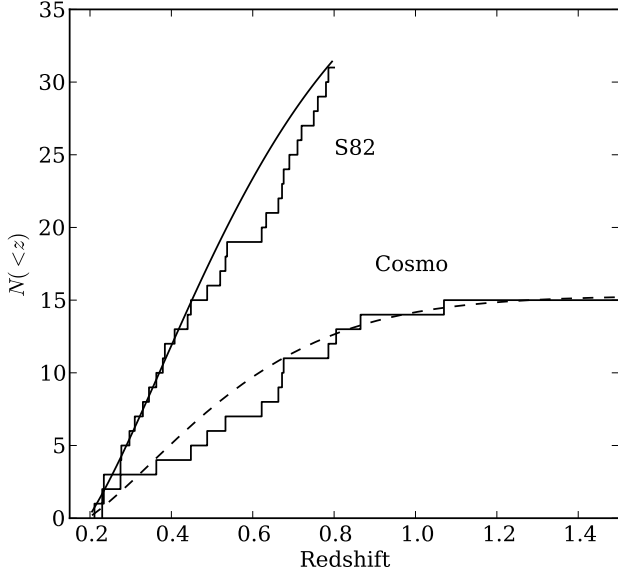


Figure 12. Cumulative number counts for two subsamples of the full cluster catalog for which confirmation is complete. The upper lines are data and model counts for the S82 sample of clusters having $\tilde{y}_0/\delta\tilde{y}_0 > 4$ and $0.2 < z < 0.8$. The lower lines represent the cosmological sample of 15 clusters with fixed-scale $\tilde{y}_0/\delta\tilde{y}_0 > 5.1$ and $z > 0.2$. The model for the counts is obtained from a maximum likelihood fit, with only σ_8 as a free parameter. The model includes a full treatment of selection effects for the sample under consideration.

from the cluster mass function of [Tinker et al. \(2008\)](#), and include all selection effects (intrinsic scatter, noise, and $\tilde{y}_0/\delta\tilde{y}_0$ cut). The fits yield $\sigma_8 = 0.782$ for the cosmological sample, and $\sigma_8 = 0.789$ for the S82 sample. Both of these are consistent with the result of the full cosmological analysis for the UPP scaling relation. The best-fit model is a good fit to the data in the sense that the likelihood score of the data, given the best-fit model, lies near the median of the likelihood scores for all samples drawn from the best-fit model that have the same total cluster count as the data. For the S82 (respectively, cosmological) sample, 55% (59%) of such random samples are less likely. Each of these samples is dominated by clusters with spectroscopic redshift estimates, and thus any features in the distribution cannot be attributed to redshift error.

4. COMPARISON WITH OTHER CATALOGS

In this section we compare the Equatorial cluster catalog and the SZ derived cluster properties to those obtained by other studies in microwave, X-ray, and optical wavelengths. While optical studies have good overlap with our sample in S82 to $z < 0.6$, previous X-ray and SZ survey data include only a small fraction of the clusters in our sample. We also examine the question of radio contamination of cluster decrements through a comparison of extrapolated fluxes near our cluster positions relative to random positions in the field.

4.1. Comparison to Planck Early SZ Sample

We compare our catalog and our derived cluster properties, to the catalog presented in the *Planck* all-sky Early Sunyaev-Zel’dovich cluster sample (ESZ; [Planck Collaboration 2011a](#)). The ESZ presents 189 clusters, of which 4 lie within the ACT Equatorial foot-

print, and of which 2 are detected by ACT. The two clusters detected by both *Planck* and ACT consist of two of the three clusters having ACT Y_{500} exceeding the 50% completeness level of the ESZ. (The third, not matched to the ESZ, is RCS2 J2327.4–0204.)

The two clusters not detected by ACT are low redshift clusters: Abell 2440 at $z = 0.091$ and Abell 119 at $z = 0.044$. Based on their integrated X-ray gas temperature measurements of 3.88 ± 0.14 and 5.62 ± 0.12 keV ([White 2000](#)), we estimate masses of $\approx 4 \times 10^{14}$ and $7 \times 10^{14} h_{70}^{-1} M_\odot$, respectively; these are well below our 90% completeness level (Section 3.6) at these redshifts.

For the two clusters detected by both *Planck* and ACT, a summary comparison of measured cluster properties may be found in Table 2. MACS J2135.2–0102 is detected by ACT, at low significance, inside S82. Abell 2355 (ACT-CL J2135.2+0125) is detected by ACT at high significance ($S/N = 9.3$) just outside the S82 region. The specifics of each case are discussed below.

For ease of comparison, we convert the *Planck* measurement of the SZ signal within $5R_{500}$ through the ESZ-provided conversion factor $Y_{500} = Y_{5R_{500}}/1.81$. We also use the ESZ value for θ_{500} (which is either determined from X-ray luminosity measurements, or from the SZ signal alone) to obtain an approximate value for M_{500c} . The ESZ analysis makes use of the “Standard” version of the Universal Pressure Profile, which assumes a self-similar scaling relation (see the Appendix of [Arnaud et al. 2010](#)). We thus re-analyze the ACT \tilde{y}_0 measurements using the profiles and scaling relation of the Standard UPP to estimate θ_{500} , Y_{500} , and M_{500c} . The results of this analysis differ only slightly from the results obtained using the full UPP (Table 8).

For MACS J2135.2–0102 ($z = 0.329$), X-ray luminosity data was not available and the ESZ presents the angular scale of the cluster based on SZ data alone. The scale, $\theta_{500} = 1.6 \pm 1.0'$ is the smallest θ_{500} in the ESZ, and corresponds to a very low mass ($\approx 1 \times 10^{14}$). Such a mass seems inconsistent with the SZ signal observed by either *Planck* or ACT. Lensed submillimeter galaxies have been observed near this cluster ([Iverson et al. 2010](#)), and the ESZ notes include a reference to possible point source contamination. The ACT measurement is likely to be less contaminated by such emission, since we use only 148 GHz data where dusty sources are comparatively dim. This may explain the large difference in Y_{500} inferred by the two telescopes. Overall this cluster is a peculiar case, and it is difficult to draw any useful conclusions from the disagreement of ACT and *Planck* measurements without more detailed X-ray information.

Abell 2355 (ACT-CL J2135.2+0125) is one of the most significant ACT detections, and one for which the ACT analysis implies a very high mass. A spectroscopic redshift of 0.1244 for this cluster has been obtained by [Kowalski et al. \(1983\)](#), and has subsequently been adopted in both the MCXC and the *Planck* ESZ. However, [Sarazin et al. \(1982\)](#) identify $z = 0.231$ as a more probable spectroscopic redshift, and this value is adopted by [Menanteau et al. \(2013\)](#), who find it to be much more consistent with their photometric estimate of $z = 0.25 \pm 0.01$. Furthermore, the NED⁴ entry for

⁴ NASA Extragalactic Database; <http://ned.ipac.caltech.edu/>. Retrieved July 15, 2012.

Table 2
Comparison of *Planck* and ACT cluster measurements

Cluster ID	Redshift	Planck			ACT		
		θ_{500} (arcmin)	Y_{500} (10^{-4} arcmin ²)	M_{500} ($10^{14} h_{70}^{-1} \text{ M}_{\odot}$)	θ_{500} (arcmin)	Y_{500} (10^{-4} arcmin ²)	M_{500} ($10^{14} h_{70}^{-1} \text{ M}_{\odot}$)
Early SZ clusters							
MACS J2135.2-0102	0.325	1.6 ± 1.0	9.8 ± 1.9	0.8 ± 0.8	3.1 ± 0.4	2.5 ± 1.2	2.7 ± 1.0
Abell 2355	0.231	5.1	15 ± 4	5.2	5.3 ± 0.2	14.3 ± 2.4	6.3 ± 1.3
Intermediate Results							
Abell 267	0.235	4.5 ± 0.2	9.3 ± 2.3	3.6 ± 0.5	5.4 ± 0.2	13.1 ± 2.4	5.6 ± 1.2
RXC J2129.6+0005	0.234	4.7 ± 0.2	7.8 ± 2.0	4.3 ± 0.5	5.2 ± 0.2	11.4 ± 2.5	5.2 ± 1.2
Abell 2631	0.275	5.4 ± 0.6	15.5 ± 2.3	9.8 ± 3.3	4.8 ± 0.2	11.5 ± 2.2	6.0 ± 1.3

Note. — Comparison of cluster properties as determined by *Planck* and by ACT, for two clusters from the ESZ (Planck Collaboration 2011a, Section 4.1) and three clusters from Intermediate Results (Planck Collaboration et al. 2013, Section 4.2). For *Planck*, θ_{500} is derived from X-ray measurements of M_{500} for all clusters except MACS J2135.2–0102, for which the angular scale was determined from the SZ data only. *Planck* values for Abell 2355 are corrected to redshift 0.231 as discussed in the text; M_{500} for this cluster is estimated from X-ray luminosity and thus carries a large ($\approx 50\%$) uncertainty. For the ACT measurements, the angular scale, mass and Y_{500} of each cluster are obtained simultaneously from the 148 GHz data assuming that the cluster pressure profile is described by the Standard UPP.

this cluster refers to an unpublished spectroscopic redshift $z = 0.228$ obtained from 3 galaxies. In order to compare the *Planck* and ACT measurements, we correct the *Planck* SZ measurements to $z = 0.231$.

The cluster angular scale used by *Planck* is obtained from X-ray luminosity based masses in the MCXC. We compute a new mass estimate using the MCXC scaling relations, correcting the X-ray luminosity for the changes in luminosity distance and K-correction (according to the $T = 5$ keV tabulation of Böhringer et al. 2004). The resulting inferred mass is more than double the estimate obtained for $z = 0.1244$. The corresponding θ_{500} is slightly smaller, and so we obtain a crude estimate of the Y_{500} that *Planck* might have measured if they had used this angular scale. From the inspection of Figure 9 of Planck Collaboration (2011a), the axis of degeneracy for the scale and signal measurements lies along $Y_{500} \propto \theta_{500}^{\alpha}$ with α in the range of 0.75 (for resolved clusters) to 1.5 (unresolved clusters). We compute the new value assuming $\alpha = 1$, and add 20% error to account for the uncertainty in α . This gives $Y_{500} = (15 \pm 4) \times 10^{-4}$ arcmin 2 . The ACT mass and Y_{500} are in good agreement with the X-ray mass and our estimate of the resulting *Planck* SZ signal.

Comparison to SZ measurements of three more clusters detected by *Planck* may be found in the next section.

4.2. Comparison to Weak Lensing Masses

In this section we examine weak lensing mass measurements of 4 clusters in the ACT Equatorial sample. While one is a high redshift cluster discovered by ACT, the other three are well-known moderate redshift clusters that have been observed by *XMM-Newton* and *Planck*.

Weak lensing measurements of ACT-CL J0022.2–0036 ($z = 0.81$) are presented in Miyatake et al. (2013). Subaru imaging is analyzed and radial profiles of tangential shear are fit with an NFW profile. They obtain a mass estimate of $M_{500c} = 8.4^{+3.3}_{-3.0} \times 10^{14} h_{70}^{-1} M_{\odot}$. While consistent with our SZ masses for any of the three model scaling relations, this mass is higher than the one deduced from the UPP scaling relation parameters and more consistent with the B12 and Nonthermal20 models. The SZ and lensing mass estimates are also consistent with the dynamical mass reported for ACT-CL J0022.2–0036 in

Menanteau et al. (2013).

The ACT Equatorial sample also includes 3 clusters (A267, A2361, and RXCJ2129.6+0005) treated by Planck Collaboration et al. (2013, hereafter PI3) in a comparison of weak lensing mass, X-ray mass proxies, and SZ signal. X-ray data are obtained from the *XMM-Newton* archive, and weak lensing masses for the clusters we consider here originate in Okabe et al. (2010). Each of these clusters is detected by ACT inside S82 with $S/N > 8$.

Comparing the ACT UPP based SZ masses to the weak lensing masses for these three clusters we obtain a mean weighted mass ratio of $M_{\text{ACT}}^{\text{UPP}}/M_{\text{WL}} = 1.3 \pm 0.2$. This is consistent with the mass ratio found by PI3 between X-ray masses and weak lensing masses for their full sample of 17 objects. For the B12 scaling relation parameters the ratio is $M_{\text{ACT}}^{\text{B12}}/M_{\text{WL}} = 1.8 \pm 0.3$.

PI3 also report Y_{500} , measured from *Planck*’s multi-band data using a matched filter, with the scale (θ_{500}) of the cluster template fixed using either the X-ray or the weak lensing mass. For each object we see agreement in the Y_{500} measurements at the 1 to 2 – σ level, and our mean ratio is consistent with unity. For θ_{500} determined from X-ray (weak lensing) mass we find weighted mean ratio $Y_{500,\text{ACT}}^{\text{UPP}}/Y_{500,\text{Planck}} = 0.90 \pm 0.16$ (0.98 ± 0.16).

The angular scales, Y_{500} and M_{500c} obtained by *Planck* and ACT are provided in Table 2. The ACT values are computed for the Standard version of the UPP, following our treatment of the ESZ clusters in section 4.1; these results are almost indistinguishable from those obtained with the full UPP treatment.

4.3. Comparison to SZA Measurements

Higher resolution SZ data can be obtained through interferometric observations. Reese et al. (2012) present Sunyaev-Zel’dovich Array (SZA) observations of two ACT Equatorial clusters at 30 GHz. For the high redshift, newly discovered cluster ACT-CL J0022-0036, a GNFW profile is fit to the 30 GHz SZ signal, and is used to infer the cluster mass assuming an NFW density profile and virialization of the gas. This yields a mass estimate of $M_{500c} = 7.3^{+1.0}_{-1.0} \times 10^{14} h_{70}^{-1} M_{\odot}$. For Abell 2631 (ACT-CL J2337.6+0016), X-ray and SZ data are

both used to constrain the density profile, producing a mass estimate of $M_{500c} = 9.4^{+4.8}_{-2.4} \times 10^{14} h_{70}^{-1} M_{\odot}$. These masses are somewhat higher than the ACT results for the UPP scaling relation, and are more consistent with the masses arising from the B12 scaling relation parameters.

4.4. Optical Cluster Catalogs

The extensive overlap of the ACT observations described in this work with the SDSS means that there are a number of existing optically selected cluster catalogs with which the ACT SZ selected cluster sample can be compared (see also Menanteau et al. 2013). For all the comparisons described below, we matched each catalog to the ACT cluster sample using a 0.5 Mpc matching radius, evaluated at the ACT cluster redshift.

Several optical cluster catalogs have been extracted from the SDSS legacy survey (e.g., Goto et al. 2002; Miller et al. 2005; Koester et al. 2007; Szabo et al. 2011; Wen et al. 2009, 2012). For the purposes of this comparison, we focus on the MaxBCG catalog (Koester et al. 2007) and its successor the GMBCG catalog (Hao et al. 2010). Both of these catalogs make use of the color-magnitude red-sequence characteristic of the cluster early type galaxy population, plus the presence of a Brightest Cluster Galaxy (BCG), to identify clusters. The MaxBCG catalog contains 13,823 clusters, of which 492 fall within the footprint of the 148 GHz map used in this work, and is thought to be $> 90\%$ complete and $> 90\%$ pure for clusters with $N_{\text{gal}} > 20$ over its entire redshift range ($0.1 < z < 0.3$). The GMBCG catalog builds on this work using the entire SDSS DR7 survey area, and is thought to have $> 95\%$ completeness and purity for clusters with richness > 20 galaxies and $z < 0.48$. A total of 1903 of the 55,424 GMBCG clusters fall within the ACT footprint.

We find that the ACT cluster catalog contains 8 clusters in common with MaxBCG, and 16 clusters in common with the GMBCG catalog. There are no ACT clusters at $z < 0.3$ in the SDSS DR7 footprint that are not cross matched with MaxBCG objects; however, there are 2 ACT clusters at $z < 0.48$ (ACT-CL J0348.6–0028 and ACT-CL J0230.9–0024) that are not cross matched with objects with richness > 20 in the GMBCG catalog within the common area⁵ between the two surveys. ACT-CL J0348.6–0028 ($z = 0.29$) is an optically rich system ($N_{\text{gal}} = 56.9 \pm 7.5$; as measured by Menanteau et al. 2013), while ACT-CL J0230.9–0024 is optically fairly poor ($N_{\text{gal}} = 19.9 \pm 4.5$). In both cases, Menanteau et al. (2013) find the BCG to have a small offset from the SZ position (0.1 Mpc for J0348.6 and 0.16 Mpc for J0230.9). However, neither of these objects has a plausible cross-match in the full GMBCG catalog, although we note that there is a GMBCG cluster (J057.14850–00.43348) at $z = 0.31$ located within a projected distance of 0.65 Mpc of ACT-CL J0348.6–0028.

We also compared the ACT catalog with that of Geach, Murphy, & Bower (2011). This catalog is constructed using the Overdense Red-sequence Cluster Algorithm (ORCA; Murphy, Geach, & Bower 2012) and is

the first optical cluster catalog available based on the deep ($r \approx 23.5$ mag) SDSS S82 region. It reaches to higher redshift ($z \approx 0.6$) than the catalogs based on the SDSS legacy survey data (such as GMBCG), and all of the MaxBCG clusters within a 7 deg^2 test area are re-detected (Murphy et al. 2012). We find that 26 $z < 0.6$ ACT clusters are cross-matched with objects in the Geach et al. catalog. However, there are 24 ACT clusters, which we have optically confirmed using the S82 data, that were not detected by Geach et al., and most of these (19 objects) are at $z > 0.6$. We also confirmed a further 4 objects at $z > 1$ in the S82 region with the addition of K_s -band imaging obtained at the Apache Point Observatory. This suggests that the ACT cluster catalog has a higher level of completeness for massive clusters at high redshift compared to current optical surveys.

4.5. X-ray Cluster Catalogs

Clusters are detected in X-rays through thermal bremsstrahlung emission from the intracluster gas, and so X-ray selected cluster surveys are complementary to SZ searches. However, current large area X-ray surveys are relatively shallow. The REFLEX cluster catalog (Böhringer et al. 2004) is derived from the ROSAT All Sky Survey data (Voges et al. 1999) and overlaps completely with the ACT survey. The full catalog contains a total of 448 clusters reaching to $z = 0.45$, from which 17 objects fall within the footprint of the ACT Equatorial maps. We find that only five of these clusters are cross-matched with ACT cluster detections. The detected objects are all luminous systems, with $L_X > 3.3 \times 10^{44} \text{ erg s}^{-1}$. The undetected objects are all lower luminosity (hence lower mass) and are at $z < 0.1$, where SZ completeness is low.

As discussed in Section 4.1, the *Planck* ESZ relies on the M_{500c} values presented in the MCXC (derived from the $L_X - M$ relation in Arnaud et al. (2010), which has intrinsic scatter $\approx 50\%$) to constrain the angular scale of detected clusters, and reduce the uncertainty in Y_{5R500} . The MCXC catalog includes 9 clusters from the ACT Equatorial cluster sample, and 6 clusters from the ACT Southern cluster sample.

Comparing the masses we derive from the UPP scaling relation to the MCXC masses, we obtain a mean ratio $M_{500c}^{\text{ACT,UPP}}/M_{500c}^{\text{MCXC}} = 1.03 \pm 0.19$. Adding in the Southern clusters (see Appendix) we find a ratio of 0.83 ± 0.13 .

While the Equatorial cluster result is consistent with the UPP scaling relation, the full sample prefers higher masses. For the B12 scaling relation parameters and the full sample we find $M_{500c}^{\text{ACT,B12}}/M_{500c}^{\text{MCXC}} = 1.12 \pm 0.17$. For the Equatorial sample alone, this ratio is 1.41 ± 0.27 . The mass ratios are shown in Figure 13.

4.6. Radio Point Sources

Relative to the field, galaxy clusters are observed to contain an excess of radio point sources (e.g., Cooray et al. 1998). Studies of potential SZ signal contamination by radio sources have been carried out at frequencies below 50 GHz (e.g., Lin et al. 2009). There are, however, few such studies at 150 GHz. Recently Sayers et al. (2013) used Bolocam at 140 GHz to study possible radio source contamination in 45 massive clusters. They found that the SZ signals from only 25% of

⁵ To determine the overlap between the ACT maps and various SDSS data releases, we make use of the angular selection function from <http://space.mit.edu/~molly/mangle/download/data.html> (see Swanson et al. 2008; Hamilton & Tegmark 2004; Blanton et al. 2005, for details).

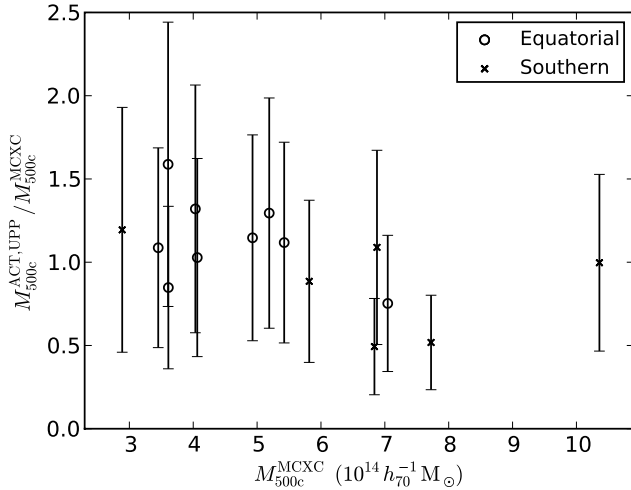


Figure 13. Ratio of ACT SZ determined masses to X-ray luminosity based masses from the MCXC. ACT masses assume the UPP scaling relation parameters. Error bars on mass include uncertainty from the ACT SZ measurements, and 50% uncertainty on MCXC masses. The weighted mean ratio is 1.03 ± 0.19 for the Equatorial clusters and 0.83 ± 0.13 for the full sample.

the sample were contaminated at a level greater than 1%. The largest contamination observed was 20% of the SZ signal. We study this phenomenon in the ACT cluster sample, using the FIRST catalog of flux densities at 1.4 GHz (White et al. 1997). The lower flux density limit of the catalog is at most 1 mJy, and overlaps with the ACT Equatorial field between R.A. of $21^{\text{h}}20^{\text{m}}$ and $3^{\text{h}}20^{\text{m}}$.

For each source in the FIRST catalog, we extrapolate the flux density to 148 GHz using flux-dependent spectral indices computed based on a stacking analysis in the ACT 148 GHz and 218 GHz maps. For the sources of interest here, the spectral index ranges from approximately -0.5 (at $S_{1.4} = 10$ mJy) to -0.8 (at $S_{1.4} = 100$ mJy). While a single spectral index is inadequate for describing the spectral behavior of radio sources over a decade in frequency, the extrapolation based on stacked ACT data is a reasonable technique for the purposes of predicting flux densities at ACT frequencies. Given the few sources found per cluster, the error in the extrapolation will be dominated by intrinsic scatter in 148 GHz flux densities (≤ 1 mJy) corresponding to a given $S_{1.4}$ range. This analysis does not take into account the probability of source orientation dependence that results in significantly greater observed flux density, as in the case of blazars. For each of the 63 galaxy clusters lying in the FIRST survey area, we take all sources within $2'$ of the cluster position and sum the predicted flux at 148 GHz. We find a mean flux density of $S_{148} = 0.94$ mJy, and the 9 most potentially contaminated clusters have flux density between 2.5 and 4.2 mJy. Converting these to a peak brightness in CMB temperature units using the 148 GHz beam, we obtain contamination of $11 \mu\text{K}$ on average and $50 \mu\text{K}$ at worst. These levels are substantially higher than would be expected if total radio flux were not correlated with cluster position. For random positions, the contamination is only $S_{148} = 0.2$ mJy on average, and 1% of locations have total flux exceeding 2.4 mJy.

For the purposes of inferring masses, we are interested in the impact the point sources may have in the measure-

ment of the uncorrected central decrement. To explore this, we create a simulated ACT map of the sources using their inferred flux densities at 148 GHz and the ACT beam shape. This map is then filtered with the same matched filter $\Psi_{5.9}$ described in Section 3.1. We obtain a prediction for the contamination level of each cluster by taking the maximum value in the filtered map within $2'$ of the cluster position. More than half of the clusters have predicted contamination less than $13 \mu\text{K}$ and 90% have less than $30 \mu\text{K}$ (which is smaller than the typical measurement uncertainty). The worst contamination prediction is associated with ACT-CL J0104.8+0002, at a level of $59 \mu\text{K}$ (corresponding to 35% of the signal strength, and larger than the cluster noise level of $41 \mu\text{K}$).

We emphasize that the contamination levels given here are extrapolations based on 1.4 GHz flux, and thus the contamination at 148 GHz for any particular source associated with a cluster may vary somewhat from the values stated. Since such contamination is difficult to model in detail without knowing the spectral indices of individual sources, and since the rate of significant contamination seems to be quite low, we make no attempt to correct for this effect. This may introduce a small, redshift dependent bias into scaling relation parameters obtained from these SZ data.

5. COSMOLOGICAL INTERPRETATION

Cluster count statistics, such as the number density of clusters above some limiting mass, are particularly sensitive to the total matter density (Ω_m) and the amplitude of density fluctuations (as parametrized by, e.g., σ_8). Because SZ selected cluster samples can reach to arbitrarily high redshift, they also probe parameters, such as the dark energy equation of state parameter w , that describe the recent expansion history.

In order to constrain cosmological parameters, we incorporate our sample into a Bayesian analysis and compute the posterior likelihood of cosmological parameters given the cluster data. We begin by outlining the formalism used to model the probability of our data given values of cosmological and scaling relation parameters. We then demonstrate the constraints achieved by combining the ACT cluster data with other data sets.

5.1. Likelihood Formalism

In this section we outline a formalism for determining the Bayesian likelihood of cosmological and scaling relation parameters given the ACT cluster measurements, including redshift, SZ, and dynamical mass information, when available. Our approach follows previous work in developing an expression for the probability of the cluster measurements based on the application of Poisson statistics to finely spaced bins in the multi-dimensional space of cluster observables. Such approaches naturally support non-trivial sample selection functions, the self-consistent calibration of scaling relations between object properties (i.e., between mass, SZ signal, and redshift), and missing data (i.e., the absence of independent mass measurements for some detected clusters). This approach to the comparison of a sample of detected objects to a number density predicted by a model is described by Cash (1979); Mantz et al. (2010b) present a useful general formalism for dealing with cluster data, applying it to X-ray mass and luminosity measurements

to obtain cosmological constraints while calibrating the mass–luminosity scaling relation. The SZ studies of [Sehgal et al. \(2011\)](#) and SPT (e.g., [Benson et al. 2013](#)) have applied similar techniques to SZ and X-ray data. Here, we develop an approach that pays particular attention to the uncertainties in the observed quantities, and in which the SZ signal is interpreted through the PBAA approach (Section 3.1).

We assume that the cluster data consist of a sample of confirmed clusters, and that for each cluster an uncorrected central Compton parameter $\tilde{y}_0 \pm \delta\tilde{y}_0$ and redshift $z \pm \delta z$ have been measured. The \tilde{y}_0 are obtained from maps filtered with $\Psi_{5.9}$. In some cases, clusters may also have dynamical mass measurements, M_{500c}^{dyn} (see Section 3.5). To parametrize these measurements in a way that is independent of cosmology, we define the observed dynamical mass parameter, $\tilde{m} \equiv E(z)M_{500c}^{\text{dyn}}/(10^{14} h_{70}^{-1} \text{M}_\odot)$.

To compare the observed sample to predicted cluster number densities, we consider all clusters to possess an intrinsic uncorrected central Compton parameter \tilde{y}_0^{tr} , redshift z^{tr} , and mass parameter \tilde{m}^{tr} . These true intrinsic quantities represent the values one would measure in the absence of any instrumental noise or astrophysical contamination (from, e.g., the CMB). For the SZ signal, \tilde{y}_0^{tr} should be thought of as the measurement we would make if we applied our filter $\Psi_{5.9}$ (i.e., the fixed-scale filter matched to the noise spectrum of our maps) to a map from which all noise and astrophysical contamination had been removed. The true cluster mass parameter, $\tilde{m}^{\text{tr}} \equiv M_{500c} h_{70} E(z^{\text{tr}})$ with $E(z^{\text{tr}})$ computed for the true cosmology, is representative of the halo mass rather than the mass inferred from an observational proxy (such as galaxy velocity dispersion).

We proceed by obtaining the number density of galaxy clusters in the space of true cluster properties \tilde{y}_0^{tr} , \tilde{m}^{tr} , and z^{tr} . As described in Section 3.2, we make use of the cluster mass function of [Tinker et al. \(2008\)](#) to predict, for cosmological parameters θ , the number of clusters per unit redshift and unit mass within the area of the survey:

$$n(\tilde{m}^{\text{tr}}, z^{\text{tr}}|\theta) = d^2 N(< \tilde{m}^{\text{tr}}, z^{\text{tr}})/dz^{\text{tr}} d\tilde{m}^{\text{tr}}. \quad (19)$$

Here we use the notation $n(\alpha|\beta)$, more commonly used with probability densities, to indicate the conditional distribution of clusters with respect to variables α when variables β are held fixed.

Given \tilde{m}^{tr} , z^{tr} , and scaling relation parameters $\psi = (A_m, B, C, \sigma_{\text{int}})$, the conditional distribution of Compton parameter values, $P(\tilde{y}_0^{\text{tr}}|\tilde{m}^{\text{tr}}, z^{\text{tr}}, \psi)$, is specified by equations (13) and (15). Summarizing these equations in our current notation, $\log \tilde{y}_0^{\text{tr}}$ is normally distributed,

$$\log \tilde{y}_0^{\text{tr}} \sim N(\log \tilde{y}_0(\tilde{m}^{\text{tr}}, z^{\text{tr}}, \psi); \sigma_{\text{int}}^2), \quad (20)$$

and the mean relation is described by

$$\begin{aligned} \tilde{y}_0^{\text{tr}}(\tilde{m}^{\text{tr}}, z^{\text{tr}}, \psi) &= 10^{A_0 + A_m} E^2(z^{\text{tr}}) (\tilde{m}^{\text{tr}})^{1+B_0+B} \times \\ &\quad Q \left[\left(\frac{1+z^{\text{tr}}}{1.5} \right)^C \theta_{500}/(\tilde{m}^{\text{tr}})^{C_0} \right] \times \\ &\quad f_{\text{rel}}(\tilde{m}^{\text{tr}}, z^{\text{tr}}). \end{aligned} \quad (21)$$

This may be used to compute the number density of clusters in the full space of true cluster properties:

$$n(\tilde{y}_0^{\text{tr}}, \tilde{m}^{\text{tr}}, z^{\text{tr}}|\theta, \psi) = P(\tilde{y}_0^{\text{tr}}|\tilde{m}^{\text{tr}}, z^{\text{tr}}, \psi) \times n(\tilde{m}^{\text{tr}}, z^{\text{tr}}|\theta). \quad (22)$$

In order to compare our observed sample to the model, it is necessary to properly account for the sample selection function, and for the effects of measurement uncertainty. This is especially important because our selection function depends explicitly on $\delta\tilde{y}_0$, and the mass function (and thus the cluster density as a function of \tilde{y}_0) is very steep. This full treatment of uncertainty allows us to include, in the same analysis, regions of the map that have quite different noise levels.

In general, we imagine that the cluster observables $\mathbf{x} = (\tilde{y}_0, \tilde{m}, z, \delta\tilde{y}_0, \delta\tilde{m}, \delta z)$ are related to the true cluster properties $\tilde{y}_0^{\text{tr}}, \tilde{m}^{\text{tr}}, z^{\text{tr}}$ by some probability distribution $P(\mathbf{x}|\tilde{y}_0^{\text{tr}}, \tilde{m}^{\text{tr}}, z^{\text{tr}}, \beta^{\text{dyn}})$. In addition to describing the scatter of each variable about its true value, and accounting for the dynamical mass bias through the parameter β^{dyn} (which is defined in Section 3.5), this distribution also includes a description of what measurement uncertainties we are likely to encounter for given values of the true cluster properties. For example, while most of our sample have spectroscopic redshifts for which the measurement uncertainty is negligible, some clusters (particularly at high redshift) have photometric redshift estimates with relatively large uncertainties ($\delta z \approx 0.06$). Although it may seem awkward to worry about measurement uncertainty for clusters that have not been detected, it is necessary, formally, to account for the distribution of errors if the sample is defined based on observed cluster properties. In our particular case, the full probability distribution factors to:

$$\begin{aligned} P(\mathbf{x}|\tilde{y}_0^{\text{tr}}, \tilde{m}^{\text{tr}}, z^{\text{tr}}, \beta^{\text{dyn}}) &= P(\tilde{y}_0|\tilde{y}_0^{\text{tr}}, \delta\tilde{y}_0) P(\delta\tilde{y}_0) \times \\ &\quad P(\tilde{m}|\tilde{m}^{\text{tr}}, \delta\tilde{m}, \beta^{\text{dyn}}) P(\delta\tilde{m}) \times \\ &\quad P(z|z^{\text{tr}}, \delta z) P(\delta z|z^{\text{tr}}). \end{aligned} \quad (23)$$

The expression above encodes the following properties of the ACT observations:

- For a given cluster, the measurements of \tilde{y}_0 , \tilde{m} , and z are independent; we do not expect any covariance in the errors. In practice we assume cluster observables are normally distributed about their true values (with the exception of \tilde{m} ; see next point).
- The probability distribution of \tilde{m} includes the effects of the dynamical mass bias parameter, β^{dyn} ; specifically the measured dynamical mass parameter \tilde{m} is expected to be normally distributed about mean $\beta^{\text{dyn}}\tilde{m}^{\text{tr}}$ with standard deviation $\delta\tilde{m}$.
- The distribution of \tilde{y}_0 errors, $P(\delta\tilde{y}_0)$, is independent of all true cluster properties. In practice $P(\delta\tilde{y}_0)$ is obtained from the histogram of the noise map.
- The distribution of \tilde{m} errors, $P(\delta\tilde{m})$, is independent of true cluster properties. In practice the uncertainty in the dynamical masses is related to the number of galaxies used for the velocity dispersion measurements. In any case, we do not need

to understand this distribution in detail, because observed mass is not a factor in sample selection.

- The distribution of z errors, $P(\delta z|z^{\text{tr}})$, may depend on the true cluster redshift. While spectroscopically measured redshifts are available for many sample clusters, high redshift clusters are more likely to have only photometric redshift estimates. In practice, this distribution only enters when computing the prediction for the *total* number of clusters observed within some volume. For suitably chosen sample redshift limits, the details will not matter (see discussion below).

For a sample selected based on signal to noise ratio threshold s and observed redshift range $[z_A, z_B]$, we define the selection function $S(\tilde{y}_0, z, \delta\tilde{y}_0)$ to take value unity when $\tilde{y}_0/\delta\tilde{y}_0 > s$ and $z \in [z_A, z_B]$, and to take value zero otherwise. Then the predicted number density in the 6-dimensional space of observables \mathbf{x} is

$$n(\mathbf{x}|\boldsymbol{\theta}, \boldsymbol{\psi}, \beta^{\text{dyn}}) = S(\tilde{y}_0, z, \delta\tilde{y}_0) \times \int d\tilde{y}_0^{\text{tr}} d\tilde{m}^{\text{tr}} dz^{\text{tr}} P(\mathbf{x}|\tilde{y}_0^{\text{tr}}, \tilde{m}^{\text{tr}}, z^{\text{tr}}, \beta^{\text{dyn}}) \times n(\tilde{y}_0^{\text{tr}}, \tilde{m}^{\text{tr}}, z^{\text{tr}}|\boldsymbol{\theta}, \boldsymbol{\psi}). \quad (24)$$

This cluster density function may be used to evaluate the extent to which the observed cluster data are consistent with the model $\boldsymbol{\theta}, \boldsymbol{\psi}, \beta^{\text{dyn}}$. This is achieved, as in [Cash \(1979\)](#) by imagining a very fine binning in the space of observables. We take bins indexed by α centered at \mathbf{x}_α and having (6-dimensional) volume V_α . In the limit of very fine bins, the total predicted counts in bin α is well-approximated by $N_\alpha(\boldsymbol{\theta}, \boldsymbol{\psi}, \beta^{\text{dyn}}) \approx V_\alpha n(\mathbf{x}_\alpha|\boldsymbol{\theta}, \boldsymbol{\psi}, \beta^{\text{dyn}})$. Furthermore, the number of observed clusters in bin α , denoted c_α , is either 0 or 1.

Letting D denote the set of bins in which a cluster has been observed (i.e., the α where $c_\alpha = 1$), we assume Poisson statistics in each bin, and obtain the probability of the data given the model parameters:

$$\begin{aligned} P(\{\mathbf{x}_i\}|\boldsymbol{\theta}, \boldsymbol{\psi}, \beta^{\text{dyn}}) &= P(\{c_\alpha\}|\boldsymbol{\theta}, \boldsymbol{\psi}, \beta^{\text{dyn}}) \\ &= \prod_{\alpha} e^{-N_\alpha(\boldsymbol{\theta}, \boldsymbol{\psi}, \beta^{\text{dyn}})} N_\alpha(\boldsymbol{\theta}, \boldsymbol{\psi}, \beta^{\text{dyn}})^{c_\alpha} \\ &= e^{-N_{\text{tot}}(\boldsymbol{\theta}, \boldsymbol{\psi}, \beta^{\text{dyn}})} \prod_{\alpha \in D} V_\alpha n(\mathbf{x}_\alpha). \end{aligned} \quad (25)$$

We have defined

$$\begin{aligned} N_{\text{tot}}(\boldsymbol{\theta}, \boldsymbol{\psi}, \beta^{\text{dyn}}) &= \sum_{\alpha} N_\alpha(\boldsymbol{\theta}, \boldsymbol{\psi}, \beta^{\text{dyn}}) \\ &= \int d^6x n(\mathbf{x}|\boldsymbol{\theta}, \boldsymbol{\psi}, \beta^{\text{dyn}}), \end{aligned} \quad (26)$$

the total number of clusters that the model predicts will be detected.

In equation (25), the product over occupied bins is only sensitive to the values of the density function at the locations of the detected clusters. The volume elements V_α depend on the data and the binning, but not on the cosmological or scaling relation parameters. They will thus cancel exactly in any ratio of probabilities comparing different models. So we may write the likelihood of

parameters $\boldsymbol{\theta}, \boldsymbol{\psi}, \beta^{\text{dyn}}$ given the cluster data $\{\mathbf{x}_i\}$ as

$$\begin{aligned} L(\boldsymbol{\theta}, \boldsymbol{\psi}, \beta^{\text{dyn}}|\{\mathbf{x}_i\}) &= P(\{\mathbf{x}_i\}|\boldsymbol{\theta}, \boldsymbol{\psi}, \beta^{\text{dyn}}) \\ &\propto e^{-N_{\text{tot}}(\boldsymbol{\theta}, \boldsymbol{\psi}, \beta^{\text{dyn}})} \times \prod_i n(\mathbf{x}_i|\boldsymbol{\theta}, \boldsymbol{\psi}, \beta^{\text{dyn}}), \end{aligned} \quad (27)$$

where i indexes the clusters in the sample.

When evaluating this expression in practice, we face the two related problems of computing the total cluster count prediction N_{tot} , and of computing the number density $n(\mathbf{x}_i|\boldsymbol{\theta}, \boldsymbol{\psi}, \beta^{\text{dyn}})$ for each cluster in the sample. Certain simplifications make possible the efficient computation of these quantities.

When computing $n(\mathbf{x}_i|\boldsymbol{\theta}, \boldsymbol{\psi}, \beta^{\text{dyn}})$, we approximate $P(\delta z|z^{\text{tr}})$ as being constant over the range of z^{tr} under consideration. This is acceptable because the integral over z^{tr} is restricted to the vicinity of the observed cluster redshift z_i by the distribution $P(z_i|z^{\text{tr}}, \delta z)$. We thus replace $P(\delta z|z^{\text{tr}})$ with $p_i \equiv P(\delta z|z^{\text{tr}})|_{z^{\text{tr}}=z_i}$. The p_i can then be factored out of the integral over true cluster properties in equation (24). When evaluating the likelihood in equation (27), these p_i contribute a constant multiplicative factor that is independent of parameters $\boldsymbol{\theta}, \boldsymbol{\psi}, \beta^{\text{dyn}}$. So their contribution is irrelevant, and like the V_α the p_i may be dropped from the likelihood expression.

When computing N_{tot} , the procedure is simplified by first integrating over \tilde{m}^{tr} to obtain the distribution $n(\tilde{y}_0^{\text{tr}}, z^{\text{tr}}|\boldsymbol{\theta}, \boldsymbol{\psi})$. The integrals over \tilde{m} and $\delta\tilde{m}$ are trivial to perform (independent of the form of $P(\delta m)$ and the value of β^{dyn}), because the selection function does not depend on \tilde{m} or $\delta\tilde{m}$. We may then write $N_{\text{tot}}(\boldsymbol{\theta}, \boldsymbol{\psi})$, dropping the dependence on β^{dyn} . The integral over $\delta\tilde{y}_0$ can be accomplished with $P(\delta\tilde{y}_0)$ based on the noise map. Note that this is essential to properly predict the total cluster count in cases where the map area under consideration includes a variety of local noise levels.

It is necessary to consider the impact of $P(\delta z|z^{\text{tr}})$ in the evaluation of N_{tot} . The number of clusters within an observed redshift range $z \in [z_A, z_B]$ will be approximately equal to the number of clusters with true redshift $z^{\text{tr}} \in [z_A, z_B]$. The difference between these two numbers may be interpreted as the result of clusters “scattering” over the redshift boundary due to measurement uncertainty. The magnitude of this effect is related to the noise level δz and the steepness of the distribution $n(z)$ at the boundaries.

Two properties of the ACT cluster sample allow us to avoid dealing with the details of $P(\delta z|z^{\text{tr}})$. The first is that we have spectroscopic redshift measurements for all but a small number of high redshift clusters. This means that $P(\delta z|z^{\text{tr}})$ strongly favors the case of $\delta z \approx 0$ at the low redshift sample boundary. Second, our upper redshift limit, which arises based on the depth of optical confirmation observations, is at $z = 1.4$. Clusters at $z = 1.4$ are sufficiently rare that uncertainty in δz does not greatly affect the total number of clusters within the full survey volume. For example, at $z = 1.4$ the predicted cluster number density has fallen off significantly and the effects of redshift uncertainty can only affect the total predicted counts by less than 1%. This is well below the error due to sample variance. So provided we use

a cluster sample for which SZ candidate follow-up (optical/IR confirmation) is complete out to at least $z = 1.4$, we may disregard redshift uncertainty when computing N_{tot} , and integrate over z^{tr} instead of z and δz .

For a more complicated data set (involving a large number of photometrically obtained redshifts), the distribution $P(\delta z|z^{\text{tr}})$ could be estimated based on the redshift error data in hand.

Finally, in the case that mass data are not available for some or all of the clusters, we can simply integrate over our ignorance of \tilde{m} . The model and scaling relation parameters give cluster density prediction, marginalized over the missing data, of

$$n(\tilde{y}_0, z, \delta \tilde{y}_0, \delta z | \boldsymbol{\theta}, \boldsymbol{\psi}) = \int d(\tilde{m}) \int dm n(\mathbf{x} | \boldsymbol{\theta}, \boldsymbol{\psi}, \beta^{\text{dyn}}). \quad (28)$$

The likelihood expression for the mixed case is

$$L(\boldsymbol{\theta}, \boldsymbol{\psi}, \beta^{\text{dyn}} | \{\mathbf{x}_i\}) \propto e^{-N_{\text{tot}}(\boldsymbol{\theta}, \boldsymbol{\psi})} \times \prod_{i \in M} n(\mathbf{x}_i | \boldsymbol{\theta}, \boldsymbol{\psi}, \beta^{\text{dyn}}) \times \prod_{i \notin M} n(\tilde{y}_{0i}, z_i, \delta \tilde{y}_{0i}, \delta z_i | \boldsymbol{\theta}, \boldsymbol{\psi}), \quad (29)$$

where M denotes the subset of clusters that have mass measurements.

5.2. Parameter Constraints for Fixed Scaling Relations

In this section we obtain cosmological parameter constraints by combining the Equatorial cluster sample with various external data sets, with the SZ scaling relation parameters fixed to values indicated by the UPP prescription, and by the B12 and Nonthermal20 models. For each case, we fix the scaling relation parameters ($A_m, B, C, \sigma_{\text{int}}$) to the values given in Table 1, and do not account for any uncertainty in these parameters. These results should thus be viewed as illustrating the potential constraint achievable from these cluster data, should the uncertainty on the scaling relations be reduced. The constraints also demonstrate the sensitivity of cosmological parameter estimates to the different physical assumptions entering each model.

The posterior distributions of cosmological parameters are obtained through Markov Chain Monte Carlo (MCMC) sampling, driven by the CosmoMC software (Lewis & Bridle 2002), with matter power spectra and CMB angular power spectra computed using the CAMB software (Lewis et al. 2000). The ACT Equatorial data contribute to the likelihood according to equation (29). The cluster sample includes the 15 objects (identified in Table 7) that lie inside sample boundaries defined by redshift range $0.2 < z < 1.4$ and signal to noise ratio cut $\tilde{y}_0/\delta \tilde{y}_0 > 5.1$. As discussed in Section 2.4, the cut on $\tilde{y}_0/\delta \tilde{y}_0$ corresponds to the level above which the optical confirmation campaign has successfully confirmed or falsified all SZ detections.

Posterior distributions of parameters for data sets that do not include ACT cluster information are obtained from chains released with the WMAP seven-year results (WMAP7; Komatsu et al. 2011). In some cases, chains also incorporate data from Baryon Acoustic Oscillation experiments (BAO; Percival et al. 2010), and

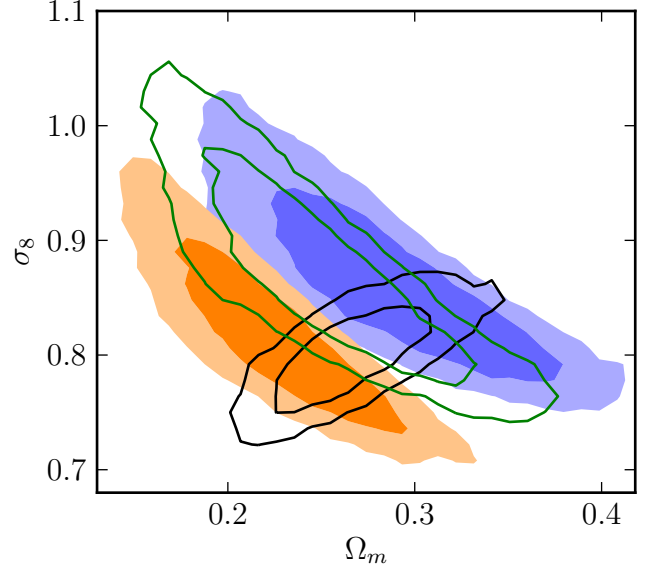


Figure 14. Constraints on Λ CDM cosmological parameters from WMAP7 (black line contours) and ACTcl+BBN+H0 (without CMB information). Contours indicate 68 and 95% confidence regions. ACT results are shown for three scaling relations: UPP (orange contours), B12 (green lines), Nonthermal20 (violet contours). While any one scaling relation provides an interesting complement to CMB information, the results from the three different scaling relations span the range of parameter values allowed by WMAP measurements.

Type Ia supernovae (SNe; Hicken et al. 2009). When not constrained by CMB information, ACT cluster data are combined with results from big bang nucleosynthesis (BBN; Hamann et al. 2008) to constrain the baryon fraction and with Hubble constant measurements (denoted H_0 ; Riess et al. 2009). The H_0 measurements are also used to restrict the parameter space of w CDM model studies, emphasizing the role clusters can play in such cases.

We first consider a Λ CDM model with 7 free parameters representing the baryon and cold dark matter densities (Ω_b and Ω_c), the angular scale of the sound horizon (θ_A), the normalization (A_s) and spectral index (n_s) of the matter power spectrum, the optical depth of reionization (τ), and the SZ spectral amplitude (A_{SZ}). For simplicity, the SZ spectral amplitude is not explicitly tied to the cluster scaling relation parameters.

The potential for our cluster data to constrain Ω_m and σ_8 is demonstrated in Figure 14. In order to emphasize the impact of cluster studies, we have computed the parameter likelihood for the ACT cluster data in combination with BBN and H_0 only (these constrain the baryon density to $\Omega_b h^2 = 0.022 \pm 0.002$ and the Hubble constant to $H_0 = 73.9 \pm 3.6 \text{ km s Mpc}^{-1}$). We plot the marginalized two-dimensional distribution of parameters σ_8 and Ω_m , with contours showing the 68% and 95% confidence regions. The ACT cluster constraints, without CMB information, are seen to nicely complement the results from WMAP7. But the variation in the constraints between models shows the degree to which uncertainty in the cluster physics diminishes the constraining power. The marginalized parameter values are provided in Table 3.

In a w CDM model (which differs from the Λ CDM model in that the equation of state param-

Table 3
Cosmological parameter constraints for the Λ CDM model.

Data set	$\Omega_c h^2$	Ω_m	Parameter (Λ CDM)		
			σ_8	h	$\sigma_8(\Omega_m/0.27)^{0.3}$
Without ACT Cluster Data					
WMAP7	0.111 ± 0.006	0.266 ± 0.029	0.801 ± 0.030	0.710 ± 0.025	0.797 ± 0.053
WMAP7 + BAO + H0	0.112 ± 0.003	0.272 ± 0.016	0.809 ± 0.024	0.704 ± 0.014	0.811 ± 0.034
Fixed Scaling Relations (§5.2)					
BBN + H0 + ACTcl(B12)	0.115 ± 0.024	0.252 ± 0.047	0.872 ± 0.065	0.741 ± 0.036	0.848 ± 0.032
WMAP7 + ACTcl(UPP)	0.107 ± 0.002	0.250 ± 0.012	0.786 ± 0.013	0.720 ± 0.015	0.768 ± 0.015
WMAP7 + ACTcl(B12)	0.114 ± 0.002	0.285 ± 0.014	0.824 ± 0.014	0.693 ± 0.015	0.837 ± 0.017
WMAP7 + ACTcl(Non)	0.117 ± 0.002	0.303 ± 0.016	0.839 ± 0.014	0.680 ± 0.015	0.869 ± 0.018
Dynamical Mass Constraints (§5.3)					
BBN + H0 + ACTcl(dyn)	0.141 ± 0.042	0.301 ± 0.082	0.975 ± 0.108	0.737 ± 0.037	0.999 ± 0.130
WMAP7 + ACTcl(dyn)	0.115 ± 0.004	0.292 ± 0.025	0.829 ± 0.024	0.688 ± 0.021	0.848 ± 0.042
WMAP7 + ACTcl(dyn) + BAO + H0	0.114 ± 0.003	0.282 ± 0.016	0.829 ± 0.022	0.696 ± 0.013	0.840 ± 0.031

Note. — Numbers indicate the mean and standard deviation of the marginalized posterior distribution. ACTcl results for scaling relations based on the Universal Pressure Profile (UPP), and the B12 and *Nonthermal20* (Non) models do not include marginalization over scaling relation uncertainties (Section 5.2). ACTcl(dyn) results use Southern and Equatorial cluster data, including dynamical mass measurements for the Southern clusters (Section 5.3).

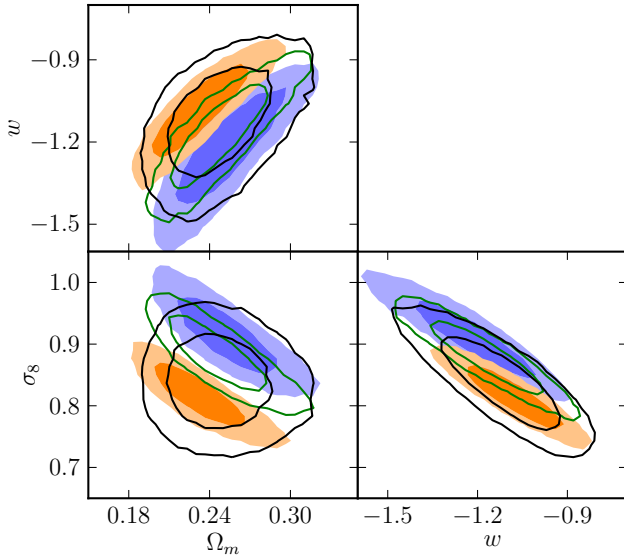


Figure 15. Constraints on w CDM cosmological parameters from WMAP7+H0 (solid black lines), and WMAP7+ACTcl+H0 for three scaling relations (B12 scaling relation is green lines; UPP is orange contours; Nonthermal20 is violet contours.)

eter w may deviate from -1), cluster counts are sensitive to the effect of dark energy on the expansion rate of the recent universe. As shown in Table 4, the ACT cluster data provides slightly improved constraints on σ_8 relative to WMAP7 alone; but the true power of the cluster data is to break degeneracies between σ_8 , Ω_m , and w . We present composite parameters defined by $\sigma_8(\Omega_m/0.27)^{0.4}$ and $w(\Omega_m/0.27)$ to express these improvements.

In Figure 15, we show 2-d marginalized constraints for Ω_m , σ_8 , and w . Note that, for this plot only, we have included the H0 prior, to partially break the degeneracy between these three parameters and to emphasize the role that normalization of the SZ scaling relation plays in this space.

Overall, we find no disagreement between WMAP7 and the ACT cluster data for any of the three model-based scaling relations considered. While the three scaling relations produce results that almost completely span the

range of Ω_m and σ_8 preferred by WMAP7, a better understanding of scaling relation parameters can provide significant improvements in parameter constraints given even a relatively small cluster sample. This is addressed in the next section.

5.3. Parameter Constraints from Dynamical Mass Data

As an alternative to fixing the SZ scaling relation parameters based on models, in this section we perform a cosmological analysis using the ACT Southern and Equatorial cluster samples, including the dynamical mass information for the Southern clusters from Sifón et al. (2012). The two samples are included as separate contributions to the likelihood. In this analysis, the dynamical masses directly inform the cosmology, while the selection function is understood in terms of the observed SZ signal, through the modeling of the cluster signal with the UPP. In this framework the scaling relation parameters will be naturally constrained to be consistent with the observed sample sizes and with the \tilde{y}_0 measurements of the clusters that also have dynamical mass measurements.

For the Equatorial clusters we apply the same sample selection criteria used in Section 5.2, and thus include the same 15 clusters. As before, these clusters contribute to the likelihood through their observed redshifts and \tilde{y}_0 measurements.

For the Southern cluster sample, we obtain \tilde{y}_0 measurements from the three-season 148 GHz maps as described in the Appendix. For the cosmological analysis we restrict the Southern sample based on a signal to noise ratio threshold of $\tilde{y}_0/\delta\tilde{y}_0 > 5.7$ and an observed redshift requirement of $0.315 < z < 1.4$. The $\tilde{y}_0/\delta\tilde{y}_0$ threshold is high enough to exclude new, unconfirmed candidates in our analysis of the three-season Southern maps. The lower redshift bound restricts the sample to the clusters for which Sifón et al. (2012) have measured dynamical masses. This yields a sample of seven clusters, which are identified in Table 9. Of the nine clusters used in Sehgal et al. (2011), our sample includes the five clusters at $z > 0.315$. The sample includes the exceptional cluster ACT-CL J0102–4915; the inclusion or exclusion of this cluster does not change the cosmological parameter constraints significantly. The contribution from the Southern clusters to the likelihood is in the form of equa-

Table 4
Cosmological parameter constraints for the flat w CDM model.

Data set	$\Omega_c h^2$	Parameter (w CDM)		
		σ_8	$\sigma_8(\Omega_m/0.27)^{0.4}$	$w(\Omega_m/0.27)$
Without ACT Cluster Data				
WMAP7	0.111 ± 0.006	0.832 ± 0.134	0.790 ± 0.065	-0.95 ± 0.13
WMAP7 + SNe	0.111 ± 0.006	0.791 ± 0.042	0.798 ± 0.060	-0.99 ± 0.11
Fixed Scaling Relations (§5.2)				
WMAP7 + ACTcl(UPP)	0.108 ± 0.002	0.854 ± 0.106	0.766 ± 0.018	-0.90 ± 0.06
WMAP7 + ACTcl(B12)	0.115 ± 0.003	0.915 ± 0.111	0.849 ± 0.021	-1.04 ± 0.07
WMAP7 + ACTcl(Non)	0.119 ± 0.003	0.915 ± 0.116	0.887 ± 0.023	-1.11 ± 0.08
Dynamical Mass Constraints (§5.3)				
WMAP7 + ACTcl(dyn)	0.116 ± 0.005	0.921 ± 0.108	0.851 ± 0.052	-1.05 ± 0.11
WMAP7 + ACTcl(dyn) + SNe	0.115 ± 0.004	0.835 ± 0.034	0.858 ± 0.049	-1.08 ± 0.10

Note. — Cluster data provide important constraints in the space of σ_8 , Ω_m and w . ACTcl results are presented for scaling relations based on the Universal Pressure Profile (UPP), and the B12 and *Nonthermal20* (Non) models; these do not include marginalization over scaling relation uncertainties. Results constrained using dynamical mass data (dyn) include a full marginalization over SZ scaling relation parameters.

Table 5
Cosmological parameter constraints for the flat w CDM model, for various combinations of WMAP7, ACT cluster data (with scaling relation constrained using dynamical mass data), and Type Ia Supernovae results.

Data set	$\Omega_c h^2$	Ω_m	Parameter (w CDM)		
			σ_8	h	w
Without ACT Cluster Data					
WMAP7	0.111 ± 0.006	0.259 ± 0.096	0.832 ± 0.134	0.753 ± 0.131	-1.117 ± 0.394
WMAP7 + SNe	0.111 ± 0.006	0.276 ± 0.020	0.791 ± 0.042	0.697 ± 0.016	-0.969 ± 0.054
Dynamical Mass Constraints					
WMAP7 + ACTcl(dyn)	0.116 ± 0.005	0.237 ± 0.080	0.921 ± 0.108	0.792 ± 0.119	-1.306 ± 0.356
WMAP7 + ACTcl(dyn) + SNe	0.115 ± 0.004	0.289 ± 0.017	0.835 ± 0.034	0.691 ± 0.014	-1.011 ± 0.052

tion (27).

The data set consisting of this combination of Equatorial SZ data and Southern SZ and dynamical mass data is denoted ACTcl(dyn). These data are combined with other data sets in an MCMC approach to parameter estimation as described in Section 5.2, except that now we allow the SZ scaling relation parameters to vary, assuming flat priors over ranges $1.7 < A_m < 0.9$, $-1 < B < 3$, $-2 < C < 2$ and $0 < \sigma_{\text{int}}^2 < 2$. These priors are not intended to be informative, but rather to permit the scaling relation parameters to range freely over values supported by the data. For the dynamical mass bias parameter, we apply a Gaussian prior corresponding to $1/\beta^{\text{dyn}} = 1.00 \pm 0.15$,⁶ motivated by the results of Evrard et al. (2008) as described in Section 3.5.

5.3.1. Λ CDM Constraints

The effect of the increased freedom in the scaling relation parameters may be seen in Figure 16, which shows the confidence regions on σ_8 and Ω_m , in a Λ CDM model, from ACT cluster data combined with BBN and H0. The scaling relation parameters are not well constrained without some prior information, so for this chain only we include a Gaussian prior on the redshift evolution corresponding to $C = 0.0 \pm 0.5$, based on the B12 model fits. Compared to results for fixed scaling relation parameters, the distribution of acceptable σ_8 and Ω_m is broader and skewed, at fixed Ω_m , towards high σ_8 .

⁶ This description of the prior is an artifact of our initial implementation of the likelihood, where the parameter describing the bias corresponded to $1/\beta^{\text{dyn}}$.

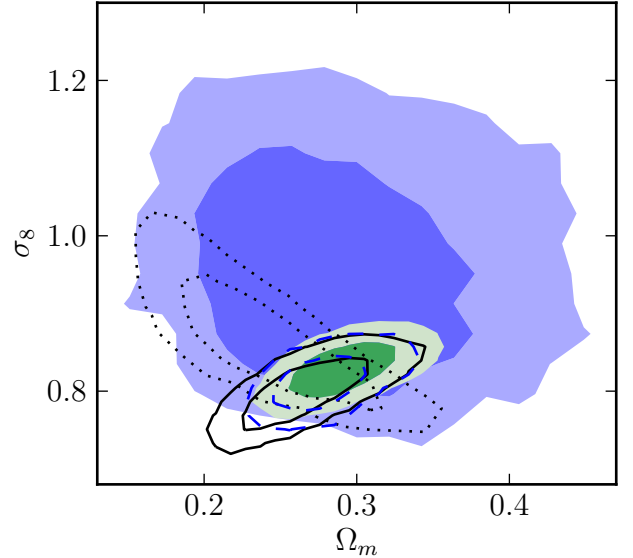


Figure 16. Constraints on Λ CDM cosmological parameters from Equatorial and Southern clusters. Results from ACTcl(dyn)+BBN+H0 (violet contours), and WMAP7+ACTcl(dyn) (green contours), which both include full marginalization over scaling relation and dynamical mass bias parameters, may be compared to WMAP alone (solid black lines). Dotted line shows constraints for ACTcl+BBN+H0, using the same cluster sample but with the scaling relation fixed to the central values obtained from the dynamical mass fit of Section 3.5; note the similarity to contours in Figure 14 obtained for Equatorial SZ data with B12 fixed scaling relation parameters. Dashed blue line shows WMAP7+ACTcl(dyn), with full marginalization over scaling relation parameters but with β^{dyn} fixed to 1.33.

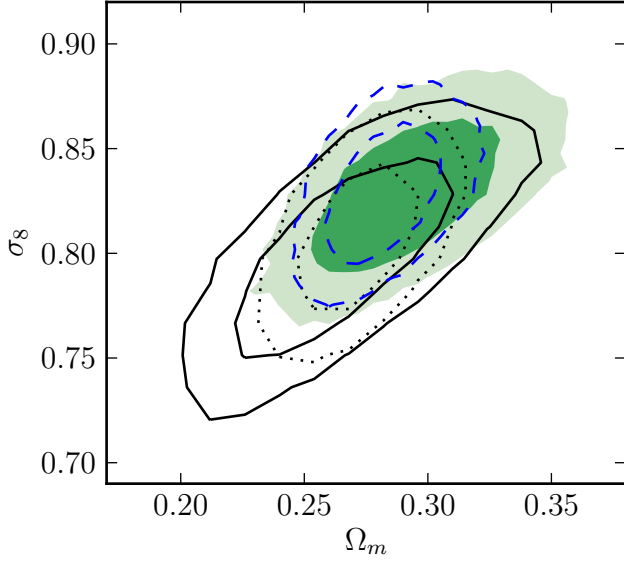


Figure 17. Constraints on Λ CDM cosmological parameters from the combined Southern and Equatorial cluster samples, including dynamical mass measurements for the Southern clusters and full marginalization over scaling relation parameters. WMAP7 and WMAP7+ACTcl(dyn) are identified as in Figure 16 (solid black line and green contours, respectively). Also shown are WMAP7+BAO+H0 (dotted black line) and WMAP7+ACTcl(dyn)+BAO+H0 (dashed blue lines).

In a Λ CDM model, the addition of ACTcl(dyn) data improves the constraints on σ_8 , Ω_m , and h relative to WMAP7 alone by factors of 0.8 to 0.9, as can be seen in Figure 16. WMAP7+ACTcl(dyn) prefers slightly larger values of σ_8 than does WMAP7+BAO+H0. For the composite parameter $\sigma_8(\Omega_m/0.27)^{0.3}$, the combination of WMAP7+BAO+H0+ACTcl(dyn) improves the uncertainty by a factor of 0.6 compared to WMAP7. Parameter values are presented in Table 3 and confidence regions for σ_8 and Ω_m are plotted in Figure 17.

Within the WMAP7+ACTcl(dyn) chain for Λ CDM the dynamical mass bias parameter is pushed to $\beta^{\text{dyn}} = 1.12 \pm 0.17$ (corresponding to $1/\beta^{\text{dyn}} = 0.91 \pm 0.12$), a substantial change given the prior on β^{dyn} . To explore the consequences of a large systematic bias in the dynamical mass measurements, we study a Λ CDM chain run with fixed $\beta^{\text{dyn}} = 1.33$. We find that σ_8 and Ω_m move towards the central values preferred by WMAP7, with parameter uncertainty slightly reduced. The confidence contours associated with this chain can be seen in Figure 16.

In the chains presented we have not included any intrinsic scatter in the relationship between dynamical mass and halo mass, because the measurement errors on the masses are already at the 20-50% level, and because we do not use dynamical mass in the sample selection criteria. However, large levels of intrinsic scatter in \tilde{m}^{dyn} , or correlations between \tilde{m}^{dyn} and \tilde{y}_0^{tr} as mass proxies will affect the derived constraints to some degree. In chains that include a 30% scatter in the dynamical mass relative to halo mass, the central values of σ_8 , Ω_m , and $\sigma_8(\Omega_m/0.3)^{0.27}$ decrease by up to 20% of their quoted uncertainties. Adding positive correlation to the scatter in \tilde{m}^{dyn} and \tilde{y}_0^{tr} lowers the preferred parameter values further. Running WMAP7+ACTcl(dyn)

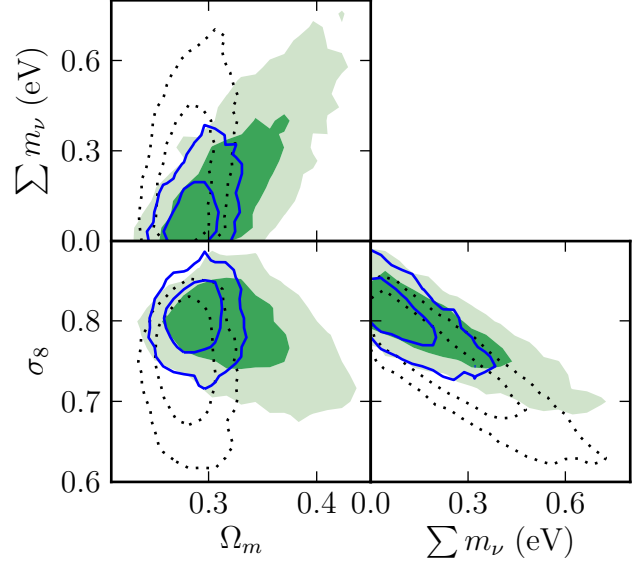


Figure 18. Constraints within an extension to Λ CDM that allows for non-zero neutrino density. The data sets shown are WMAP7+BAO+H0 (dotted black lines), WMAP7+ACTcl(dyn) (green contours), and WMAP7+ACTcl(dyn)+BAO+H0 (solid blue lines). The total number of relativistic species is fixed to $N_{\text{eff}} = 3.046$.

with an additional constraint that the two proxies scatter with correlation coefficient $\rho = 0.5$, we obtain constraints $\sigma_8 = 0.820 \pm 0.025$, $\Omega_m = 0.284 \pm 0.025$, and $\sigma_8(\Omega_m/0.3)^{0.27} = 0.832 \pm 0.042$. The addition of these two effects changes the central parameter constraints by roughly 40% of the quoted uncertainty; limits on the intrinsic scatter and its correlation between proxies will be important in higher precision studies.

5.3.2. Neutrino Mass Constraints

As an extension to Λ CDM, we also run chains where the cosmic mass density of neutrinos is allowed to vary. Constraints are interpreted in terms of the sum of the neutrino mass species according to the relation $\Omega_\nu h^2 = \sum_\nu m_\nu / (93 \text{ eV})$. Combining the ACT cluster data with WMAP7 and BAO+H0 leads to significant improvements in this constraint, as shown in Figure 18 and Table 6. For WMAP7+BAO+H0+ACTcl(dyn) we obtain an upper limit, at 95% confidence, of $\sum m_\nu < 0.29 \text{ eV}$. The improvement in this constraint is driven by the preference of the ACT cluster data for values of σ_8 and Ω_m that are in the upper range of those consistent with WMAP. Interpretations of this preference are discussed below.

5.3.3. w CDM Constraints

Within a w CDM model, we consider the ACTcl(dyn) data in combination with WMAP7 and with SNe (which provides important, complementary constraints on the recent cosmic expansion history). The WMAP7+ACTcl(dyn) are consistent with WMAP7+SNe, but with a preference (as was found in Λ CDM) for slightly higher values of σ_8 and Ω_m . The importance of cluster information is demonstrated by the improvement, over both WMAP7 and WMAP7+SNe, in the composite parameter $\sigma_8(\Omega_m/0.27)^{0.4}$ (see Table 4). As a result, the main impact of adding the cluster data to either WMAP7 or WMAP7+SNe is to reduce the

Table 6
Cosmological parameter constraints for Λ CDM, extended with one additional parameter for non-zero neutrino density.

Data set	Ω_m	Parameter (Λ CDM + $\sum_h m_\nu$)			$\sum m_\nu$ (eV) 95% CL
WMAP7 + BAO + H0	0.282 ± 0.018	0.742 ± 0.053	0.693 ± 0.016		< 0.58
WMAP7 + ACTcl(dyn)	0.325 ± 0.041	0.787 ± 0.041	0.663 ± 0.029		< 0.57
WMAP7 + ACTcl(dyn) + BAO + H0	0.289 ± 0.018	0.802 ± 0.031	0.690 ± 0.015		< 0.29

Note. — The cluster data greatly assist in breaking the degeneracy between σ_8 , Ω_m , and the neutrino density (as parametrized by $\sum m_\nu$). ACTcl(dyn) results use South and Equatorial cluster data, including dynamical mass measurements for the Southern clusters (Section 5.3).

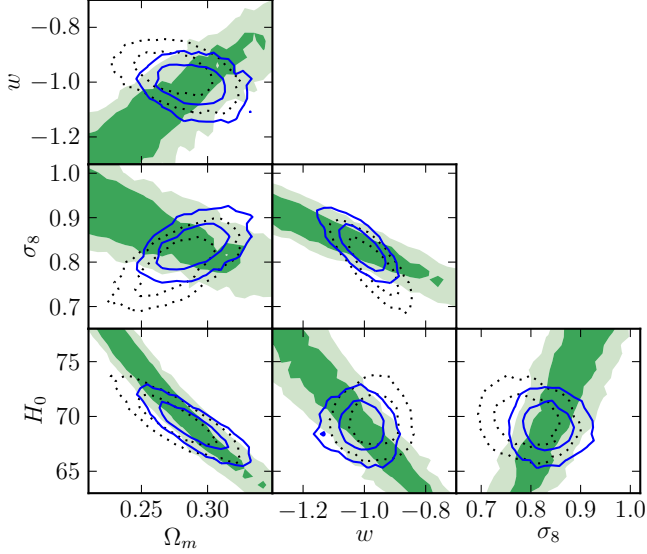


Figure 19. Constraints on w CDM cosmological parameters from the combined Southern and Equatorial cluster samples, with scaling relation parameters constrained based on dynamical mass measurements. Data sets shown are WMAP7+SNe (dotted black lines), WMAP7+ACTcl(dyn) (green contours), and WMAP7+ACTcl(dyn)+SNe (solid blue lines). The units of H_0 are $\text{km s}^{-1} \text{Mpc}^{-1}$.

uncertainties in σ_8 and Ω_m by factors of ≈ 0.8 . The w CDM parameter constraints for each combination of ACTcl(dyn) and SNe with WMAP7 are presented in Table 5, with marginalized 2-d confidence regions shown in Figure 19.

The slight preference of ACTcl(dyn) for higher values of σ_8 and Ω_m than are preferred by WMAP7+SNe alone also induces a shift in the posterior distribution for w . The value of the composite parameter $w(\Omega_m/0.27)$ decreases by almost one standard deviation when ACTcl(dyn) are added to WMAP7 + SNe.

5.3.4. Scaling Relation Constraints

The marginalized constraints on the SZ scaling relation parameters derived for the ACTcl(dyn) chains are presented in Table 1. The parameters indicating deviations from self-similar scaling with mass and redshift (B and C) are each consistent with 0, and consistent with the fits to all models. The intrinsic scatter, σ_{int} is somewhat higher than the 20% seen in the model results, but it is not well-constrained by these data. Furthermore, since the data span a fairly restricted range of masses, there is significant covariance between A_m , B , and σ_{int} .

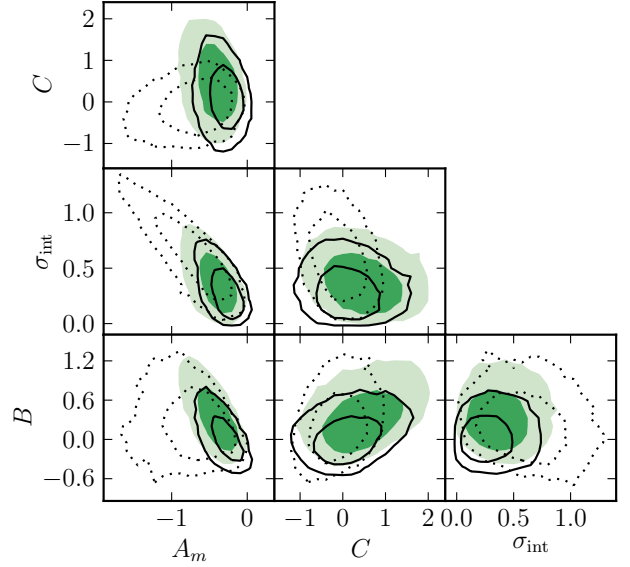


Figure 20. Constraints on SZ scaling relation parameters from the combined Southern and Equatorial cluster samples, ACTcl(dyn), constrained based on dynamical mass measurements in a cosmological MCMC. Green contours are for WMAP7+ACTcl(dyn) chain; black solid lines are for WMAP7+ACTcl(dyn) but with J0102–4915 excluded from the Southern sample. Dotted line shows constraints for ACTcl(dyn)+BBN+H0 (i.e., without CMB information), but with a Gaussian prior on C of 0.0 ± 0.5 .

The value of A is provided for $M_{\text{pivot}} = 7 \times 10^{14} h_{70}^{-1} \text{M}_\odot$, chosen to produce negligible covariance between A and B . While the cosmological results change only slightly when J0102–4915 is excluded from the Southern cluster sample, we note that scaling relation parameters are somewhat more affected, and in particular that the slope parameter B drops from 0.36 ± 0.36 to 0.06 ± 0.27 and the scatter σ_{int} drops from 0.42 ± 0.19 to 0.33 ± 0.17 . The 2-d confidence regions for scaling relation parameters are shown in Figure 20.

5.3.5. Discussion

We note that the constraints on cosmological parameters are due mostly to the inclusion of the dynamical mass measurements for the Southern clusters, rather than due to the SZ data of the larger Equatorial sample. However, while the removal of the Equatorial sample from the likelihood computation produces no change in the cosmological parameter constraints, it leads to a significant weakening in the SZ scaling relation parameter constraints. This is because the Equatorial sam-

ple constrains the scaling relation parameters to values that predict sample selection functions consistent with the Equatorial sample size. By including the Equatorial SZ measurements in the likelihood, we obtain simultaneous, self-consistent constraints on cosmological parameters and the SZ scaling relation parameters. Despite the low weight of the SZ information in the cosmological parameter constraints, it remains true that the sample is SZ selected and thus approximately mass-limited over a broad range of redshifts.

Immediate improvement in the cosmological constraining power can be obtained through improved calibration of the SZ mass relation. This is underway in the form of a campaign to collect dynamical mass data for the Equatorial sample (Sifón et al, in prep.). The current analysis would also benefit from an improved understanding of any systematic biases in the measurement of halo mass using galaxy velocity dispersions. In addition to the dynamical mass data, we are pursuing weak lensing (e.g., Miyatake et al. 2013), X-ray (e.g., Menanteau et al. 2012), and additional SZ (e.g., Reese et al. 2012) measurements to improve constraints on the SZ–mass scaling relation from the ACT cluster sample. All such mass measurements can be easily included in our formulation. The sample of clusters appropriate for our approach to the cosmological analysis will grow as targeted follow-up on the Equatorial field candidates is completed to lower S/N ratios.

While this work presents a new way to quantify the SZ–mass relation for $10^{15} M_{\odot}$ clusters, we note that it is but one component of a growing web of observation that tie optical and SZ data together. Recently the Planck team presented results (Planck Collaboration 2012b) on the SZ emission from SDSS galaxies that extended the SZ–mass relation down to $10^{13} M_{\odot}$ systems and showed that the gas properties of dark matter haloes are similar to those in massive clusters.

6. CONCLUSION

The ACT Equatorial maps at 148 GHz, along with an optical and infrared confirmation campaign, have yielded a sample of 68 confirmed, SZ selected galaxy clusters in the redshift range from approximately 0.1 to 1.4, in an area of 504 square degrees. Inside the 270 square degree overlap with SDSS Stripe 82, and assuming the scaling relation parameters associated with the Universal Pressure Profile of A10, the sample is estimated to be 90% complete above a mass of $M_{500c} \approx 4.5 \times 10^{14} h_{70}^{-1} M_{\odot}$. (The completeness level is dependent on the normalization of the SZ–mass scaling relation; a similar estimate using the most likely scaling relation parameters from a full cosmological MCMC that incorporates dynamical mass information gives a 90% completeness mass of $\approx 9 \times 10^{14} h_{70}^{-1} M_{\odot}$.)

In order to use the SZ signal to determine cluster mass and to constrain cosmological parameters, we have developed a framework that predicts the cluster amplitude in a matched-filtered map based on cluster mass and redshift. The approach naturally handles varying noise levels in a map, and can be adapted easily to accommodate alternative cluster pressure profiles and scaling relations.

The framework is based on the Universal Pressure Profile of A10, but we obtain alternative normalizations through an analysis of several cluster physics models.

While the normalization obtained directly from the UPP is consistent with X-ray masses from the MCXC, the calibration to the B12 model is more consistent with dynamical mass measurements of the ACT Southern cluster sample. From this we conclude that it is necessary to consider a broad range of scaling relation parameters when using the cluster data to constrain cosmological parameters.

We have presented constraints in Λ CDM and w CDM models using the ACT Equatorial cluster sample for several fixed normalizations of the SZ scaling relations. In each case the cosmological constraints are consistent with WMAP. The results obtained for fixed scaling relations demonstrate the potential for such a cluster sample to provide important new cosmological information, even for modest cluster samples, provided the systematics of the SZ–mass calibration can be better understood.

We have also demonstrated cosmological constraints based on the combination of SZ measurements and dynamical mass data, in which the four parameters of the SZ scaling relation are calibrated simultaneously with cosmological parameters. The results provide significant constraints that are complementary to CMB, BAO, and Type Ia Supernovae data. The scaling relation parameters obtained in this analysis are consistent with the B12 model and inconsistent with the normalization arising directly from the UPP.

Our results are consistent with a study of the SZ signal from the ACT Southern cluster sample (Sehgal et al. 2011), as well as the σ_8 constraints from the skewness analysis of the ACT Equatorial 148 GHz maps. (Wilson et al. 2012).

While the ACT SZ cluster data prefer matter density parameters that are at the upper end of those supported by WMAP7 data, our results are consistent with cluster studies that incorporate a variety of other mass proxies. They are also in agreement with the recent ACT angular power spectrum results (Sievers et al, in prep.), which also favor the upper limits of σ_8 and Ω_m permitted by WMAP7.

The combined X-ray, f_{gas} , Supernovae, BAO, and CMB results of Mantz et al. (2010b) produce $\sigma_8 = 0.80 \pm 0.02$ (0.79 ± 0.03) and $\Omega_m = 0.257 \pm 0.015$ (0.272 ± 0.016) in Λ CDM (w CDM); these results are marginally consistent with but lower than the results of our analysis. For the ACTcl(dyn)+H0+BBN run in Λ CDM, we compute $\sigma_8(\Omega_m/0.25)^{0.47} = 0.87 \pm 0.04$, which is higher than, but consistent with, the value of 0.813 ± 0.027 obtained for the X-ray cluster study of Vikhlinin et al. (2009b).

Using SPT cluster SZ and X-ray mass information, Reichardt et al. (2013) obtain σ_8 and Ω_m measurements in a combined WMAP7, high- ℓ power spectrum, and clusters analysis that lie slightly below the central values preferred by CMB measurements alone (including Sievers et al, in prep.). From their Figure 5 we also estimate that their cluster data in combination with H0 and BBN (i.e., without CMB information) produce a composite parameter constraint of $\sigma_8(\Omega_m/0.27)^{0.3} = 0.77 \pm 0.05$, lower by roughly 1.3- σ than either our WMAP7+ACTcl(dyn) or BBN+H0+ACTcl(dyn) results. Our results are in general agreement with SPT despite several differences in the SZ signal interpretation and mass calibration, which we summarize here.

SPT makes use of cluster signal simulations, analogous to the B12 models used here, in order to interpret an observable based on signal to noise ratio. In contrast, our analysis relies instead on the assumption of a simple relation between mass and the cluster pressure profile. We test the PBAA approach on simulated maps based on models of cluster physics, but we do not use these models to place priors on the scaling relation parameters. The SPT mass calibration is ultimately derived from measurements of Y_X , defined as the product of the core-excised X-ray temperature and the cluster gas mass (Kravtsov et al. 2006). The use of Y_X as a mass proxy has, in turn, been calibrated to weak lensing masses (Vikhlinin et al. 2009a). The slight preference of our data for higher values of σ_8 and Ω_m (for both the ACTcl(dyn) and ACTcl(B12) studies) compared to SPT may indicate a complicated relationship between the various mass proxies.

This work was supported by the U.S. National Science Foundation through awards AST-0408698 and AST-0965625 for the ACT project, as well as awards PHY-0855887 and PHY-1214379. Funding was also provided by Princeton University, the University of Pennsylvania, and a Canada Foundation for Innovation (CFI) award to UBC. ACT operates in the Parque Astronómico Atacama in northern Chile under the auspices of the Comisión Nacional de Investigación Científica y Tecnológica de Chile (CONICYT). Computations were performed on the GPC supercomputer at the SciNet HPC Consortium. SciNet is funded by the CFI under the auspices of Compute Canada, the Government of Ontario, the Ontario Research Fund – Research Excellence; and the University of Toronto.

REFERENCES

- Abazajian, K. N., et al. 2009, *ApJS*, 182, 543
 Abell, G. O. 1958, *ApJS*, 3, 211
 Abell, G. O., Corwin, Jr., H. G., & Olowin, R. P. 1989, *ApJS*, 70, 1
 Akritas, M. G., & Bershady, M. A. 1996, *ApJ*, 470, 706
 Allen, S. W., Evrard, A. E., & Mantz, A. B. 2011, *ARA&A*, 49, 409
 Annis, J., et al. 2011, *ApJ* submitted (arXiv:1111.6619)
 Arnaud, M., Pointecouteau, E., & Pratt, G. W. 2005, *A&A*, 441, 893
 Arnaud, M., Pratt, G. W., Piffaretti, R., Böhringer, H., Croston, J. H., & Pointecouteau, E. 2010, *A&A*, 517, A92 (A10)
 Bahcall, N. A., & Cen, R. 1992, *ApJ*, 398, L81
 Battaglia, N., Bond, J. R., Pfrommer, C., & Sievers, J. L. 2012, *ApJ*, 758, 74
 Benson, B. A., et al. 2013, *ApJ*, 763, 147
 Birkinshaw, M. 1999, *Phys. Rep.*, 310, 97
 Blanton, M. R., et al. 2005, *AJ*, 129, 2562
 Bode, P., & Ostriker, J. P. 2003, *ApJS*, 145, 1
 Bode, P., Ostriker, J. P., Cen, R., & Trac, H. 2012, *ApJ* submitted (arXiv:1204.1762) (B12)
 Bode, P., Ostriker, J. P., & Vikhlinin, A. 2009, *ApJ*, 700, 989
 Böhringer, H., et al. 2000, *ApJS*, 129, 435
 —. 2004, *A&A*, 425, 367
 Bonamente, M., Joy, M., LaRoque, S. J., Carlstrom, J. E., Nagai, D., & Marrone, D. P. 2008, *ApJ*, 675, 106
 Brodwin, M., et al. 2010, *ApJ*, 721, 90
 Burenin, R. A., Vikhlinin, A., Hornstrup, A., Ebeling, H., Quintana, H., & Mescheryakov, A. 2007, *ApJS*, 172, 561
 Carlstrom, J. E., Holder, G. P., & Reese, E. D. 2002, *ARA&A*, 40, 643
 Cash, W. 1979, *ApJ*, 228, 939
 Cooray, A. R., Grego, L., Holzappel, W. L., Joy, M., & Carlstrom, J. E. 1998, *AJ*, 115, 1388
 Coppin, K., Halpern, M., Scott, D., Borys, C., & Chapman, S. 2005, *MNRAS*, 357, 1022
 Das, S., et al. 2013, *JCAP* submitted (arXiv:1301.1037)
 Duffy, A. R., Schaye, J., Kay, S. T., & Dalla Vecchia, C. 2008, *MNRAS*, 390, L64
 Dunkley, J., et al. 2011, *ApJ*, 739, 52
 Dünner, R., Hasselfield, M., Marriage, T. A., Sievers, J., et al. 2013, *ApJ*, 762, 10
 Ebeling, H., Edge, A. C., Böhringer, H., Allen, S. W., Crawford, C. S., Fabian, A. C., Voges, W., & Huchra, J. P. 1998, *MNRAS*, 301, 881
 Evrard, A. E., et al. 2008, *ApJ*, 672, 122
 Foley, R. J., et al. 2011, *ApJ*, 731, 86
 Geach, J. E., Murphy, D. N. A., & Bower, R. G. 2011, *MNRAS*, 413, 3059
 Goto, T., et al. 2002, *AJ*, 123, 1807
 Gralla, M. B., et al. 2011, *ApJ*, 737, 74
 Hajian, A., et al. 2011, *ApJ*, 740, 86
 Hamann, J., Lesgourgues, J., & Mangano, G. 2008, *JCAP*, 3, 4
 Hamilton, A. J. S., & Tegmark, M. 2004, *MNRAS*, 349, 115
 Hand, N., et al. 2011, *ApJ*, 736, 39
 —. 2012, *Physical Review Letters*, 109, 041101
 Hao, J., et al. 2010, *ApJS*, 191, 254
 Harrison, I., & Coles, P. 2012, *MNRAS*, 421, L19
 Henry, J. P., Gioia, I. M., Maccacaro, T., Morris, S. L., Stocke, J. T., & Wolter, A. 1992, *ApJ*, 386, 408
 Hicken, M., Wood-Vasey, W. M., Blondin, S., Challis, P., Jha, S., Kelly, P. L., Rest, A., & Kirshner, R. P. 2009, *ApJ*, 700, 1097
 Hincks, A. D., et al. 2010, *ApJS*, 191, 423
 Hinshaw, G., et al. 2012, *ApJS* submitted (arXiv:1212.5226)
 Hotchkiss, S. 2011, *JCAP*, 7, 4
 Hoyle, B., Jimenez, R., & Verde, L. 2011, *Phys. Rev. D*, 83, 103502
 Itoh, N., Kohyama, Y., & Nozawa, S. 1998, *ApJ*, 502, 7
 Ivison, R. J., et al. 2010, *A&A*, 518, L35
 Jarosik, N., et al. 2011, *ApJS*, 192, 14
 Keisler, R., et al. 2011, *ApJ*, 743, 28
 Kelly, B. C. 2007, *ApJ*, 665, 1489
 Koester, B. P., et al. 2007, *ApJ*, 660, 239
 Komatsu, E., et al. 2011, *ApJS*, 192, 18
 Kowalski, M. P., Ulmer, M. P., & Cruddace, R. G. 1983, *ApJ*, 268, 540
 Kravtsov, A. V., Vikhlinin, A., & Nagai, D. 2006, *ApJ*, 650, 128
 Lampeitl, H., et al. 2010, *MNRAS*, 401, 2331
 Lau, E. T., Kravtsov, A. V., & Nagai, D. 2009, *ApJ*, 705, 1129
 Lewis, A., & Bridle, S. 2002, *Phys. Rev.*, D66, 103511
 Lewis, A., Challinor, A., & Lasenby, A. 2000, *Astrophys. J.*, 538, 473
 Lin, Y., Partridge, B., Poher, J. C., Boucheffry, K. E., Burke, S., Klein, J. N., Coish, J. W., & Haffenberger, K. M. 2009, *ApJ*, 694, 992
 Lopes, P. A. A., de Carvalho, R. R., Gal, R. R., Djorgovski, S. G., Odewahn, S. C., Mahabal, A. A., & Brunner, R. J. 2004, *AJ*, 128, 1017
 Lumsden, S. L., Nichol, R. C., Collins, C. A., & Guzzo, L. 1992, *MNRAS*, 258, 1
 Mahdavi, A., Hoekstra, H., Babul, A., Bildfell, C., Jeltama, T., & Henry, J. P. 2013, *ApJ*, 767, 116
 Mantz, A., Allen, S. W., Ebeling, H., Rapetti, D., & Drlica-Wagner, A. 2010a, *MNRAS*, 406, 1773
 Mantz, A., Allen, S. W., Rapetti, D., & Ebeling, H. 2010b, *MNRAS*, 406, 1759
 Marriage, T. A., et al. 2011, *ApJ*, 737, 61
 Marrone, D. P., et al. 2012, *ApJ*, 754, 119
 Mehrrens, N., et al. 2012, *MNRAS*, 423, 1024
 Menanteau, F., et al. 2010, *ApJ*, 723, 1523
 —. 2012, *ApJ*, 748, 7
 —. 2013, *ApJ*, 765, 67
 Miller, C. J., et al. 2005, 130, 968
 Miyatake, H., et al. 2013, *MNRAS*, 429, 3627
 Miyazaki, S., Hamana, T., Ellis, R. S., Kashikawa, N., Massey, R. J., Taylor, J., & Refregier, A. 2007, *ApJ*, 669, 714
 Mortonson, M. J., Hu, W., & Huterer, D. 2011, *Phys. Rev. D*, 83, 023015
 Motl, P. M., Hallman, E. J., Burns, J. O., & Norman, M. L. 2005, *ApJ*, 623, L63

- Murphy, D. N. A., Geach, J. E., & Bower, R. G. 2012, *MNRAS*, 420, 1861
- Nagai, D., Kravtsov, A. V., & Vikhlinin, A. 2007, *ApJ*, 668, 1
- Navarro, J. F., Frenk, C. S., & White, S. D. M. 1995, *MNRAS*, 275, 720
- Okabe, N., Takada, M., Umetsu, K., Futamase, T., & Smith, G. P. 2010, *PASJ*, 62, 811
- Percival, W. J., et al. 2010, *MNRAS*, 401, 2148
- Planck Collaboration. 2011a, *A&A*, 536, A8
- . 2011b, *A&A*, 536, A26
- . 2012a, *A&A* submitted (arXiv:1207.4061)
- . 2012b, *A&A* submitted (arXiv:1212.4131)
- Planck Collaboration et al. 2013, *A&A*, 550, A129 (PI3)
- Reese, E. D., et al. 2012, *ApJ*, 751, 12
- Reichardt, C. L., et al. 2012, *ApJ*, 755, 70
- . 2013, *ApJ*, 763, 127
- Reid, B. A., & Spergel, D. N. 2006, *ApJ*, 651, 643
- Riess, A. G., et al. 2009, *ApJ*, 699, 539
- Rozo, E., et al. 2010, *ApJ*, 708, 645
- Sarazin, C. L., Rood, H. J., & Struble, M. F. 1982, *A&A*, 108, L7
- Sayers, J., et al. 2013, *ApJ*, 764, 152
- Sehgal, N., et al. 2010, *ApJ*, 709, 920
- Sehgal, N., et al. 2011, *ApJ*, 732, 44
- . 2013, *ApJ*, 767, 38
- Shaw, L. D., Nagai, D., Bhattacharya, S., & Lau, E. T. 2010, *ApJ*, 725, 1452
- Sifón, C., et al. 2012, *ApJ* submitted (arXiv:1201.0991) (S12)
- Stalder, B., et al. 2012, *ApJ* submitted (arXiv:1205.6478)
- Staniszewski, Z., et al. 2009, *ApJ*, 701, 32
- Story, K., et al. 2011, *ApJ*, 735, L36
- Story, K. T., et al. 2012, *ApJ* submitted (arXiv:1210.7231)
- Sunyaev, R. A., & Zel'dovich, Y. B. 1970, *Comments on Astrophysics and Space Physics*, 2, 66
- Suzuki, N., et al. 2012, *ApJ*, 746, 85
- Swanson, M. E. C., Tegmark, M., Hamilton, A. J. S., & Hill, J. C. 2008, *MNRAS*, 387, 1391
- Swetz, D. S., et al. 2011, *ApJS*, 194, 41
- Szabo, T., Pierpaoli, E., Dong, F., Pipino, A., & Gunn, J. 2011, *ApJ*, 736, 21
- Tinker, J., Kravtsov, A. V., Klypin, A., Abazajian, K., Warren, M., Yepes, G., Gottlöber, S., & Holz, D. E. 2008, *ApJ*, 688, 709
- Trac, H., Bode, P., & Ostriker, J. P. 2011, *ApJ*, 727, 94
- Tucker, W. H., Tananbaum, H., & Remillard, R. A. 1995, *ApJ*, 444, 532
- Vanderlinde, K., et al. 2010, *ApJ*, 722, 1180
- Vikhlinin, A., et al. 2009a, *ApJ*, 692, 1033
- . 2009b, *ApJ*, 692, 1060
- Voges, W., et al. 1999, *A&A*, 349, 389
- Wen, Z. L., Han, J. L., & Liu, F. S. 2009, *ApJS*, 183, 197
- . 2012, *ApJS*, 199, 34
- Werner, N., Churazov, E., Finoguenov, A., Markevitch, M., Burenin, R., Kaastra, J. S., & Böhringer, H. 2007, *A&A*, 474, 707
- White, D. A. 2000, *MNRAS*, 312, 663
- White, R. L., Becker, R. H., Helfand, D. J., & Gregg, M. D. 1997, *ApJ*, 475, 479
- Williamson, R., et al. 2011, *ApJ*, 738, 139
- Wilson, M. J., et al. 2012, *Phys. Rev. D* in press (arXiv:1203.6633)
- Wittman, D., Dell'Antonio, I. P., Hughes, J. P., Margoniner, V. E., Tyson, J. A., Cohen, J. G., & Norman, D. 2006, *ApJ*, 643, 128
- Zhang, Y.-Y., et al. 2010, *ApJ*, 711, 1033

Table 7
Confirmed galaxy clusters in the ACT Equatorial region.

ACT ID	R.A. ($^{\circ}$)	Dec. ($^{\circ}$)	Redshift	Reg.	S/N	θ_{500} (arcmin)	\tilde{y}_0 (10^{-4})	Alternate ID (ref.)
ACT-CL J0008.1+0201	2.0418	2.0204	0.36 ± 0.04	DR8	4.7	4.71	0.96 ± 0.21	WHL J000810.4+020112 (1)
ACT-CL J0012.0-0046	3.0152	-0.7693	1.36 ± 0.06	S82	5.3	16.47	0.91 ± 0.18	
ACT-CL J0014.9-0057	3.7276	-0.9502	0.533	S82*	7.8	3.53	1.34 ± 0.18	GMB11 J003.71362-00.94838 (2)
ACT-CL J0017.6-0051	4.4138	-0.8580	0.211	S82	4.2	4.71	0.73 ± 0.17	SDSS CE J004.414726-00.876164 (3)
ACT-CL J0018.2-0022	4.5623	-0.3795	0.75 ± 0.04	S82	4.4	4.71	0.74 ± 0.17	
ACT-CL J0022.2-0036	5.5553	-0.6050	0.805	S82*	9.8	1.18	1.35 ± 0.16	WHL J002213.0-003634 (1)
ACT-CL J0026.2+0120	6.5699	1.3367	0.65 ± 0.04	DR8	6.3	4.71	0.99 ± 0.16	
ACT-CL J0044.4+0113	11.1076	1.2221	1.11 ± 0.03	S82	5.5	1.18	0.70 ± 0.15	
ACT-CL J0045.2-0152	11.3051	-1.8827	0.545	DR8	7.5	3.53	1.31 ± 0.18	WHL J004512.5-015232 (1)
ACT-CL J0051.1+0055	12.7875	0.9323	0.69 ± 0.03	S82	4.2	1.18	0.53 ± 0.15	WHL J005112.9+005555 (1)
ACT-CL J0058.0+0030	14.5189	0.5106	0.76 ± 0.02	S82	5.0	2.35	0.72 ± 0.15	
ACT-CL J0059.1-0049	14.7855	-0.8326	0.786	S82*	8.4	2.35	1.24 ± 0.15	
ACT-CL J0104.8+0002	16.2195	0.0495	0.277	S82	4.3	12.94	0.62 ± 0.15	SDSS CE J016.232412+00.058164 (3)
ACT-CL J0119.9+0055	19.9971	0.9193	0.72 ± 0.03	S82	5.0	3.53	0.73 ± 0.15	
ACT-CL J0127.2+0020	21.8227	0.3468	0.379	S82	5.1	2.35	0.72 ± 0.15	SDSS CE J021.826914+00.344883 (3)
ACT-CL J0139.3-0128	24.8407	-1.4769	0.70 ± 0.03	DR8	4.3	1.18	0.54 ± 0.17	
ACT-CL J0152.7+0100	28.1764	1.0059	0.230	S82*	9.0	3.53	1.30 ± 0.15	Abell 267 (4)
ACT-CL J0156.4-0123	29.1008	-1.3879	0.45 ± 0.04	DR8	5.2	2.35	0.67 ± 0.15	WHL J015624.3-012317 (1)
ACT-CL J0206.2-0114	31.5567	-1.2428	0.676	S82*	6.9	2.35	0.94 ± 0.14	
ACT-CL J0215.4+0030	33.8699	0.5091	0.865	S82*	5.5	1.18	0.75 ± 0.15	
ACT-CL J0218.2-0041	34.5626	-0.6883	0.672	S82*	5.8	2.35	0.82 ± 0.15	GMB11 J034.56995-00.69963 (2)
ACT-CL J0219.8+0022	34.9533	0.3755	0.537	S82	4.7	2.35	0.66 ± 0.15	GMB11 J034.94761+00.35956 (2)
ACT-CL J0219.9+0129	34.9759	1.4973	0.35 ± 0.02	DR8	4.9	2.35	0.62 ± 0.14	NSCS J021954+013102 (5)
ACT-CL J0221.5-0012	35.3925	-0.2063	0.589	S82	4.0	1.18	0.33 ± 0.15	GMB11 J035.40587-00.21967 (2)
ACT-CL J0223.1-0056	35.7939	-0.9466	0.663	S82*	5.8	2.35	0.84 ± 0.15	GMB11 J035.79247-00.95712 (2)
ACT-CL J0228.5+0030	37.1250	0.5033	0.72 ± 0.02	S82	4.0	1.18	0.56 ± 0.15	GMB11 J037.11459+00.52965 (2)
ACT-CL J0230.9-0024	37.7273	-0.4043	0.44 ± 0.03	S82	4.2	8.24	0.63 ± 0.15	WHL J023055.3-002549 (6)
ACT-CL J0239.8-0134	39.9718	-1.5758	0.375	DR8	8.8	4.71	1.61 ± 0.18	Abell 370 (4)
ACT-CL J0240.0+0116	40.0102	1.2693	0.62 ± 0.03	DR8	4.8	4.71	0.70 ± 0.15	WHL J024001.7+011606 (1)
ACT-CL J0241.2-0018	40.3129	-0.3109	0.684	S82	5.1	1.18	0.59 ± 0.15	WHL J024115.5-001841 (1)
ACT-CL J0245.8-0042	41.4645	-0.7013	0.179	S82	4.1	10.59	0.61 ± 0.15	Abell 381 (4)
ACT-CL J0250.1+0008	42.5370	0.1403	0.78 ± 0.03	S82	4.5	2.35	0.62 ± 0.15	
ACT-CL J0256.5+0006	44.1354	0.1049	0.363	S82*	5.4	7.06	0.82 ± 0.15	SDSS CE J044.143375+00.105766 (3)
ACT-CL J0301.1-0110	45.2925	-1.1716	0.53 ± 0.04	S82	4.2	2.35	0.51 ± 0.15	GMB11 J045.30649-01.17805 (2)
ACT-CL J0301.6+0155	45.4158	1.9219	0.167	DR8	5.8	4.71	1.12 ± 0.20	RXC J0301.6+0155 (7)
ACT-CL J0303.3+0155	45.8343	1.9214	0.153	DR8	5.2	7.06	1.00 ± 0.20	Abell 409 (4)
ACT-CL J0308.1+0103	47.0481	1.0607	0.633	S82	4.8	1.18	0.60 ± 0.15	GMB11 J047.03754+01.04350 (2)
ACT-CL J0320.4+0032	50.1239	0.5399	0.384	S82	4.9	3.53	0.72 ± 0.15	SDSS CE J050.120594+00.533045 (3)
ACT-CL J0326.8-0043	51.7075	-0.7312	0.448	S82*	9.1	1.18	1.24 ± 0.15	GMBCG J051.70814-00.73104 (8)
ACT-CL J0336.9-0110	54.2438	-1.1705	1.32 ± 0.05	S82	4.8	3.53	0.68 ± 0.14	
ACT-CL J0342.0+0105	55.5008	1.0873	1.07 ± 0.06	S82*	5.9	4.71	0.89 ± 0.15	
ACT-CL J0342.7-0017	55.6845	-0.2899	0.310	S82	4.6	5.88	0.70 ± 0.15	SDSS CE J055.683678-00.286974 (3)
ACT-CL J0348.6+0029	57.1612	0.4892	0.297	S82	5.0	2.35	0.69 ± 0.15	WHL J034837.9+002900 (6)
ACT-CL J0348.6-0028	57.1605	-0.4681	0.345	S82	4.7	2.35	0.67 ± 0.15	WHL J034841.5-002807 (6)
ACT-CL J0205.2+0030	306.3006	0.5130	0.34 ± 0.02	DR8	6.4	9.41	1.05 ± 0.17	WHL J202512.8+003134 (1)
ACT-CL J2050.5-0055	312.6264	-0.9311	0.622	S82*	5.6	1.18	0.83 ± 0.16	GMB11 J312.62475-00.92697 (2)
ACT-CL J2050.7+0123	312.6814	1.3857	0.333	DR8	7.4	4.71	1.16 ± 0.16	RXC J2050.7+0123 (7)
ACT-CL J2051.1+0056	312.7935	0.9488	0.333	S82	4.1	1.18	0.62 ± 0.17	WHL J205111.1+005646 (6)
ACT-CL J2051.1+0215	312.7885	2.2628	0.321	DR8	5.2	5.88	1.36 ± 0.26	RXC J2051.1+0216 (7)
ACT-CL J2055.4+0105	313.8581	1.0985	0.408	S82	4.9	3.53	0.77 ± 0.16	WHL J205526.6+010511 (6)
ACT-CL J2058.8+0123	314.7234	1.3836	0.32 ± 0.02	DR8	8.3	10.59	1.25 ± 0.15	WHL J205853.1+012411 (1)
ACT-CL J2128.4+0135	322.1036	1.5996	0.385	DR8	7.3	5.88	1.34 ± 0.18	WHL J212823.4+013536 (1)
ACT-CL J2129.6+0005	322.4186	0.0891	0.234	S82*	8.0	1.18	1.23 ± 0.17	RXC J2129.6+0005 (9)
ACT-CL J2130.1+0045	322.5367	0.7590	0.71 ± 0.04	S82	4.4	4.71	0.74 ± 0.17	
ACT-CL J2135.1-0102	323.7907	-1.0396	0.33 ± 0.01	S82	4.1	8.24	0.68 ± 0.17	WHL J213512.1-010258 (6)
ACT-CL J2135.2+0125	323.8151	1.4247	0.231	DR8	9.3	4.71	1.47 ± 0.16	Abell 2355 (4)
ACT-CL J2135.7+0009	323.9310	0.1568	0.118	S82	4.0	10.59	0.68 ± 0.17	Abell 2356 (4)
ACT-CL J2152.9-0114	328.2375	-1.2458	0.69 ± 0.02	S82	4.4	3.53	0.70 ± 0.17	
ACT-CL J2154.5-0049	328.6319	-0.8197	0.488	S82*	5.9	3.53	0.95 ± 0.17	WHL J215432.2-004905 (6)
ACT-CL J2156.1+0123	329.0407	1.3857	0.224	DR8	6.0	7.06	0.95 ± 0.16	Abell 2397 (4)
ACT-CL J2220.7-0042	335.1922	-0.7095	0.57 ± 0.03	S82	4.0	1.18	0.63 ± 0.18	GMB11 J335.19871-00.69024 (2)
ACT-CL J2229.2-0004	337.3042	-0.0743	0.61 ± 0.05	S82	4.0	15.29	0.66 ± 0.17	
ACT-CL J2253.3-0031	343.3432	-0.5280	0.54 ± 0.01	S82	4.0	2.35	0.64 ± 0.17	
ACT-CL J2302.5+0002	345.6427	0.0419	0.520	S82	4.9	4.71	0.82 ± 0.17	WHL J230235.1+000234 (6)
ACT-CL J2307.6+0130	346.9176	1.5161	0.36 ± 0.02	DR8	6.1	2.35	0.95 ± 0.17	WHL J230739.9+013056 (1)
ACT-CL J2327.4-0204	351.8660	-2.0777	0.705	DR8	13.1	3.53	2.65 ± 0.21	RCS2 J2327.4-0204 (10)
ACT-CL J2337.6+0016	354.4156	0.2690	0.275	S82*	8.2	7.06	1.43 ± 0.18	Abell 2631 (4)
ACT-CL J2351.7+0009	357.9349	0.1538	0.99 ± 0.03	S82	4.7	2.35	0.89 ± 0.21	

Table 7 — *Continued*

ACT ID	R.A. (°)	Dec. (°)	Redshift	Reg.	S/N	θ_{500} (arcmin)	\tilde{y}_0 (10^{-4})	Alternate ID (ref.)
--------	-------------	-------------	----------	------	-------	----------------------------	--------------------------------	---------------------

Note. — Coordinates are in the J2000 standard equinox. Redshifts for which uncertainties are quoted are photometric; all others are spectroscopic (full details can be found in [Menanteau et al. 2013](#)). The Region (Reg.) column indicates whether the cluster lies within the coverage of SDSS Stripe 82 or in the shallower coverage of SDSS DR8; an asterisk denotes clusters used for the cosmological analysis of Section 5. The signal to noise ratio and filter scale θ_{500} are provided for the matched filter template that yielded the most significant detection. The uncorrected central Compton parameter \tilde{y}_0 is obtained from maps filtered with the matched filter having $\theta_{500} = 5'.9$ (see Section 3.1). References: (1) [Wen et al. \(2012\)](#); (2) [Geach et al. \(2011\)](#); (3) [Goto et al. \(2002\)](#); (4) [Abell \(1958\)](#); (5) [Lopes et al. \(2004\)](#); (6) [Wen et al. \(2009\)](#); (7) [Böhlinger et al. \(2000\)](#); (8) [Hao et al. \(2010\)](#); (9) [Ebeling et al. \(1998\)](#); (10) [Gralla et al. \(2011\)](#).

Table 8
SZ-derived mass estimates for ACT clusters.

ID	θ_{500} (arcmin)	$Q(m, z)$	Y_{500} (10^{-4} arcmin ²)	M_{500c}^{UPP} ($10^{14} h_{70}^{-1} M_{\odot}$)	M_{500c}^{B12} ($10^{14} h_{70}^{-1} M_{\odot}$)	M_{500c}^{non} ($10^{14} h_{70}^{-1} M_{\odot}$)	M_{500c}^{dyn} ($10^{14} h_{70}^{-1} M_{\odot}$)
ACT-CL J0008.1+0201	3.3 ± 0.3	0.78 ± 0.05	4.0 ± 1.6	3.9 ± 1.1	5.2 ± 1.6	6.2 ± 2.0	4.9 ± 2.0
ACT-CL J0012.0-0046	1.2 ± 0.1	0.28 ± 0.03	1.4 ± 0.5	3.0 ± 0.8	3.9 ± 1.1	3.7 ± 1.0	3.3 ± 1.2
ACT-CL J0014.9-0057	2.8 ± 0.1	0.69 ± 0.02	5.0 ± 0.9	5.7 ± 1.1	7.6 ± 1.4	9.0 ± 1.7	8.2 ± 1.9
ACT-CL J0017.6-0051	4.6 ± 0.5	0.93 ± 0.04	5.0 ± 2.3	2.9 ± 1.0	3.9 ± 1.4	4.8 ± 1.8	3.4 ± 1.6
ACT-CL J0018.2-0022	1.8 ± 0.2	0.45 ± 0.05	1.5 ± 0.6	3.1 ± 0.9	4.0 ± 1.3	4.4 ± 1.4	3.6 ± 1.4
ACT-CL J0022.2-0036	2.1 ± 0.1	0.52 ± 0.02	3.8 ± 0.6	5.5 ± 0.9	7.3 ± 1.2	8.0 ± 1.4	7.7 ± 1.6
ACT-CL J0026.2+0120	2.2 ± 0.1	0.56 ± 0.03	2.8 ± 0.6	4.4 ± 0.9	5.8 ± 1.2	6.6 ± 1.3	5.8 ± 1.5
ACT-CL J0044.4+0113	1.3 ± 0.1	0.32 ± 0.04	1.1 ± 0.4	2.7 ± 0.8	3.5 ± 1.0	3.5 ± 1.1	3.0 ± 1.1
ACT-CL J0045.2-0152	2.8 ± 0.1	0.68 ± 0.02	4.8 ± 0.9	5.6 ± 1.1	7.5 ± 1.4	8.8 ± 1.6	8.0 ± 1.9
ACT-CL J0051.1+0055	1.7 ± 0.2	0.42 ± 0.06	0.9 ± 0.5	2.2 ± 0.8	2.8 ± 1.1	3.0 ± 1.3	2.2 ± 1.1
ACT-CL J0058.0+0030	1.8 ± 0.1	0.45 ± 0.04	1.5 ± 0.5	3.2 ± 0.8	4.1 ± 1.1	4.5 ± 1.3	3.7 ± 1.3
ACT-CL J0059.1-0049	2.1 ± 0.1	0.53 ± 0.02	3.5 ± 0.6	5.2 ± 0.9	6.9 ± 1.2	7.6 ± 1.3	7.2 ± 1.5
ACT-CL J0104.8+0002	3.5 ± 0.4	0.81 ± 0.06	2.8 ± 1.3	2.6 ± 0.9	3.5 ± 1.2	4.2 ± 1.5	3.0 ± 1.4
ACT-CL J0119.9+0055	1.9 ± 0.1	0.47 ± 0.04	1.7 ± 0.5	3.3 ± 0.8	4.3 ± 1.1	4.7 ± 1.3	3.9 ± 1.3
ACT-CL J0127.2+0020	3.0 ± 0.2	0.73 ± 0.04	2.8 ± 0.9	3.3 ± 0.9	4.4 ± 1.2	5.3 ± 1.4	4.1 ± 1.4
ACT-CL J0139.3-0128	1.6 ± 0.2	0.40 ± 0.06	0.8 ± 0.5	2.1 ± 0.9	2.6 ± 1.1	2.8 ± 1.2	2.1 ± 1.1
ACT-CL J0152.7+0100	5.4 ± 0.2	0.98 ± 0.01	13.0 ± 2.3	5.7 ± 1.1	7.9 ± 1.6	9.7 ± 1.9	8.7 ± 2.3
ACT-CL J0156.4-0123	2.6 ± 0.2	0.64 ± 0.05	2.1 ± 0.8	3.1 ± 0.9	4.0 ± 1.2	4.7 ± 1.4	3.6 ± 1.4
ACT-CL J0206.2-0114	2.2 ± 0.1	0.54 ± 0.02	2.6 ± 0.6	4.3 ± 0.8	5.7 ± 1.1	6.4 ± 1.2	5.7 ± 1.4
ACT-CL J0215.4+0030	1.9 ± 0.1	0.47 ± 0.03	1.8 ± 0.5	3.5 ± 0.8	4.5 ± 1.1	5.0 ± 1.2	4.2 ± 1.3
ACT-CL J0218.2-0041	2.1 ± 0.1	0.54 ± 0.03	2.2 ± 0.6	3.8 ± 0.8	4.9 ± 1.1	5.6 ± 1.3	4.7 ± 1.3
ACT-CL J0219.8+0022	2.2 ± 0.2	0.57 ± 0.05	1.7 ± 0.7	3.0 ± 0.9	3.9 ± 1.2	4.5 ± 1.4	3.5 ± 1.4
ACT-CL J0219.9+0129	3.0 ± 0.3	0.73 ± 0.05	2.3 ± 0.9	2.8 ± 0.8	3.7 ± 1.1	4.5 ± 1.4	3.3 ± 1.3
ACT-CL J0221.5-0012	1.6 ± 0.2	0.40 ± 0.06	0.5 ± 0.3	1.4 ± 0.6	1.8 ± 0.8	2.0 ± 0.9	1.4 ± 0.7
ACT-CL J0223.1-0056	2.1 ± 0.1	0.53 ± 0.03	2.2 ± 0.6	3.8 ± 0.8	5.0 ± 1.1	5.7 ± 1.3	4.8 ± 1.4
ACT-CL J0228.5+0030	1.7 ± 0.2	0.42 ± 0.06	1.0 ± 0.5	2.4 ± 0.8	3.0 ± 1.1	3.3 ± 1.3	2.5 ± 1.2
ACT-CL J0230.9-0024	2.5 ± 0.3	0.64 ± 0.06	1.9 ± 0.8	2.8 ± 0.9	3.7 ± 1.2	4.3 ± 1.4	3.2 ± 1.4
ACT-CL J0239.8-0134	3.9 ± 0.1	0.85 ± 0.01	9.4 ± 1.6	6.7 ± 1.3	9.1 ± 1.7	11.1 ± 2.0	10.3 ± 2.5
ACT-CL J0240.0+0116	2.1 ± 0.2	0.53 ± 0.04	1.8 ± 0.6	3.3 ± 0.8	4.3 ± 1.1	4.8 ± 1.3	3.9 ± 1.3
ACT-CL J0241.2-0018	1.8 ± 0.2	0.44 ± 0.06	1.1 ± 0.5	2.5 ± 0.9	3.2 ± 1.2	3.6 ± 1.3	2.7 ± 1.2
ACT-CL J0245.8-0042	5.0 ± 0.6	0.95 ± 0.04	4.9 ± 2.4	2.5 ± 0.9	3.4 ± 1.3	4.1 ± 1.6	2.8 ± 1.4
ACT-CL J0250.1+0008	1.7 ± 0.2	0.41 ± 0.05	1.2 ± 0.5	2.7 ± 0.8	3.5 ± 1.1	3.7 ± 1.2	3.0 ± 1.2
ACT-CL J0256.5+0006	3.1 ± 0.2	0.76 ± 0.03	3.4 ± 1.0	3.8 ± 0.9	5.0 ± 1.2	6.1 ± 1.4	4.8 ± 1.5
ACT-CL J0301.1-0110	2.0 ± 0.3	0.51 ± 0.07	1.1 ± 0.6	2.2 ± 0.8	2.8 ± 1.1	3.2 ± 1.3	2.3 ± 1.2
ACT-CL J0301.6+0155	6.7 ± 0.4	1.01 ± 0.01	15.7 ± 5.0	4.7 ± 1.2	6.6 ± 1.8	8.1 ± 2.1	6.7 ± 2.4
ACT-CL J0303.3+0155	6.9 ± 0.6	1.01 ± 0.01	14.9 ± 5.5	4.2 ± 1.2	5.8 ± 1.8	7.1 ± 2.1	5.6 ± 2.3
ACT-CL J0308.1+0103	1.9 ± 0.2	0.48 ± 0.05	1.3 ± 0.6	2.7 ± 0.8	3.4 ± 1.1	3.8 ± 1.3	3.0 ± 1.3
ACT-CL J0320.4+0032	3.0 ± 0.2	0.72 ± 0.04	2.8 ± 0.9	3.3 ± 0.9	4.4 ± 1.2	5.3 ± 1.4	4.1 ± 1.4
ACT-CL J0326.8-0043	3.1 ± 0.1	0.75 ± 0.02	5.5 ± 0.9	5.5 ± 1.0	7.4 ± 1.4	8.9 ± 1.6	7.9 ± 1.9
ACT-CL J0336.9-0110	1.2 ± 0.1	0.27 ± 0.03	1.0 ± 0.4	2.5 ± 0.7	3.2 ± 0.9	3.1 ± 0.9	2.7 ± 1.0
ACT-CL J0342.0+0105	1.5 ± 0.1	0.37 ± 0.02	1.8 ± 0.4	3.7 ± 0.7	4.8 ± 1.0	4.8 ± 1.0	4.5 ± 1.1
ACT-CL J0342.7-0017	3.4 ± 0.3	0.80 ± 0.04	3.2 ± 1.2	3.1 ± 0.9	4.1 ± 1.2	5.0 ± 1.5	3.7 ± 1.4
ACT-CL J0348.6+0029	3.5 ± 0.3	0.81 ± 0.04	3.3 ± 1.2	3.1 ± 0.9	4.1 ± 1.2	5.0 ± 1.5	3.7 ± 1.4
ACT-CL J0348.6-0028	3.1 ± 0.3	0.75 ± 0.05	2.6 ± 1.0	3.0 ± 0.9	4.0 ± 1.2	4.8 ± 1.5	3.5 ± 1.4
ACT-CL J2025.2+0030	3.6 ± 0.2	0.83 ± 0.02	5.5 ± 1.3	4.6 ± 1.0	6.3 ± 1.4	7.7 ± 1.6	6.4 ± 1.8
ACT-CL J2050.5-0055	2.2 ± 0.1	0.56 ± 0.04	2.2 ± 0.7	3.8 ± 0.9	4.9 ± 1.2	5.6 ± 1.4	4.7 ± 1.4
ACT-CL J2050.7+0123	3.9 ± 0.2	0.85 ± 0.02	6.7 ± 1.4	5.1 ± 1.0	7.0 ± 1.4	8.5 ± 1.7	7.4 ± 1.9
ACT-CL J2051.1+0056	3.0 ± 0.4	0.73 ± 0.07	2.1 ± 1.1	2.5 ± 0.9	3.3 ± 1.3	4.0 ± 1.6	2.8 ± 1.4
ACT-CL J2051.1+0215	4.0 ± 0.3	0.87 ± 0.03	7.6 ± 2.5	5.3 ± 1.4	7.1 ± 1.9	8.6 ± 2.4	7.2 ± 2.6
ACT-CL J2055.4+0105	2.9 ± 0.2	0.70 ± 0.04	2.8 ± 1.0	3.5 ± 0.9	4.6 ± 1.3	5.5 ± 1.5	4.3 ± 1.5
ACT-CL J2058.8+0123	4.1 ± 0.2	0.88 ± 0.02	7.8 ± 1.4	5.5 ± 1.1	7.5 ± 1.5	9.2 ± 1.8	8.0 ± 2.0
ACT-CL J2128.4+0135	3.5 ± 0.1	0.81 ± 0.02	6.8 ± 1.4	5.7 ± 1.1	7.7 ± 1.6	9.4 ± 1.8	8.3 ± 2.1
ACT-CL J2129.6+0005	5.2 ± 0.2	0.97 ± 0.01	11.4 ± 2.4	5.3 ± 1.1	7.3 ± 1.6	9.1 ± 1.9	7.9 ± 2.2
ACT-CL J2130.1+0045	1.9 ± 0.2	0.47 ± 0.05	1.6 ± 0.6	3.2 ± 0.9	4.1 ± 1.2	4.5 ± 1.4	3.7 ± 1.4
ACT-CL J2135.1-0102	3.1 ± 0.4	0.75 ± 0.06	2.6 ± 1.2	2.8 ± 1.0	3.7 ± 1.3	4.5 ± 1.6	3.2 ± 1.5
ACT-CL J2135.2+0125	5.3 ± 0.2	0.97 ± 0.01	14.2 ± 2.4	6.3 ± 1.2	8.7 ± 1.7	10.8 ± 2.1	9.9 ± 2.6
ACT-CL J2135.7+0009	7.3 ± 1.0	1.01 ± 0.01	10.8 ± 6.3	2.6 ± 1.1	3.6 ± 1.6	4.3 ± 1.9	2.9 ± 1.8
ACT-CL J2152.9-0114	1.9 ± 0.2	0.47 ± 0.05	1.5 ± 0.6	3.0 ± 0.9	3.9 ± 1.3	4.2 ± 1.4	3.4 ± 1.4
ACT-CL J2154.5-0049	2.7 ± 0.2	0.68 ± 0.03	3.4 ± 0.9	4.3 ± 0.9	5.7 ± 1.3	6.8 ± 1.5	5.7 ± 1.6
ACT-CL J2156.1+0123	4.9 ± 0.3	0.95 ± 0.02	7.9 ± 2.2	4.1 ± 1.0	5.7 ± 1.4	7.0 ± 1.7	5.7 ± 1.8

Table 8 — *Continued*

ID	θ_{500} (arcmin)	$Q(m, z)$	Y_{500} (10^{-4} arcmin ²)	M_{500c}^{UPP} ($10^{14} h_{70}^{-1} \text{M}_{\odot}$)	M_{500c}^{B12} ($10^{14} h_{70}^{-1} \text{M}_{\odot}$)	M_{500c}^{non} ($10^{14} h_{70}^{-1} \text{M}_{\odot}$)	M_{500c}^{dyn} ($10^{14} h_{70}^{-1} \text{M}_{\odot}$)
ACT-CL J2220.7–0042	2.0 ± 0.3	0.50 ± 0.07	1.2 ± 0.7	2.5 ± 1.0	3.1 ± 1.3	3.5 ± 1.5	2.6 ± 1.4
ACT-CL J2229.2–0004	2.0 ± 0.2	0.49 ± 0.06	1.3 ± 0.7	2.7 ± 1.0	3.4 ± 1.3	3.8 ± 1.5	2.9 ± 1.4
ACT-CL J2253.3–0031	2.1 ± 0.3	0.54 ± 0.06	1.5 ± 0.7	2.7 ± 0.9	3.5 ± 1.3	4.0 ± 1.5	3.0 ± 1.4
ACT-CL J2302.5+0002	2.5 ± 0.2	0.62 ± 0.04	2.5 ± 0.8	3.7 ± 0.9	4.8 ± 1.3	5.6 ± 1.5	4.6 ± 1.5
ACT-CL J2307.6+0130	3.4 ± 0.2	0.80 ± 0.03	4.5 ± 1.2	4.2 ± 1.0	5.7 ± 1.3	6.9 ± 1.6	5.7 ± 1.7
ACT-CL J2327.4–0204	2.8 ± 0.1	0.67 ± 0.01	10.1 ± 1.0	9.4 ± 1.5	12.5 ± 2.0	14.3 ± 2.2	14.9 ± 3.0
ACT-CL J2337.6+0016	4.8 ± 0.2	0.94 ± 0.01	11.5 ± 2.2	6.1 ± 1.2	8.4 ± 1.7	10.3 ± 2.0	9.3 ± 2.5
ACT-CL J2351.7+0009	1.5 ± 0.2	0.36 ± 0.05	1.5 ± 0.7	3.2 ± 1.0	4.0 ± 1.4	4.1 ± 1.5	3.4 ± 1.6

Note. — Mass estimates obtained as described in Section 3.2. The \tilde{y}_0 - M scaling relation is fixed to either the UPP result, the fit to the B12 model, the fit to Nonthermal20 model (superscript “non”), or the fit to dynamical masses of Sifón et al. (2012) (superscript “dyn”). Masses and SZ quantities are computed from the cluster’s uncorrected central Compton parameter \tilde{y}_0 and redshift measurements, including correction for mass function bias. The cluster scale θ_{500} , value of the bias function $Q(m, z)$, and integrated Compton parameter Y_{500} are those inferred from the UPP scaling relation. Uncertainties do not include uncertainty in the scaling relation parameters, but do include the effects of intrinsic scatter and the measurement uncertainty. SZ and mass errors are highly correlated.

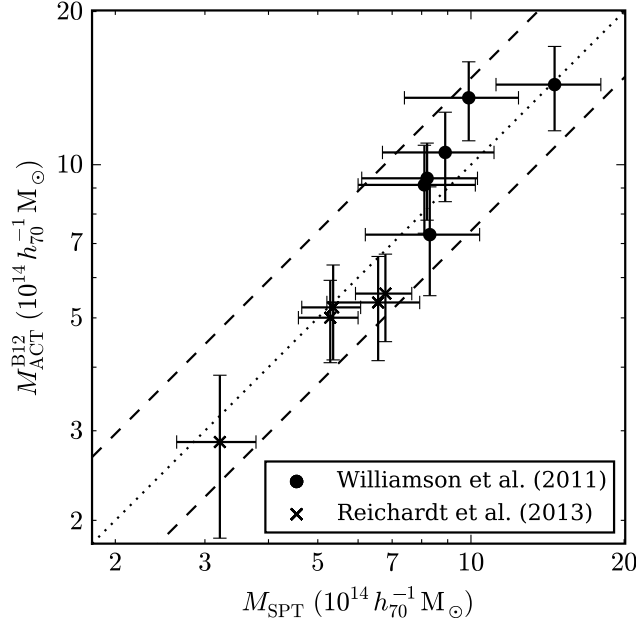


Figure 21. Comparison of ACT SZ based masses (from B12 scaling relation) to masses from the South Pole Telescope. Both are M_{500c} . ACT masses are computed using the B12 scaling relation and may be found in Table 10. SPT masses are taken from Williamson et al. (2011) (mass is computed from SZ signal based on scaling relation calibrated to Shaw et al. (2010) models; only statistical uncertainty is included in error bars), and Reichardt et al. (2013) (mass is computed from combination of Y_X and SZ measurements). The weighted mean mass ratio for the 11 clusters is 0.99 ± 0.06 , though there is evidence of a systematic difference between the mass calibration in the two SPT catalogs. Dotted line traces equality of SPT and ACT masses for the B12 scaling relation. Dashed lines trace approximate loci of agreement between SPT masses and ACT masses based on the UPP (upper line) and Nonthermal20 (lower line) scaling relations. Uncertainties in the ACT and SPT measurements for each cluster are likely to be partially correlated, since both use properties of cluster gas to infer a total mass.

APPENDIX

ANALYSIS OF ACT SOUTHERN CLUSTERS

In this appendix we apply the methodology of Sections 3.1 and 3.2 to estimate masses and SZ quantities for the 23 clusters from the original ACT Southern cluster sample, described in Marriage et al. (2011, hereafter M11) and Menanteau et al. (2010). For this analysis, we use updated maps that include additional data acquired in this field during the 2009 and 2010 observing seasons.

In Table 9 we summarize the basic properties of the Southern cluster sample, and include our measurement of the uncorrected central temperature decrement taken from maps filtered with the $\theta_{500} = 5.9$ UPP matched filter. While this filter incorporates the same cluster profile that was used in the analysis of the Equatorial sample, the filter itself is slightly different due to the different noise properties in the Southern maps. In Table 10 we present cluster mass and SZ quantity estimates.

There is substantial overlap between the ACT Southern field and the cluster samples presented by the SPT collaboration. The M11 sample includes six of the clusters analyzed in Williamson et al. (2011, hereafter W11), and five of the clusters in Reichardt et al. (2013, hereafter R12). In W11 a scaling relation based on the SPT signal to noise ratio and calibrated to the models of Shaw et al. (2010) is used to obtain SZ based mass estimates. In R12, masses are presented that are derived from a combination of SZ and X-ray measurements, though X-ray measurements are expected to dominate because of the smaller uncertainty in the X-ray scaling relation. (Four of the five ACT clusters appearing in R12 have X-ray mass measurements.)

We find the SPT masses to be in good agreement with our masses based on the B12 model scaling relation parameters, with weighted mean mass ratio $M^{\text{B12}}/M^{\text{SPT}} = 0.99 \pm 0.06$. We note, however, a difference in the mean ratio for each of the two SPT catalogs. For the clusters in R12 the mass ratio is 0.88 ± 0.09 , while for the higher mass, lower redshift sample of W11 the ratio is 1.10 ± 0.09 . In Figure 21 we show the masses. We note that this difference in mass ratio is consistent with the observation in W11 that their average SZ determined masses are smaller than Y_X based masses by a factor of 0.78 ± 0.06 . In contrast, the R12 masses for four of the five common clusters include input from observations of Y_X , which is likely to dominate over the contribution from SZ data.

Table 9
Uncorrected central Compton parameters for the clusters from
Marriage et al. (2011).

ACT ID	R.A. ($^{\circ}$)	Dec. ($^{\circ}$)	Redshift	S/N	\tilde{y}_0 (10^{-4})	Alternate ID (ref.)
ACT-CL J0102–4915*	15.7208	−49.2553	0.870	9.0	3.51 ± 0.43	SPT-CL J0102-4915 (1)
ACT-CL J0145–5301	26.2458	−53.0169	0.118	4.0	0.86 ± 0.19	Abell 2941 (2)
ACT-CL J0215–5212	33.8250	−52.2083	0.480	4.9	0.79 ± 0.18	RXC J0217.2-5244 (3)
ACT-CL J0217–5245	34.2958	−52.7556	0.343	4.1	0.79 ± 0.18	
ACT-CL J0232–5257	38.1875	−52.9522	0.556	4.7	0.61 ± 0.17	
ACT-CL J0235–5121	38.9667	−51.3544	0.278	6.2	0.98 ± 0.19	Abell S0295 (4)
ACT-CL J0237–4939	39.2625	−49.6575	0.334	3.9	0.93 ± 0.26	
ACT-CL J0245–5302	41.3875	−53.0344	0.300	9.1	1.57 ± 0.17	SPT-CL J0245-5302 (1)
ACT-CL J0304–4921	46.0625	−49.3617	0.392	3.9	1.52 ± 0.32	Abell 3128 NE (5)
ACT-CL J0330–5227*	52.7250	−52.4678	0.442	6.1	1.23 ± 0.18	
ACT-CL J0346–5438	56.7125	−54.6483	0.530	4.4	1.05 ± 0.22	
ACT-CL J0438–5419*	69.5792	−54.3181	0.421	8.0	1.62 ± 0.13	SPT-CL J0438-5419 (1)
ACT-CL J0509–5341*	77.3375	−53.7014	0.461	4.8	0.82 ± 0.14	SPT-CL J0509-5342 (6)
ACT-CL J0516–5430	79.1250	−54.5083	0.294	4.6	0.87 ± 0.15	Abell S0520 (4)
ACT-CL J0528–5259	82.0125	−52.9981	0.768	3.1	0.50 ± 0.13	SPT-CL J0516-5430 (6)
ACT-CL J0546–5345*	86.6542	−53.7589	1.066	6.5	0.92 ± 0.14	SPT-CL J0528-5300 (6)
ACT-CL J0559–5249*	89.9292	−52.8203	0.609	5.1	0.89 ± 0.14	SPT-CL J0546-5345 (6)
ACT-CL J0616–5227*	94.1500	−52.4597	0.684	5.9	1.00 ± 0.15	SPT-CL J0559-5249 (6)
ACT-CL J0638–5358	99.6917	−53.9792	0.222	10.0	1.77 ± 0.15	Abell S0592 (4)
ACT-CL J0641–4949	100.3958	−49.8089	0.146	4.7	0.58 ± 0.26	SPT-CL J0638-5358 (1)
ACT-CL J0645–5413	101.3750	−54.2275	0.167	7.1	1.19 ± 0.17	Abell 3402 (2)
ACT-CL J0658–5557	104.6250	−55.9511	0.296	11.5	2.65 ± 0.21	Abell 3404 (2)
ACT-CL J0707–5522	106.8042	−55.3800	0.296	3.3	0.54 ± 0.21	SPT-CL J0645-5413 (1)
						1E0657-56/Bullet (7)
						SPT-CL J0658-5556 (1)

Note. — Clusters used for cosmological and scaling relation constraints in Section 5 are marked with an asterisk. Redshifts are all spectroscopic, obtained from literature as described in Menanteau et al. (2010) or as presented in Sifón et al. (2012). We provide the S/N of detection as presented in Marriage et al. (2011), for reference. Uncorrected central Compton parameters \tilde{y}_0 are obtained from the application of a matched filter with $\theta_{500} = 5'.9$ (see Section 3.1). Alternate IDs are provided for clusters detected before the initial release of the Southern sample, and for any cluster appearing in current SPT results. References: (1) Williamson et al. (2011); (2) Abell (1958); (3) Böhringer et al. (2004); (4) Abell et al. (1989); (5) Werner et al. (2007); (6) Reichardt et al. (2013); (7) Tucker et al. (1995).

Table 10
SZ-derived mass estimates for the ACT Southern cluster sample of
Marriage et al. (2011).

ID	θ_{500} (arcmin)	$Q(m, z)$	Y_{500} (10^{-4} arcmin 2)	M_{500c}^{UPP} ($10^{14} h_{70}^{-1} M_{\odot}$)	M_{500c}^{B12} ($10^{14} h_{70}^{-1} M_{\odot}$)	M_{500c}^{non} ($10^{14} h_{70}^{-1} M_{\odot}$)	M_{500c}^{dyn} ($10^{14} h_{70}^{-1} M_{\odot}$)
ACT-CL J0102–4915	2.5 ± 0.1	0.60 ± 0.02	11.5 ± 2.0	10.5 ± 1.8	13.8 ± 2.4	15.0 ± 2.6	16.0 ± 3.5
ACT-CL J0145–5301	8.1 ± 0.9	1.02 ± 0.01	16.9 ± 8.2	3.5 ± 1.2	4.8 ± 1.8	5.7 ± 2.2	4.2 ± 2.2
ACT-CL J0215–5212	2.5 ± 0.2	0.62 ± 0.05	2.4 ± 1.0	3.5 ± 1.0	4.5 ± 1.4	5.2 ± 1.7	4.1 ± 1.7
ACT-CL J0217–5245	3.2 ± 0.3	0.75 ± 0.05	3.2 ± 1.3	3.4 ± 1.0	4.4 ± 1.4	5.3 ± 1.8	4.0 ± 1.7
ACT-CL J0232–5257	2.0 ± 0.3	0.49 ± 0.07	1.2 ± 0.7	2.5 ± 1.0	3.1 ± 1.3	3.5 ± 1.5	2.6 ± 1.4
ACT-CL J0235–5121	4.1 ± 0.3	0.87 ± 0.03	5.9 ± 2.0	4.1 ± 1.1	5.6 ± 1.5	6.8 ± 1.8	5.4 ± 1.9
ACT-CL J0237–4939	3.2 ± 0.5	0.74 ± 0.09	3.1 ± 2.1	3.1 ± 1.4	3.9 ± 1.9	4.6 ± 2.4	3.2 ± 2.1
ACT-CL J0245–5302	4.6 ± 0.2	0.92 ± 0.01	12.1 ± 2.0	6.7 ± 1.3	9.2 ± 1.8	11.3 ± 2.1	10.4 ± 2.6
ACT-CL J0304–4921	3.5 ± 0.3	0.79 ± 0.05	6.8 ± 2.6	5.7 ± 1.6	7.4 ± 2.3	8.7 ± 2.8	7.3 ± 3.1
ACT-CL J0330–5227	3.2 ± 0.1	0.74 ± 0.02	5.4 ± 1.2	5.4 ± 1.1	7.3 ± 1.5	8.7 ± 1.7	7.7 ± 2.0
ACT-CL J0346–5438	2.6 ± 0.2	0.62 ± 0.04	3.3 ± 1.1	4.4 ± 1.2	5.7 ± 1.6	6.6 ± 1.9	5.5 ± 2.0
ACT-CL J0438–5419	3.6 ± 0.1	0.80 ± 0.01	8.8 ± 1.0	7.0 ± 1.2	9.5 ± 1.6	11.5 ± 1.9	10.9 ± 2.3
ACT-CL J0509–5341	2.8 ± 0.1	0.66 ± 0.03	3.1 ± 0.7	4.0 ± 0.8	5.3 ± 1.1	6.3 ± 1.3	5.2 ± 1.4
ACT-CL J0516–5430	3.9 ± 0.2	0.85 ± 0.03	5.1 ± 1.3	4.0 ± 0.9	5.4 ± 1.2	6.7 ± 1.5	5.3 ± 1.6
ACT-CL J0528–5259	1.6 ± 0.2	0.37 ± 0.05	0.9 ± 0.4	2.3 ± 0.8	2.9 ± 1.0	3.1 ± 1.1	2.4 ± 1.1
ACT-CL J0546–5345	1.6 ± 0.1	0.36 ± 0.02	2.0 ± 0.4	3.9 ± 0.7	5.1 ± 0.9	5.2 ± 1.0	4.9 ± 1.1
ACT-CL J0559–5249	2.3 ± 0.1	0.56 ± 0.02	2.8 ± 0.6	4.3 ± 0.8	5.7 ± 1.1	6.5 ± 1.3	5.6 ± 1.4
ACT-CL J0616–5227	2.2 ± 0.1	0.53 ± 0.02	3.0 ± 0.6	4.6 ± 0.9	6.1 ± 1.2	6.9 ± 1.3	6.2 ± 1.5
ACT-CL J0638–5358	6.1 ± 0.2	1.00 ± 0.01	22.4 ± 3.0	7.5 ± 1.4	10.5 ± 2.0	13.0 ± 2.4	12.5 ± 3.2
ACT-CL J0641–4949	4.8 ± 1.0	0.93 ± 0.06	2.9 ± 3.2	1.4 ± 0.9	1.8 ± 1.2	2.2 ± 1.4	1.3 ± 1.1
ACT-CL J0645–5413	6.9 ± 0.3	1.02 ± 0.01	18.2 ± 4.3	5.1 ± 1.2	7.3 ± 1.7	8.9 ± 2.0	7.7 ± 2.4
ACT-CL J0658–5557	5.4 ± 0.1	0.97 ± 0.01	26.6 ± 3.2	10.3 ± 1.9	14.3 ± 2.6	17.6 ± 3.1	18.2 ± 4.3
ACT-CL J0707–5522	2.8 ± 0.5	0.69 ± 0.09	1.4 ± 1.1	1.7 ± 0.9	2.2 ± 1.2	2.6 ± 1.4	1.7 ± 1.1

Note. — Columns are as described in Table 8.